PEM FUEL CELL STACK MODELING AND DESIGN OF DC/DC CONVERTER FOR FUEL CELL ENERGY SYSTEM

KONG XIN

NATIONAL UNIVERSITY OF SINGAPORE

2008

PEM FUEL CELL STACK MODELING AND DESIGN OF DC/DC CONVERTER FOR FUEL CELL ENERGY SYSTEM

KONG XIN

(*M.Eng., XJTU, P.R.China*)

A THESIS SUBMITTED FOR THE DEGREE OF

DOCTOR OF PHILOSOPHY

DEPARTMENT OF ELECTRICAL & COMPUTER ENGINEERING

NATIONAL UNIVERSITY OF SINGAPORE

2008

To my husband Zuo Hai and my son Zuo Chenyu

Acknowledgements

I would like to express my sincere thanks to my research supervisor Dr. Ashwin M Khambadkone, for his guidance, support, and brain storming discussions in my tenure as research student. Not only is he actively involved in the work of all his students, he is also a great advisor guiding us to appreciate the arts of the research. Thanks to his prim and precise character, which has pushed me to struggle from understanding the fundamentals to heading for higher levels.

I am grateful to National University of Singapore for supporting this research project through the research grant $R-263-000-248-112$.

Lab officers Mr. Teo Thiam Teck, Mr. Woo Ying Chee, Mr. Chandra, and Mr. Seow Hung Cheng have been a great help. They are always there to offer technical support and help. Their smiling faces and pleasant chatting always cheer me up. Without them, the research project would not get so smooth. I would like to extend my sincere appreciations to Mr. Abdul Jalil Bin Din for his prompt PCB fabrication services.

During my stay in NUS, the life has been made pleasant by many friends sur-

rounded me. Foremost among them are Singh Ravinder Pal, Jiang Yonghong, Zhou Haihua, Xu Xinyu, Tripathi Anshuman, Gupta Amit, who are with me in the same research group. Their endless encouragement and readily help are steady motivations for me. I would like to thank Chen Yu, Yin Bo, Wei Guannan, Qin Meng, Wu Xinhui, Deng Heng, Yang Yuming, Cao Xiao, Kanakasabai Viswanathan, Krishna Mainali, Marecar Hadja, Sahoo Sanjib Kumar, for their help and concern in both my research project and personal life.

Finally, I would like to thank those closest to me. My husband, Zuo Hai who always there gave me care, understanding and support, is the constant source of my encouragement. I would like to thank my parents Mr. Kong Zhaoxia, Ms. Ma JinHua, my parents-in-law Mr. Zuo Wensen and my sister Ms. Kong Li, for their confidence and support during this doctoral research.

Contents

Summary

As a promising alternative energy source for 21st century, fuel cell based power supply is becoming increasingly important for future energy requirements. Due to its low voltage rating, load-dependence, fuel cell stack voltage has to be boosted and regulated for widespread applications. To boost the fuel cell stack voltage, power electronics, which is good at processing and controlling electrical energy can be used. To regulate fuel cell stack voltage, a fuel cell model which effectively describes the fuel cell behavior, can be used to facilitate the controller design.

The main objective of the research is twofold:

1. Fuel cell stack modelling

2. DC/DC converter design

The aim of the first aspect of the research is to develop a simple and accurate fuel cell stack model which can predict both steady-state and dynamic behavior of the stack. After introducing different fuel cell modelling techniques and their pros and cons, a hybrid fuel cell stack model is designed without the need for detailed

electrochemical and fluid dynamical models. This model is able to describe the stack's steady-state characteristics, charge double layer dynamics and temperature effects. Identification of the model parameters is analyzed in details. To improve the model dynamic accuracy and flexibility, ANN technique is brought into the hybrid model to model the nonlinear subsystem. It improves accuracy and allows the model to adapt itself to operating conditions. What is more, temperature effect on the fuel cell stack is modelled using the stack current with the help of ANN to represent the relationship between current and temperature. Real-time implementation of the proposed ANN model is realized on a dSPACE system. Experimental results are provided to verify the validity of the proposed model.

Following the fuel cell stack modelling, the other aim of the research is to design a proper DC/DC converter for fuel cell based power supply. After comparison and discussion of possible candidates of DC/DC converter topologies, the current-fed full bridge converter (CFFB) is selected due to its inherent high boost ratio, and direct control of fuel cell current. A $1.2kW$ current-fed full bridge converter is designed with a voltage doubler on the secondary side. A digital closed loop control is designed and implemented on DSP TMS320F243. Experimental results are provided.

Based on the analysis of the CFFB converter, an interleaved current-fed full bridge converter (ICFFB) is designed with a parallel input/series output scheme. The parallel connection results reduced current-stress on the semiconductor devices on the input side, while the series connection on the output side results in lower voltage ratings

for output capacitors and diodes. Due to the interleaving of the converter modules, smaller inductors and capacitors can be selected. Moreover, a soft start-up strategy is proposed for ICFFB converter without additional start-up circuits but a small current rating switch on the output side. With the aid of this switch and snubber capacitors, large inrush current during start-up stage is suppressed with small power loss and with hardly any increase in the size of the converter. All PWM signals, closed loop controller and soft start-up is implemented on one DSP board TMS320F243. Higher efficiency and smaller magnetic components are verified by the experimental results.

For both CFFB and ICFFB converters, a closed loop voltage controller with an inner average current controller is designed and implemented. Due to their inherent boost characteristics, the small signal control-to-output voltage transfer function presents a RHP zero. This produces a non minimum phase behavior. In order to minimize the RHP zero effect and improve the dynamic performance of boost type converters, a combined feed-forward/feedback controller is designed by switching between two controller structures. After first proving the stability of the combined feed-forward/feedback controller, strategy of how and when to switch between the controller structures is analyzed. The closed-loop control is implemented on a dSPACE 1104 system. Experimental results are provided to show the improved dynamic performance with fast response and small voltage undershoot/overshoot.

List of Figures

List of Tables

Chapter 1

Introduction

Fuel cell is being considered as a promising alternative energy source for the future energy requirements [1]. It may be a viable energy source for the future due to its potential high efficiency, low emission of pollutants and little maintenance [2]. However fuel cells usually provide very low DC voltage. A fuel cell voltage is usually less than $1V$ when drawing a useful current. Even with fuel cell stacks (tens or hundreds of single fuel cells are connected properly to produce a useful voltage), the output DC voltage of the stack can hardly meet high voltage load requirement. Moreover, fuel cell voltage is unregulated and varies a lot as the load changes. Hence to create a fuel cell based power supply, one need to boost and regulate fuel cell voltage. Power electronics, which is good at processing and controlling electrical energy, can be used to this end.

To boost the low DC voltage of the fuel cell stack to around $400V$, a DC/DC

converter is usually required to be connected with the stack. However due to the inherent characteristics of fuel cell stack voltage such as low rating and load-dependence, a suitable converter topology has to be used. On the other hand, as opposed to other power supplies, fuel cell is an electrochemical device. Strictly non-negative current, low switching current ripple and direct control of the fuel cell current put very specific requirements on the power converter topologies. Thus the following questions need to be answered: What kind of DC/DC converter topology is the suitable choice for a fuel cell based power supply? How to design the converters? These questions lead me to one part of this research, the DC/DC converter design.

To regulate fuel cell stack voltage, fuel cell characteristics should be taken into consideration. To describe the fuel cell characteristics, fuel cell model seems to be an effective way to simulate the fuel cell behavior. Based on different fuel cell operating modes, different fuel cell behavior such as steady-state and dynamic characteristics should be included to facilitate the controller design. Then the next problem is how to obtain a fuel cell model which is capable of predicting both the steady-state and dynamic characteristics? This lead me to another part of the research: fuel cell stack modelling.

1.1 Issues Studied

Issues studied in the thesis are in two aspects:

1. Fuel cell stack modelling

   Among all the publications, many models were mainly concerned about the steady state characteristics of the fuel cell, and models capable of describing transient phenomena are scanty. Although some models were developed to include both steady-state and dynamic characteristics of the fuel cell, the requirement of extensive computation and good knowledge of electrochemistry makes them inaccessible to many electrical engineers. Hence one of the research aim is to develop a simple and accurate fuel cell stack model which can predict both steady-state and dynamic behavior of the stack.

2. DC/DC converters

   DC/DC converter is one of the important components in a fuel cell powered system. It allows us to obtain a desired level of DC voltage without having to increase the stack size. But to design a DC/DC converter which converts fuel cell stack voltage of $26V \sim 42V$ to $400V$, a large boost ratio from ten to twenty is necessary. On the other hand, the ripple current seen by the fuel cell stack due to the switching of the DC/DC converter has to be low. Moreover, since fuel cell current is proportional to hydrogen input, the amount of hydrogen generated in a direct hydrogen system could be better controlled if the fuel cell stack current is directly controlled. There are currently two groups of DC/DC converter topologies: voltage-fed and current-fed converters. Although many voltage-fed topologies have been implemented in some of the publications, the lack of direct

control of input current and the need of a high turns-ratio transformer might not be quite suitable for a fuel cell system. Current-fed full bridge converter, on the other hand, seems to be a competitive choice due to its good control of input current. However it is hard to realize the high boost ratio up to ten or twenty using simple boost converter alone. Current-fed full bridge converter has the inherent high boost ratio, but it is seldom used as the DC/DC converter in a high power fuel cell system. The main hurdles to utilize this topology are large magnetic cores of high current inductor and the uncontrolled large inrush current during its start-up. Hence the other aim of the research is to develop a DC/DC converter topology suitable for a medium to high power fuel cell system. This converter should have large boost ratio, low input current ripple and high efficiency.

1.2 Contribution of the Thesis

Since the focus of the thesis is twofold, The major contributions of the thesis is classified in two parts:

Part I Fuel Cell Models

- A simple and accurate fuel cell stack model is proposed. It can model both steady state and dynamic characteristics of the fuel cell stack. "Charge double layer" dynamics and temperature effect on the stack are both included. Iden-

tification of model parameters is proposed and the model is verified with the experimental results on a $1.2kW$ fuel cell stack. Although the design of the model is based on a commercial fuel cell stack, model derivation method can be applied to other PEM (Proton Exchange Membrane) fuel cell stacks.

- A real-time ANN model is proposed and implemented on a dSPACE system. Only fuel cell stack current is sensed and the real-time stack voltage can be predicted by the ANN model. By using ANN to model the nonlinear subsystem in the hybrid model, it improves accuracy and allows the model to adapt itself to varying operating conditions. Good correlations are achieved between the real-time ANN model and the experimental results.

Part II DC/DC converters

- An isolated current-fed full bridge (CFFB) converter is proposed with large boost ratio and low input current ripple. Experimental results have been done to verify the analysis.

- An interleaved current-fed full bridge (ICFFB) converter is proposed for medium to high power fuel cell systems. With interleaved switching, parallel inputs and series connection of outputs, high efficiency, reduced input current ripple and smaller magnetic components could be achieved. A $1.2kW$ ICFFB converter was built and a digital controller was implemented on DSP to regulate both the input current and the output voltage.

- Soft start-up of ICFFB converter is realized without introducing any additional start-up circuit but a small current rating switch on the output side. During the start-up, output capacitors can be gradually charged up from zero to almost rated voltage with the aid of this switch and the snubber capacitors in the ICFFB converter. Hence the undesirable large inrush current is suppressed before the converter "enters into" the normal operating status.

- A combined feed-forward/feedback controller is proposed to improve the dynamic performance of boost type converters. By changing over between the feed-forward structure and feedback structures, a fast transient response can be achieved. Moreover, the voltage undershoot/overshoot is also reduced.

1.3 Organization of the Thesis

The thesis is divided into two parts. Part I focuses on the development of a fuel cell stack model while Part II presents the design and implementation of a DC/DC converter suitable for fuel cell based power supply. There are totally nine chapters in this thesis, each with a specific focus. The organization of the thesis is as following:

Part I Fuel Cell Stack Modelling

- **Chapter 2** gives the background and literature survey on fuel cell modelling. Different fuel cell modelling techniques are reviewed and evaluated. This helps

bring out the focus of the present work and also recognize the problem.

- **Chapter 3** proposes a simple hybrid fuel cell stack model which can predict both the steady state and dynamic behavior of the stack. Description of model development and parameter identification are explained. Steady state and dynamic behavior of the hybrid model are verified by the experimental results.

- **Chapter 4** proposes an ANN model to improve the accuracy by modelling the nonlinear subsystem in the hybrid model. Real-time implementation of the ANN model is realized on a dSPACE system. Model structure and development are described and experimental results are provided to verify the validity of the proposed model.

Part II DC/DC Converters

- **Chapter 5** starts with the discussion of the criteria required during the selection of the DC/DC converter topologies for a fuel cell based power supply and follows by a detailed survey on DC/DC converters candidates. Performance of different DC/DC converter candidates are evaluated and compared. Problem definition is brought out.

- **Chapter 6** develops an improved current-fed full bridge converter (CFFB) with a voltage doubler. This converter has a large boost ratio and low input current ripple. Detailed circuit analysis is performed and a closed loop controller is

realized on a DSP board. This chapter provides an analytical basis for the ICFFB converter proposed in Chapter 7.

- **Chapter 7** proposes an interleaved current-fed full bridge converter (ICFFB) that has smaller magnetic components, reduced input current ripple and high efficiency. Moreover, large inrush current during start-up can be eliminated without adding extra start-up circuit. This ICFFB converter is a good DC/DC converter candidate for high power fuel cell systems.

- **Chapter 8** describes the design and implementation of a combined feed-forward/feedback controller on a dSPACE system. Stability of the controller is proved and criteria to switch between different structures are analyzed.

- **Chapter 9** presents the conclusions and future works.

Chapter 2

Survey of Fuel Cell Modelling

2.1 Fuel Cell Principle

Fuel cell was discovered in 1839 by William R. Grove [3]. It is an electrochemical device that uses hydrogen and oxygen, with the aid of electrocatalysts to generate electricity. According to the type of electrolyte used, fuel cells can be divided into five types: PAFC (Phosphoric Acid Fuel Cell), AFC (Alkaline Fuel Cell), PEMFC (Proton Exchange Membrane Fuel Cell), MCFC (Molten Carbonate Fuel Cell) and SOFC (Solid Oxide Fuel Cell). Among them, PEMFC is believed to be the best candidate for automotive and residential applications due to its high power density, smaller size, rapid start-up and low operating temperature [4].

Typical structure of a PEM fuel cell is shown in Fig. 2.1. It consists of an electrolyte sandwiched between two electrodes − anode and cathode. These three

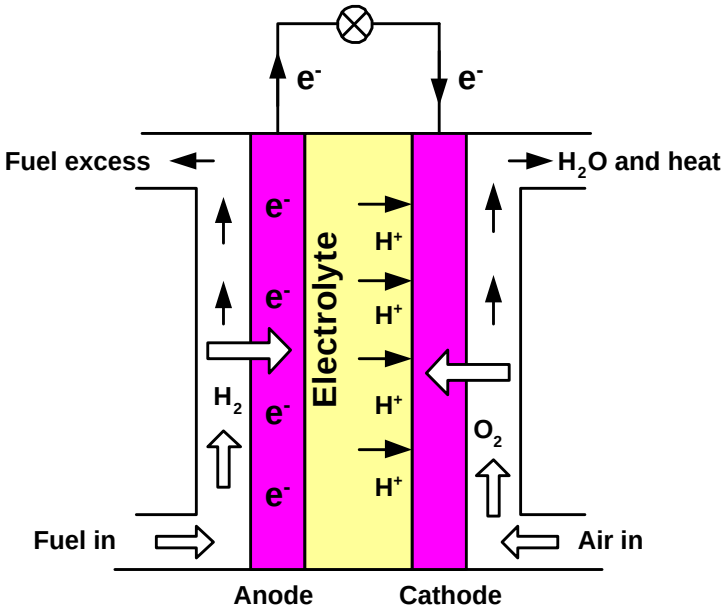

Figure 2.1: Fuel cell operating principle

components (anode, cathode and electrolyte) are sealed together to form a single Membrane Electrolyte Assembly (MEA). Hydrogen is fed to the anode, and oxygen is fed to the cathode. With the help of the catalyst, hydrogen is oxidized and separated into electrons and hydrogen ions (Eq. 2.1). Hydrogen ions move from anode to cathode through electrolyte. Since the electrolyte allows only proton exchanges, the electrons can only travel to the cathode via an external circuit, where they recombine with oxygen and hydrogen ions to produce water and electricity (Eq. 2.2).

Anode reaction:

$$H_2 \longrightarrow 2H^+ + 2e^- \tag{2.1}$$

Cathode reaction:

$$\frac{1}{2}O_2 + 2H^+ + 2e^- \longrightarrow H_2O \tag{2.2}$$

Overall reaction:

$$H_2 + \frac{1}{2}O_2 \longrightarrow H_2O \tag{2.3}$$

2.2 Fuel Cell Modelling

Many papers have been published on the modelling of PEM fuel cells since 1960s. Objectives of these studies are to model the performance of fuel cells and suggest the way to optimize structures of electrodes, membranes and electrode assemblies. At earlier stage of fuel cell modelling, most of the studies focused on fuel cell steady state behavior, that is, they modeled the fuel cell polarization curve (fuel cell voltage versus current density) over a range of operating conditions. This approach is usually known as steady state modelling. While another approach of fuel cell modelling: dynamic modelling, becomes more of an issue in recent years, because dynamic response of the fuel cell in power systems or transportation applications is of extreme importance especially when load condition changes with time [5]. A detailed survey on these two approaches is made in the following sections.

2.2.1 Steady State Modelling

Steady state modelling can be divided into two categories: analytical models and empirical models.

Analytical Models

A completely analytical model that includes all performance variables has not been found [6], because these kinds of models would be so complex and specific that they are actually of little use for simulation with electrical system. Hence many analytical models include some empirical features. T.E. Springer presented an isothermal, one-dimensional, steady-state PEM fuel cell model by developing and solving a large number of differential equations [7] [8], which are formulated with electrochemical and fluid mechanics. A research group from Royal Military College of Canada completed several substantial work related to Ballard fuel cells [9] [10] [11]. A mechanistic model was initially developed based on Nernst and Tafel equations. It included many important physical parameters in the system (effective pressure of fuels, temperature and concentration of fuels, water and proton etc.). Since it was impossible to mathematically identify all the parameters, the authors rendered the mathematical equations to parametric form and estimated the parameters via empirical approach. The model provides a more flexible modelling alternative than the complex mechanistic models proposed earlier in [7] [8] [12]. Several publications presented the formulations of fuel cell stack models. A mathematical stack model was developed to determine the

fundamental thermal-physical behavior for any operating and design configurations [13]. While S. Yerramalla [14] presented a comprehensive mathematical stack model that incorporated other separate computational modules into the design to model the behavior of a fuel cell power system.

Although many of the analytical models currently used have already been simplified, they still require the knowledge of parameters not readily available. Some of these are transfer coefficients, internal humidity level and catalyst layer thickness etc. Analytical models can simulate the performance of fuel cell over a large range of operating conditions, but the requirement of extensive computation and good knowledge of electrochemistry makes them inaccessible to many electrical engineers. Hence a set of empirical models were proposed by some researchers for simplification.

Empirical Models

Empirical models are derived from experimental data. Since the model parameters are obtained using data fitting technique, they are accurate only in a small operating range. However, simplicity is the most attractive feature of the empirical model. An empirical equation (Eq. 2.4) was presented by Junbom Kim [15] to obtain the cell potential plots at several temperature, pressure and oxygen compositions in the cathode gas mixture.

$$V''_{cell} = V''_o - R''j - b'' * \log j - m'' \exp(n'' * j). \tag{2.4}$$

Where V_o'', R'', b'', m'' and n'' are empirical parameters, and j is fuel cell current density. Excellent correlation between the experimental data and the empirical equation was demonstrated at different operating conditions. This model introduced mass transport voltage drop into the model, which is characterized by an exponential term $m'' \exp(n'' * j)$. Major effect of parameter m'' and n'' was analyzed in detail. Since the five variables are dependant on different operating conditions, S. Busquet [16] proposed to link the influence of temperature T and oxygen partial pressure (p_{O_2}) on the five empirical parameters of model in [15] with the following form: $K_1 + K_2 T + K_3 T \ln(p_{O_2})$. Hence each of the variables V_o'', R'', b'', m'' and n'' becomes related to the operating condition via three coefficients K_1, K_2 and K_3 but the number of empirical parameters, on the other hand, increases from five to fifteen. Based on this single cell structure, D. Chu [17] developed an empirical stack model without considering mass transport voltage drop. Stack performance at various humidity and temperatures was analyzed.

Few empirical models have been proposed recently that use artificial intelligence (AI) techniques. They use AI to achieve the fit of fuel cell polarization curve. S. Jemeï [18] presented a "black box" model of a PEM fuel cell by using Artificial Neural Networks (ANN), which allowed a behavioral modelling without having to determine all system parameters. Input vectors are stoichiometric factors and fuel cell current, while the output is fuel cell stack voltage. By training fifty neurons in one hidden layer, the "black box" model is able to evaluate the stack output voltage

and its variations. C. Nitsche [19] described an approach that utilize artificial neural networks to alleviate the task of onboard diagnostics for fuel cell vehicles. Since many performance degradation factors can be extracted from the change of the polarization curves of the fuel cell, a "grey box" fuel cell model was proposed by using adaptive curve fitting techniques to capture the characteristic curves of a fuel cell system. However both [18] and [19] have not discussed the dynamic performance of the fuel cell stack.

Among all the publications on steady state modelling, models capable of describing transient phenomena are scanty. Especially for empirical models, which are mainly obtained from data fitting technique, it is difficult to include time varying behavior of the fuel cell stack. However, to understand the interaction of power electronic circuits with fuel cell stack, dynamic behavior of the stack is very helpful.

2.2.2 Dynamic Modelling

Different dynamic effects exist in a fuel cell system and they have time constants varying over a wide range of order of magnitudes [20]. The thermal dynamic is considered as the slowest dynamic in fuel cell systems and has the highest order of magnitude (about 10^{2}s). Hence many studies on dynamic modelling only take the temperature effect into consideration while neglecting other faster phenomenon. E. Achenbach [21] investigated the transient behavior of a solid oxide fuel cell caused by load changes. After the current step, an undershoot of fuel cell voltage occurred before the voltage

settled down. Since the cell internal resistance is temperature dependant, the settling process of the fuel cell is closely related to the transient temperature distribution of the cell structure. Although the paper is focused on SOFC, it provided the analysis which is a good reference for PEM fuel cells. By coupling an electrochemical model with a thermal model, J. C. Amphlett [5] proposed a transient model which predicts fuel cell performance as a function of time due to the changes imposed on the system. This thermal model was developed by performing mass and energy balance on the stack. It included the changes in the heat of electrodes and water circulation streams and the theoretical energy release etc..

Other dynamics like charge double layer dynamics that influence the faster load dynamics have become an issue. Charge double layer phenomenon is caused by the layer of charge near the electrode/electrolyte interface, which stores electrical charge and energy, and behaves much like an electrical capacitor. During the load changes, it takes a certain time for this charge to build up or dissipate [3]. Charge double layer dynamics is usually represented as a first order equivalent circuit [3] [22] as shown in Fig. 2.2. E is open circuit voltage of the fuel cell, R_h models resistive voltage drops.

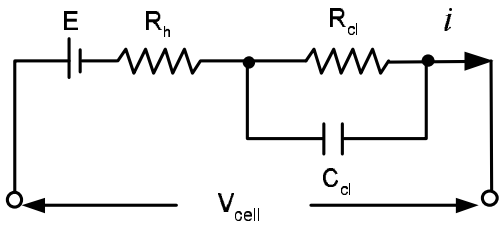

Figure 2.2: Equivalent electrical circuit of dynamic fuel cell model

R_{cl} and C_{cl} represent the charge double layer phenomenon. A more complex dynamic circuit was proposed in [23] for transportation applications, in which, an equivalent circuit was developed to model the charge double layer dynamics on both of the electrodes. Spectroscopy of electrochemical impedance was performed to identify model parameters. Voltage response of the fuel cell to rapid change of load demand was analyzed.

Recently S. Pasricha [24] proposed a dynamic fuel cell stack model by extending a static current voltage description to include temperature dependence. Small signal models of stack voltage and thermal response were derived and effect of model parameters was evaluated. C. Wang [25] presented a dynamic model for PEM fuel cell by using several electrical circuits to represent different voltage drops and thermodynamic properties in a fuel cell, where current and temperature effects are represented as current-dependant and temperature-dependant resistors. By doing so, a totally electrical circuit model of fuel cell was built in PSPICE. Simulation results show that the model can predict the electrical response of the PEM fuel cell stack under steady-state as well as transient conditions.

2.2.3 Combination of Steady state and dynamic modelling

Some work has been done to evaluate both the steady state and dynamic performance of fuel cell models in recent several years. J.M. Corrêa [26] presented a dynamic and electrochemical model for evaluation of a small generation system using PEM fuel

cells. Steady state performance and dynamic response to load insertion/rejection were evaluated. However temperature effect on fuel cell performance was not emphasized and experimental result was not provided. But in his later publication [27], this electrochemical model was tested on three different fuel cell stacks and good agreement with manufacture's data was presented. A dynamic model based on physical and chemical equations was proposed later by M. Ceraolo [28]. The model was characterized by a set of partial differential equations. Both the temperature effect and charge double layer dynamics were included in the model. Good agreement was observed between the model and the experimental results. Although some of the differential equations had already been simplified, there were still twenty-two numerical parameters required for modelling. More recently, K. Sedghisigarchi [29] proposed a SOFC model including thermal dynamics. It was found that the temperature related dynamics is important for slow transients that occur for long time durations and it can be neglected for shorter time intervals. But no experimental results were provided to verify the simulation results. Pathapati P. R [30] proposed a single cell model for predicting steady state and transient performance of a PEM fuel cell. This model included transient effects of charge double layer as well as heat transfer. A value of $3F$ was given to capacitor C_{cl} but derivation of this capacitance was not provided. The model was verified by the benchmark study in [5]. Experimental results of fuel cell steady state performance were shown, but none was provided to verify the dynamic performance of the model when load changes.

2.3 Problem Definition

Despite the large number of publications on fuel cell modelling, a simple and accurate fuel cell stack model suitable for electrical engineers is still lacking.

- Many models are developed on single cell level, which are not convenient for practical use when the fuel cell stack is connected with power converters.

- Most of the existing models are modeled with a static polarization relationship, which neglect the dynamic characteristics of the fuel cell. However, the capability of predicting fuel cell dynamics is useful for developing control strategies for the whole system.

- Most of the fuel cell models developed by chemical researchers are based on lumped electrochemical equations. These analytical models investigate deep into physical phenomenon of the fuel cell by dealing with tens of fuel cell model parameters [20] [28]. Although analytical models can simulate fuel cell performance over a large range of operating conditions, the requirement of extensive computation and unreadily available parameters makes these models inaccessible to many electrical engineers.

- Most of the fuel cell models used by electrical engineers are usually simple R model [31] [32], which are obtained by linearizing the V-I curve of the fuel cell at the rated operating point. Model parameters are constants obtained at

rated operating point. Accuracy of these models cannot be ensured when the operating point of the fuel cell stack shifts.

Based on these problems, one aim of the research is to develop a simple and accurate fuel cell stack model suitable for electrical engineers. This model should be able to predict both the steady-state and dynamic behavior of the fuel cell stack.

2.4 Summary

This chapter presents a detailed literature survey of fuel cell modelling. Advantages and disadvantages of different fuel cell modelling techniques are briefly summarized. Analytical fuel cell models [7] [8] [9] and empirical fuel cell models [15] [16] [17] are all able to describe fuel cell $V - I$ relationship while dynamic models [5] [23] are helpful to understand the dynamic behavior of the fuel cell when they interact with fast changing DC loads. Therefore a fuel cell model which can characterize both steady-state and dynamic performance of the fuel cell stack is necessary. Although analytical models can simulate the performance of fuel cell over a large range of operating conditions, the requirement of extensive computation and good knowledge of electrochemistry makes them inaccessible to many electrical engineers. Empirical models, on the other hand, have an attractive feature of simplicity, but fails to include fuel cell dynamics into the model. Electrical circuit model is capable of representing charge double layer dynamics of the fuel cell, but it fails to model

the nonlinear polarization curve of the fuel cell for all operating range. Hence one of the research objectives is find out a combined model that can make use of the advantages of both empirical model and electrical circuit model. Later in Chapter 3, a hybrid fuel cell model is proposed with the combination of an empirical model and electrical circuit model. This model is simple and accurate in predicting both of the steady-state and dynamic behavior of the fuel cell stack. In order to work with varying operating conditions and further improve dynamic accuracy, an ANN model is developed in Chapter 4 to model some nonlinear parts of the hybrid model. Real-time implementation of the proposed ANN model is realized on a dSPACE system.

Chapter 3

Hybrid PEM Fuel Cell Modelling

3.1 Introduction

One of the research aims is to obtain a simple and accurate fuel cell stack model suitable for electrical engineers. This model should be able to predict both steady state and dynamic characteristics of the fuel cell stack. From Chapter 2, it is known that an empirical model is simple but it is difficult to include dynamic performance in these models. While an electrical circuit model can predicate charge double layer dynamics but it cannot work for all operating range. Hence in this chapter, a hybrid model with the combination of an empirical stack model and an electrical circuit stack model, is proposed.

3.2 Development of a Hybrid PEM Fuel Cell Stack Model

Fig. 3.1 shows the schematic diagram of the proposed hybrid fuel cell stack model. i is fuel cell current and V_{stack} is fuel cell stack voltage. It is implemented in MATLAB SIMULINK©. As seen from Fig. 3.1, the proposed model can be divided into three parts: empirical stack model, electrical circuit stack model and temperature effect. Interactions exist among all three parts. Since each part is proposed based on a physical phenomena or an empirical equation, it is necessary to understand how they are interconnected.

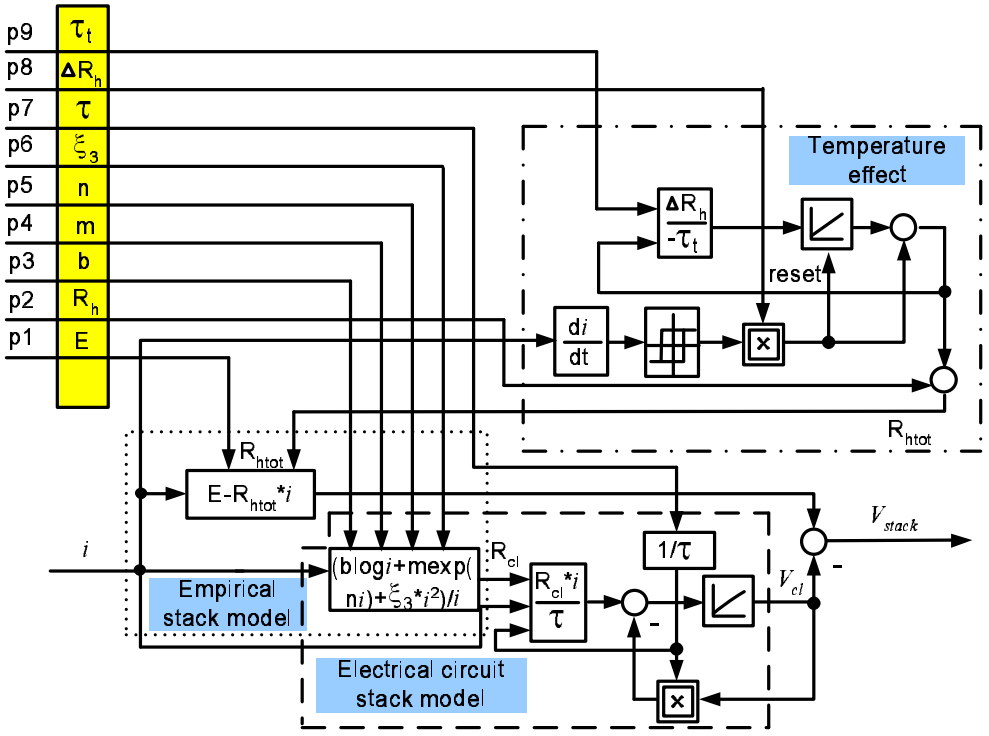

Figure 3.1: Schematic diagram of the proposed fuel cell stack model

3.2.1 Empirical fuel cell stack model

The empirical fuel cell model proposed by Junbom Kim is selected due to its good correlation between the experimental data and the model demonstrated in [15]. It gives the relationship of a single fuel cell voltage and fuel cell current density as

$$V''_{cell} = V''_o - R''j - b'' * \log j - m'' \exp(n'' * j). \tag{3.1}$$

Where V''_o, b'', R'', m'' and n'' are empirical parameters, and j is fuel cell current density. However in practical conditions, fuel cell current i is usually preferred. Since current i is actually the product of the current density j and the active area of the membrane-electrodes assemblies A_{mea}, Eq. 3.1 can be rewritten as Eq. 3.2 by substituting $i = j * A_{mea}$ into Eq. 3.1. Now Eq. 3.2 shows the $V - i$ relationship of a single fuel cell.

$$V'_{cell} = V'_o - R'i - b' * \log i - m' \exp(n' * i). \tag{3.2}$$

Where V'_o, b', R', m' and n' are still empirical parameters and can be represented as:

$$\begin{cases} V'_o = V''_o + b'' * \log A_{mea}, \quad R' = R''/A_{mea}, \\ m' = m'', \quad n' = n''/A_{mea}, \quad b' = b''. \end{cases}$$

For a fuel cell stack with N numbers of fuel cells connected in series, the empirical fuel cell stack model can be obtained as

$$\begin{aligned} V_{stack} &= N * (V'_o - R'i - b' * \log i - m' \exp(n' * i)), \\ &= V_o - Ri - b * \log i - m \exp(n * i). \end{aligned} \tag{3.3}$$

Where V_o, b, R, m and n are stack model parameters and $V_o = N * V_o'$, $b = N * b'$, $R = N * R'$, $m = N * m'$, $n = n'$.

3.2.2 Electrical circuit stack model

The equivalent electrical circuit proposed in [3] [22] is selected as the dynamic fuel cell model due to its simplicity and accuracy. The circuit is shown in Fig. 3.2. E' is the open circuit voltage of the fuel cell, R_h' models resistive voltage drops. R_{cl}' and C_{cl}' represent the charge double layer phenomenon. When N numbers of single

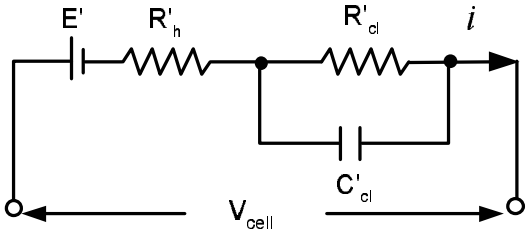

Figure 3.2: Electrical circuit model of single fuel cell

electrical circuit models are connected in series, an electrical circuit stack model can be easily obtained by applying basic circuit derivation as shown in Fig. 3.3. Where

$$\begin{cases} R_h = NR_h', \quad R_{cl} = NR_{cl}', \quad C_{cl} = \dfrac{1}{N}C_{cl}', \\ \tau = R_{cl}'C_{cl}' = R_{cl} * C_{cl}. \end{cases} \tag{3.4}$$

Fuel cell stack voltage $V_{stack}(t)$ in Fig. 3.3 can be represented as:

$$V_{stack}(t) = E - R_h i(t) - v_{cl}(t). \tag{3.5}$$

Where $v_{cl}(t)$ is the instantaneous voltage across capacitor C_{cl}.

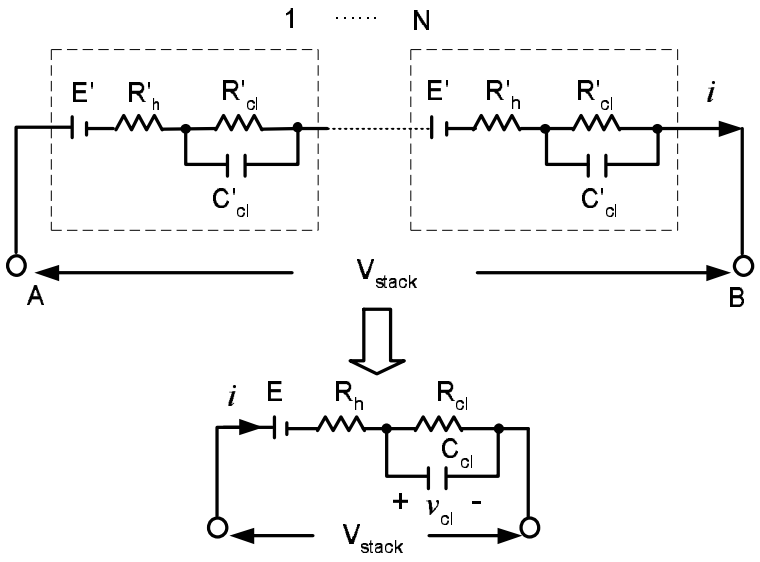

Figure 3.3: Stack model derivation with single cells connecting in series

3.2.3 Combination of empirical stack model and electrical circuit stack model

An empirical fuel cell stack model and an electrical circuit stack model have been obtained as shown in Eq. 3.3 and Eq. 3.5 respectively. The empirical stack model can simulate only the steady state performance whereas the electrical circuit stack model can simulate dynamic performance of the fuel cell stack. For a hybrid model which can evaluate both the steady state and dynamic performance of the fuel cell stack, an interconnection between the two diverse stack models is required.

Rewriting Eq. 3.3 by defining all the nonlinear part in the equation as $f(i)$:

$$V_{stack}(t)|_{t\to\infty} = V_o - Ri(t)|_{t\to\infty} - f(i)|_{t\to\infty}. \tag{3.6}$$

Where

$$f(i)|_{t\to\infty} = b * \log i(t)|_{t\to\infty} + m \exp(n * i(t))|_{t\to\infty}. \tag{3.7}$$

Comparing Eq. 3.6 and Eq. 3.5 in steady state, and assuming $V_o = E$ and $R = R_h$:

$$v_{cl}(t)|_{t\to\infty} = f(i)|_{t\to\infty}. \tag{3.8}$$

In order to combine the empirical stack model and the electrical circuit stack model, R_{cl} is obtained from empirical stack model. It is defined as fuel cell current divided by v_{cl} in steady state. Based on Eq. 3.8, following derivation can be obtained:

$$R_{cl} = \frac{v_{cl}(t)}{i(t)}|_{t\to\infty} = \frac{f(i)}{i(t)}|_{t\to\infty}. \tag{3.9}$$

For a first order electrical circuit, it is easy to find that

$$V_{cl} = R_{cl}(i_{cell} - C_{cl}\frac{dV_{cl}}{dt}) \tag{3.10}$$

Applying Lapalace transformation, the transfer function from $v_{cl}(s)$ to fuel cell current $i(s)$ can be obtained as:

$$\frac{v_{cl}(s)}{i(s)} = \frac{R_{cl}}{R_{cl}C_{cl}s + 1} = \frac{R_{cl}}{\tau s + 1}. \tag{3.11}$$

Where $\tau = R_{cl}C_{cl}$. As seen from Fig. 3.1, transfer function in Eq. 3.11 is realized as electrical circuit stack model (shown in dashed box). The output v_{cl} is the instantaneous voltage across the capacitor C_{cl}. v_{cl} is added to the output of the empirical stack model (shown in dotted box) to obtain V_{stack}. However, the internal resistance R_{htot} in the empirical stack model is actually a function of temperature (shown in dashed-dot box). In the next section, it will be shown why temperature effect should be included in the proposed model.

3.2.4 Temperature effect

Fig. 3.4 shows an experimental waveform of the fuel cell stack voltage response for a few hundred seconds of load insertion and extraction. When load steps up from

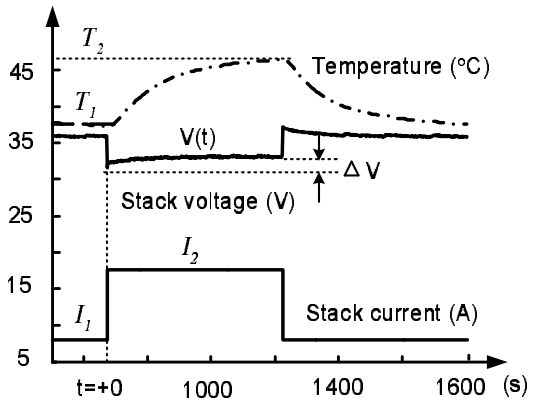

Figure 3.4: Stack voltage response to a long time interval current step

I_1 to I_2 at $t = +0$, a voltage undershoot is noticed before the voltage slowly reaches the new steady state. Elmar A. explained this undershoot phenomenon as the effect of internal resistance variation for SOFC [21]. Whereas, Pathapati P. R, provided a similar explanation for PEMFC [30]. Immediately after the load change ($t = +0$), fuel cell stack temperature is still low and is a function of the initial current value I_1. The higher amount of the heat produced at I_2 causes the stack temperature to increase which results in an increase in the stack voltage due to the decreasing internal resistance of the fuel cell stack. As proposed by [11], the internal resistance can be written as:

$$R = \xi_1 - \xi_2\theta + \xi_3 i. \tag{3.12}$$

Where $\xi_1 \sim \xi_3$ are all positive coefficients, θ is the stack temperature and i is the fuel cell current. Substituting Eq. 3.12 into Eq. 3.3 (the empirical stack model) and rewriting it, we get

$$V_{stack} = V_o - (\xi_1 - \xi_2\theta)i - \xi_3 i^2 - b * \log i - m\exp(n * i). \tag{3.13}$$

Redefining the nonlinear part in Eq. 3.13 as:

$$f(i) = \xi_3 i^2 + b * \log i(t) + m\exp(n * i(t)). \tag{3.14}$$

Now the nonlinear part of the fuel cell stack model $f(i)$ is represented as Eq. 3.14 after the temperature effect is considered. While the internal resistance of the fuel cell stack is defined as R_{htot}:

$$R_{htot} = \xi_1 - \xi_2\theta. \tag{3.15}$$

Fuel cell temperature θ can be represented as

$$\theta = \theta_{ss}(1 - e^{\frac{-t}{\tau_t}}) + \theta_0 e^{\frac{-t}{\tau_t}}. \tag{3.16}$$

Where θ_0 and θ_{ss} are initial and steady state temperature of the fuel cell stack after the load step, while τ_t is the time constant. Substituting Eq. 3.16 into Eq. 3.15, R_{htot} is rewritten as:

$$R_{htot} = R_h + \Delta R_h(t) \tag{3.17}$$

$$= R_h + \Delta R_h e^{\frac{-t}{\tau_t}}. \tag{3.18}$$

Where $\Delta R_h = (\theta_{ss} - \theta_0)\xi_2$, $R_h = \xi_1 - \theta_{ss}\xi_2$. It is noticed that R_{htot} is the summation of two parts: steady state value R_h and temperature dependant transient part $\Delta R_h(t) =$

$\Delta R_h e^{\frac{-t}{\tau_t}}$. The transient part $\Delta R_h(t)$ decays from ΔR_h at $t = +0$ to zero at $t \to \infty$. Since the transient part of the internal resistance is always zero in steady state, ΔR_h and τ_t will not affect the steady state performance of the fuel cell stack. This point is very helpful in model parameter identification described in the following section 3.4. It must be noted that R_h and ΔR_h are considered as constants here in order to simplify the model. But in fact these two parameters may vary with temperature. As will be explained later, the stack voltage variation caused by the effect of the temperature is less than 7% of the open circuit voltage. If the dispersion of the measurement is considered, the simplification can still be used to predict the fuel cell stack performance.

As seen in Fig. 3.1, implementation of the temperature effect is represented in the dashed-dot box. The output of this part is the summation of R_h and $\Delta R_h e^{\frac{-t}{\tau_t}}$ and it goes into the empirical stack model as the internal resistance R_{htot}. Now the hybrid fuel cell stack model has been obtained, and the next task is to identify model parameters. Before that, the experimental setup is first introduced.

3.3 Experimental setup

Fig. 3.5 shows the fuel cell system used for the project. It includes fuel cell stack, monitoring system and load bank. The fuel cell stack is a $1.2kW$ PEMFC stack from Ballard $Nexa^{TM}$. Hydrogen pressure is kept at 4.0 $barg$ ($56psig$), while the oxygen

(from ambient air) pressure is maintained by a compressor [33].

Schematic diagram of the experimental setup is shown in Fig. 3.6. Fuel cell

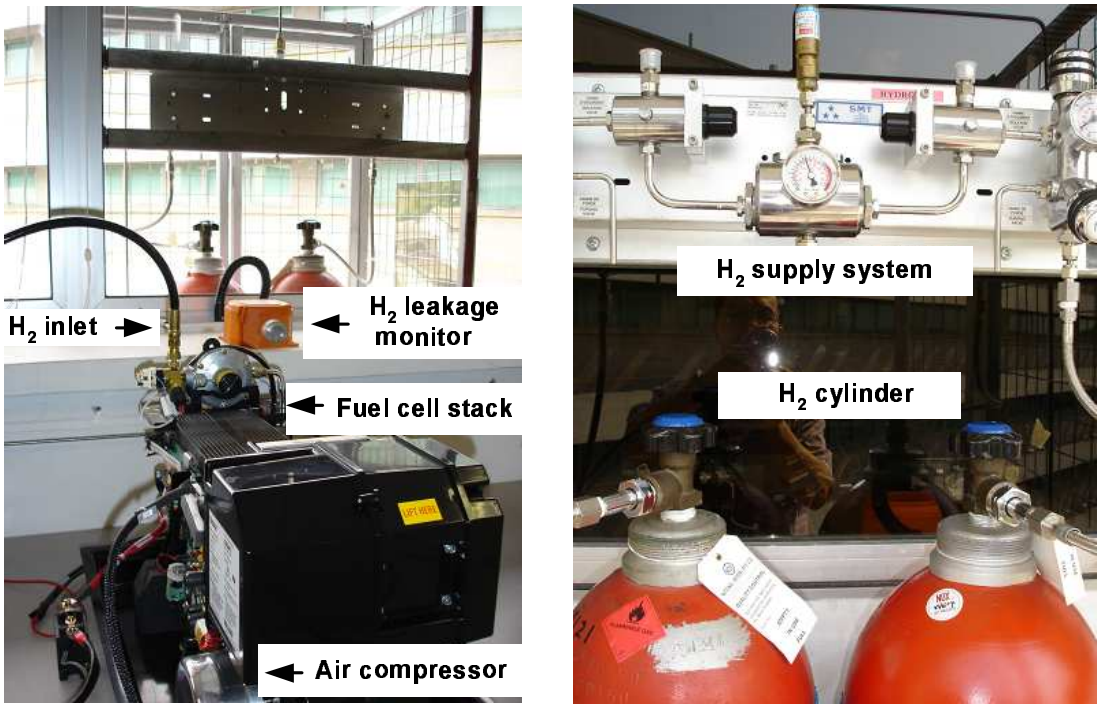

Figure 3.5: The fuel cell system used for experiments

working status is transmitted to the computer through RS485 communication cables. NexaMon OEM software provides those parameters that define the fuel cell working status such as stack voltage, stack temperature, pressure and oxygen concentration etc. Experimental data are obtained from NexaMon and a Tektronix TDS3034B digital oscilloscope. Load bank is designed to realize different load variations. As seen in Fig. 3.6, the load bank consists of six resistors. For $R_1 \sim R_5$, each resistor is capable of passing current of $12A$ and each resistance varies from $0 \sim 9\Omega$. S_1 and S_2 are used to switch on/off the load resistance network separately or simultaneously

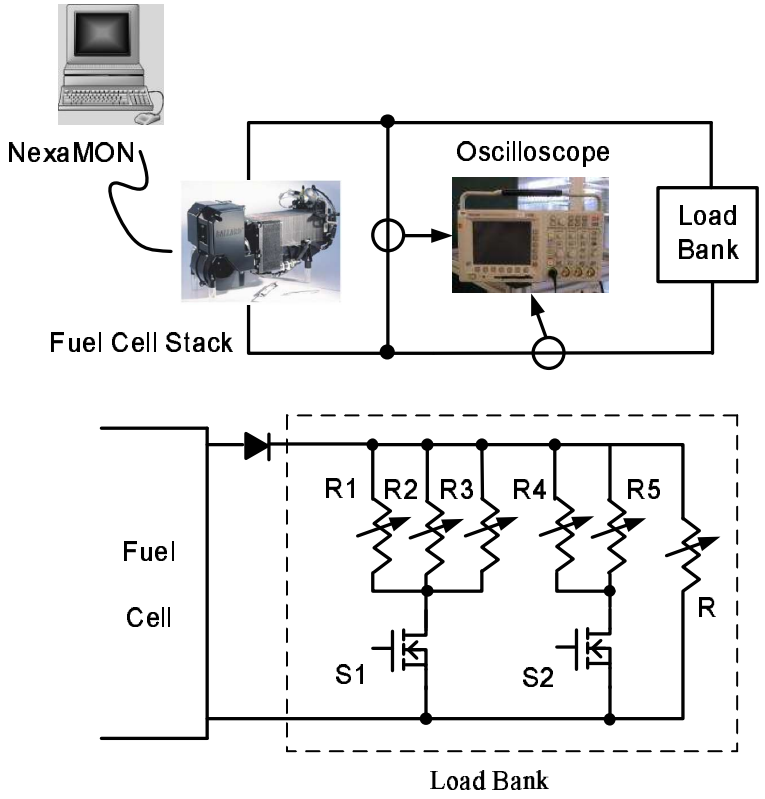

Figure 3.6: Schematic diagram of the experimental setup of Nexa fuel cell stack

according to different current step requirement. Resistor R is always connected to the stack and the resistance can vary from $0 \sim 1k\Omega$. This resistor is used to obtain the steady state performance evaluation of the stack.

3.4 Model parameter identification

As seen in Fig. 3.1, nine parameters have to be identified for the proposed model: E_o, R_h, b, m, n, ξ_3, τ, ΔR_h, τ_t. These parameters are identified following three steps.

3.4.1 Identification of electrical circuit parameters

Two techniques are usually used to identify the electrical circuit parameters [34] [35] [36] [37]: impedance spectroscopy and current-interruption. For impedance spectroscopy, alternating current with variable frequency is driven through the fuel cell. By monitoring the fuel cell voltage amplitude and phase angle, fuel cell impedance can be determined and fitted to the equivalent circuit in Fig. 3.2. However, since the capacitors are usually large and the impedances are small, special signal generators and measurement devices are needed [3]. Current-interruption technique is an alternative that can obtain accurate yet fast result. In this method the load current is changed instantaneously to a lower or a higher value. Fuel cell voltage which changes dynamically to a new steady state value, is recorded. With this method, identification of parameters that describe large signal characteristics can be performed [38].

Current-interruption technique is selected to identify the electrical circuit in the study, because it is simple and fast. First the parameters R_h and τ in the hybrid model are identified. R_h is the steady state value of the internal resistance of the fuel cell stack, while τ is the time constant of the charge double layer dynamics. A load resistor is adjusted to ensure that the stack is working at around rated power. Then the current is suddenly switched off and the stack voltage is recorded. An analytical method is proposed here to obtain all the parameters in the electrical circuit stack model with only one single voltage-transient data. Fig. 3.7 shows the typical waveform of the fuel cell stack voltage when fuel cell current is switched off. Voltage

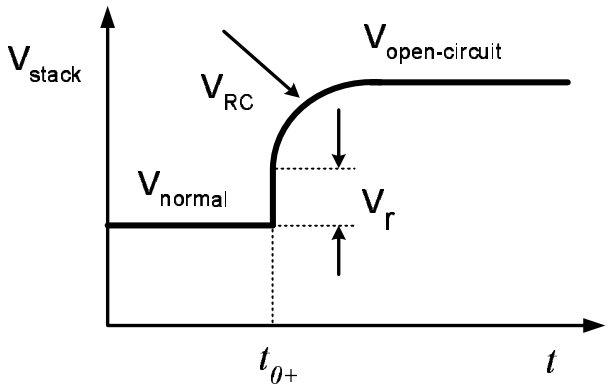

Figure 3.7: Typical waveforms of the voltage response to current interrupt

across the fuel cell stack after t_{0+} can be written as summation of three parts:

$$\begin{aligned} V_{stack} &= V_{normal} + V_r + V_{RC}, \\ &= V_{normal} + IR_h + IR_{cl}(1 - e^{\frac{-t}{\tau}}). \end{aligned} \tag{3.19}$$

Where I is the fuel cell current before switch turns off, and τ is the time constant $R_{cl}C_{cl}$. Let $\Delta V = V_{stack} - V_{normal}$,

$$\Delta V = IR_h + IR_{cl}(1 - e^{\frac{-t}{\tau}}). \tag{3.20}$$

Differentiating and linearizing on both sides of Eq. 3.20,

$$\ln \frac{\Delta V}{dt} = \ln \frac{IR_{cl}}{\tau} - \frac{t}{\tau}. \tag{3.21}$$

Using linear fitting as $y = -ax + b$, and solving for the unknowns, all parameters for electrical circuit stack model can be obtained:

$$\tau = \frac{1}{a}, \quad R_h = \frac{V_r}{I}, \quad C_{cl} = \frac{I}{e^b}, \quad R_{cl} = \frac{\frac{1}{a}}{C_{cl}}. \tag{3.22}$$

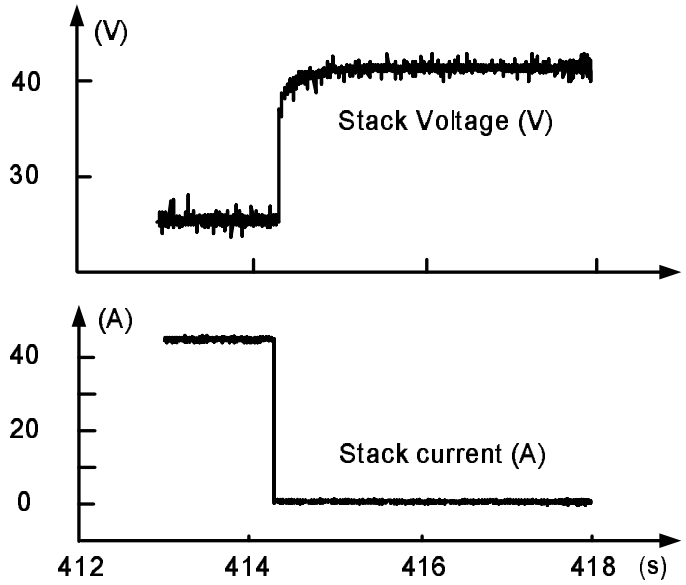

Figure 3.8: Typical waveforms of the voltage response to current interrupt

Fig. 3.8 shows the experimental waveforms recorded from an oscilloscope when current steps down from 97% (44.5A) to 0.86% (0.4A) of the rated load. Experimental data extracted from this waveforms is used to determine the electrical circuit parameters following the above method. From Eq. 3.22, $R_h = 98.7m\Omega$ and $\tau = 0.2451s$. More experimental waveforms are recorded to obtain R_h and τ at different current steps. Table 3.1 shows four sets of data obtained from the experiments. From the table, it seems that when current-interruption is used to identify electrical circuit parameters, more accurate parameters could be obtained for large current steps. That could be the reason why current-interruption always use large current step (rated load step down to open circuit) to identify the electrical circuit parameters in book [3]. An average value of the electrical parameters are finally obtained as $R_h = 98m\Omega$

and $\tau = 0.2457s$.

Table 3.1: Electrical Parameters obtained from Different Current Steps

	$I_1 - I_2$ (A)	$\Delta I(A)$	R_h $(m\Omega)$	τ (s)
1	$4.3 - 0$	4.3	94.4	0.206
2	$18 - 0$	18	100	0.2895
3	$44.5 - 0.4$	44.1	98.7	0.2451
4	$46.1 - 0$	46.1	97.6	0.2421

3.4.2 Identification of the empirical stack parameters

Once R_h and τ are determined, experimental $V - I$ data can be used to identify the following five parameters: E_o, b, m, n, ξ_3. All experimental data should be obtained in steady state. One set of experimental data is shown in Fig. 3.9 denoted as *.

It must be noticed that the pairs of V-I data are not measured at fixed temperature. One reason is that the fuel cell tested in the experiment is a commercial fuel cell stack and its cooling system controls the stack temperature within a certain range. Stack temperature of the fuel cell increases when fuel cell current increases. Hence it is not possible to measure the V-I data at fixed temperature. Another reason is that for the same fuel cell current, variation of stack voltage due to the variation of stack temperature is small. This can be proved from [16]. V-I curves of the fuel cell model

are quite close when temperature varies from 13.5^oC to 38.3^oC. Voltage difference is about $0.0017V/^oC$. Moreover, the experimental data obtained at different temperatures overlap each other for the same current load. This implies that although the simulation may show the small difference of the temperature effect on steady-state V-I curve, the dispersing of the experimental data due to the measurement noise may not reflect this difference. Similarly, the rising of the output voltage due to the temperature increase is reported to be around $0.002V/K$ in [11] for a PEM fuel cell. This number is based on the simulation of a semi-empirical model, but the experimental data shown in the paper were not sufficient enough to show the difference. For the fuel cell stack studied, the V-I curve is measured from $28.7^oC \sim 67^oC$. According to the estimation in [11], voltage variation at the same current is less than 6.3% ($(67 - 28.7) * 0.002V/1.2V * 100\%$) due to the temperature variation. If the dispersion of the measurement is considered, the parameter identification can be performed using the V-I data at different temperatures.

By curve fitting all the five parameters are determined as: $E_o = 42V$, $b = 2.61V/dec$, $m = 9mV$, $n = 0.01A^{-1}$, $\xi_3 = 0.0675m\Omega/A$.

3.4.3 Identification of temperature effect parameters

Now only parameters ΔR_h and τ_t are left to be identified. ΔR_h is the initial value of transient part in the internal resistance of the fuel cell stack, and τ_t is the time constant of the transient part. Nine different load steps are performed and ΔV is

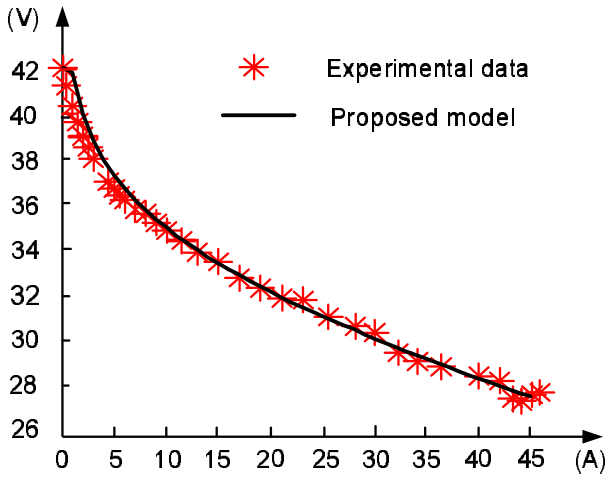

Figure 3.9: Identification of the empirical stack parameters (Fuel pressure $P_{H_2} = 4.0$ $barg$, stack temperature $\theta = 28.7^oC \sim 67^oC$)

recorded as shown in Table. 3.2.

One of the nine waveforms are shown in Fig. 3.10 (a). The undershoot ΔV is

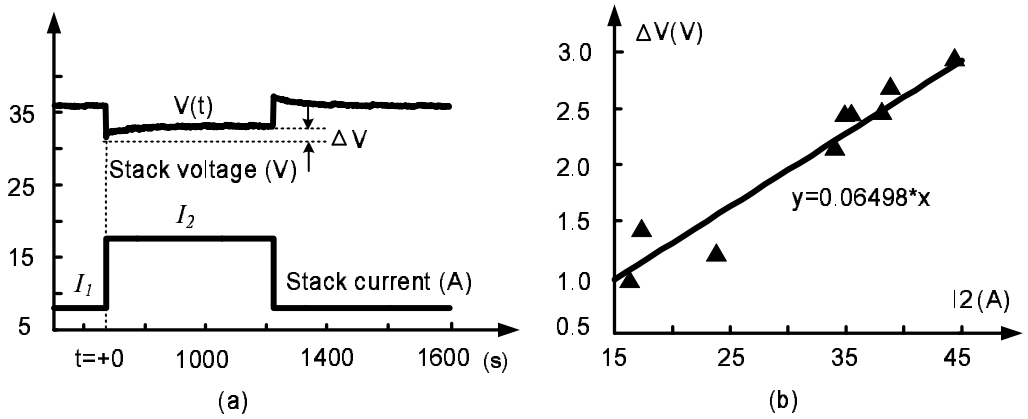

Figure 3.10: (a) Experimental waveforms used to identify temperature parameters; (b) Determination of ΔR_h

defined as the difference between the initial voltage drop at time t_0 and the final steady state voltage after the load step. Since ΔV is affected by fuel cell stack temperature, which is inherently related to current I_2, the relationship between ΔV and I_2 is

Table 3.2: Load steps to determine temperature effect parameters

	$I_1 - I_2 - I_1$ (A)	ΔV (V)
1	$0.4 - 16.3 - 0.4$	0.94
2	$8.1 - 17.4 - 8.1$	1.419
3	$14.5 - 24.3 - 14.5$	1.18
4	$16.7 - 34 - 16.7$	2.13
5	$4.1 - 34.4 - 4.1$	2.33
6	$11.2 - 34.5 - 11.2$	2.32
7	$18.8 - 38 - 18.8$	2.46
8	$9.5 - 38.3 - 9.5$	2.61
9	$0.6 - 44.6 - 0.6$	2.935

characterized from Fig. 3.10 (b) by LSE (least squared error) data fitting. Using the relationship in Fig. 3.10 (b), ΔR_h is estimated as $64.98m\Omega$. Since by observing all the experimental waveforms, it usually takes around $200s \sim 300s$ ($2 \sim 4$ times of the time constant) for the stack voltage to settle down, it is reasonable to estimate time constant τ_t as $100s$.

Finally all parameters $p_1 \sim p_9$ (as shown in Fig. 3.1) for the proposed model are

identified as:

$$\begin{cases} E_o = 42V, & R_h = 98m\Omega, & b = 2.61V/dec, \\ m = 9mV, & n = 0.01A^{-1}, & \xi_3 = 0.0675m\Omega/A, \\ \tau = 0.2457s, & \Delta R_h = 64.98m\Omega, & \tau_t = 100s. \end{cases} \tag{3.23}$$

3.5 Experimental verification of the hybrid model

Fig. 3.11 shows the voltage response of the proposed stack model to a short period of load insertion or extraction. Experimental data are obtained from both an oscilloscope and NexaMon software. The fastest sampling rate of NexaMon software is $200ms$, which is not precise enough to record the charge double layer dynamics. Hence NexaMon software is only used to record stack temperature while a Tektronix digital oscilloscope is used to record both current and voltage of the fuel cell stack. Sampling rate of current and voltage is $2ms$. As shown in Fig. 3.11, fuel cell stack temperature is relatively constant. Hence it has negligible effect on fuel cell stack voltage during the short period of time. Voltage undershoot is not observed while the first order dynamics – charge double layer dynamics is dominant. Moreover, a good correlation between the model and experimental data shows the validity of the proposed model in evaluating the charge double layer dynamics of the fuel cell stack.

Fig. 3.12 shows the voltage response of the proposed stack model to a large period of load insertion and extraction. All experimental data are obtained from NexaMon software and sampling rate is $1s$. As shown in Fig. 3.12, fuel cell temperature rises

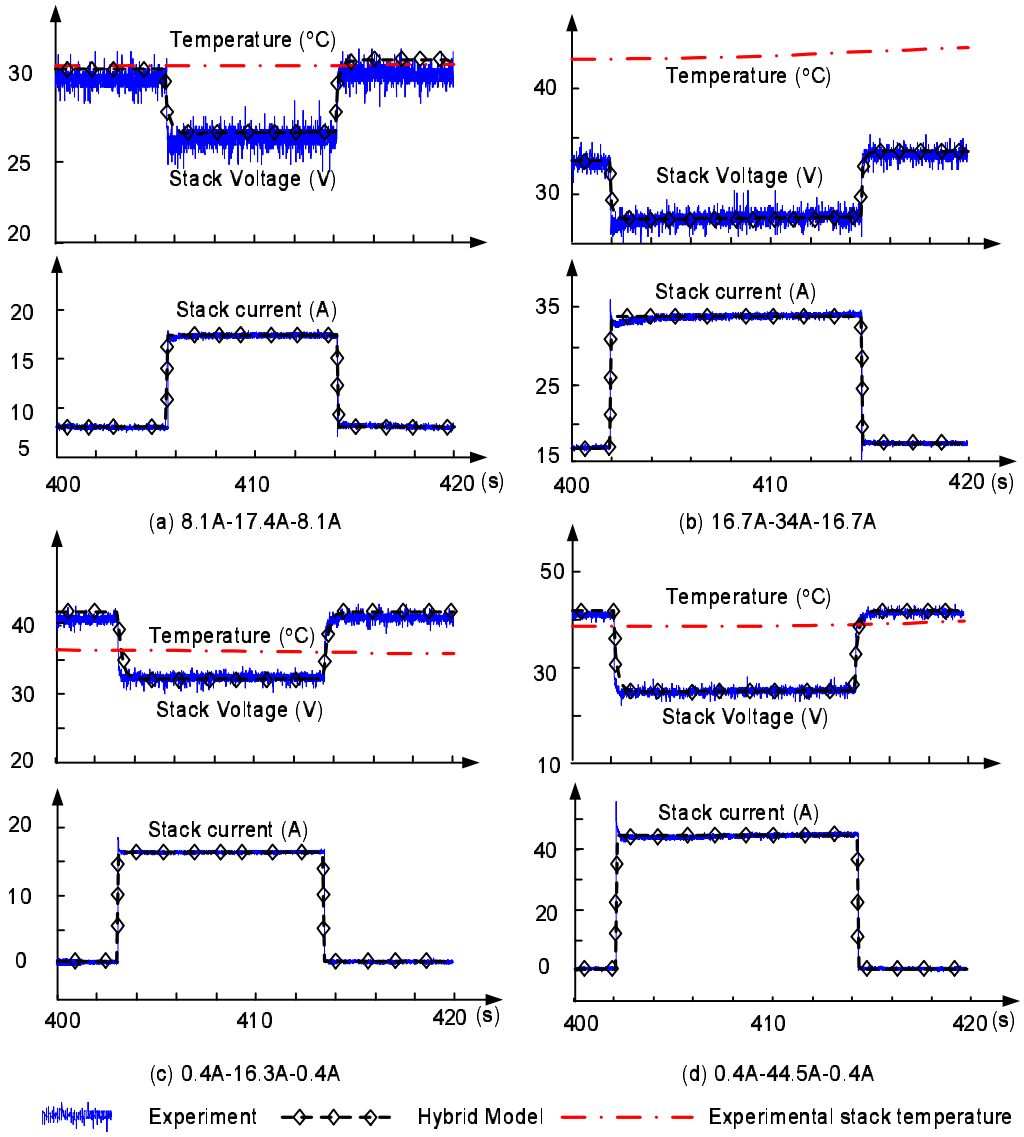

Figure 3.11: Dynamic response of the fuel cell stack model to short period of load insertion and extraction

slowly to new steady state value while the stack voltage slowly settles down in about $200s \sim 300s$. Voltage undershoot due to the temperature effect is observed for all of the current steps. Temperature effect on the stack voltage becomes dominant during the large period of load insertion. It is noticed that a maximum error of $2V$ appears

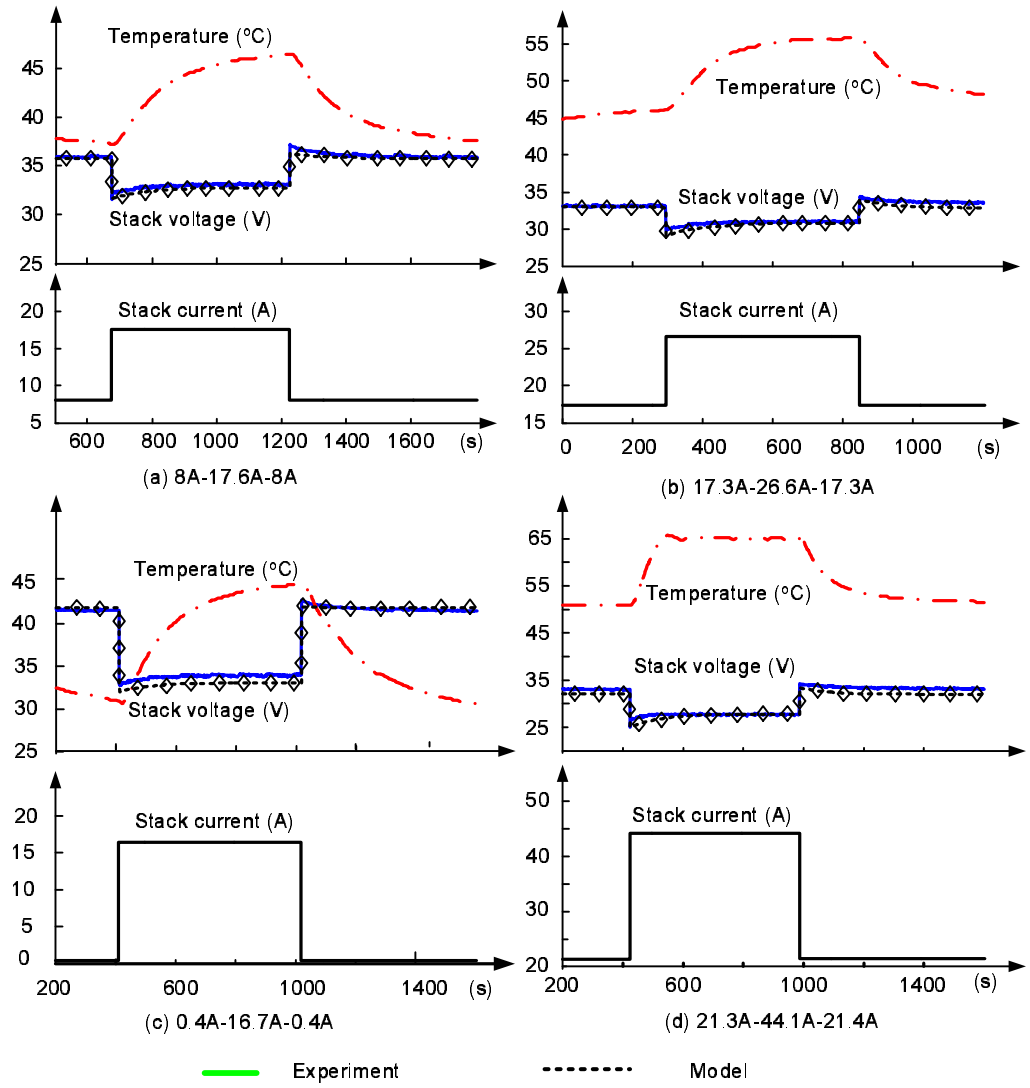

Figure 3.12: Dynamic response of the fuel cell stack model to large period of load insertion and extraction

in Fig. 3.12 (c) and (d). The error is caused by the approximation of temperature dependant internal resistance ΔR_h (Fig. 3.10) and R_h. This problem will be discussed and solved in Chapter 4. Although there is maximum error of $2V$, more than 93% accuracy can be obtained between the model and the experiment for most transient responses. The good correlation between the experiment and the model verifies the

validity of the proposed model in evaluating the stack dynamics during the large period of load insertion and extractions.

To verify the steady state performance of the hybrid model, data from dynamic experiments is used where the period of load insertion and exclusion is very large. This will produce both dynamic and steady state phases of operation. $V - I$ data pairs can be selected before the load steps up or after the stack settles down to steady state again. Take the example of Fig. 3.12 (a), two pairs of data may be selected when $t = 600s$ or $t = 1200s$. These data points are represented as □ in Fig. 3.13. In order to show correlation between the model and the experimental data, the voltage percentage error between the proposed model and the experimental data are plotted in Fig. 3.14. More than 97% accuracy can be achieved during all load range. This

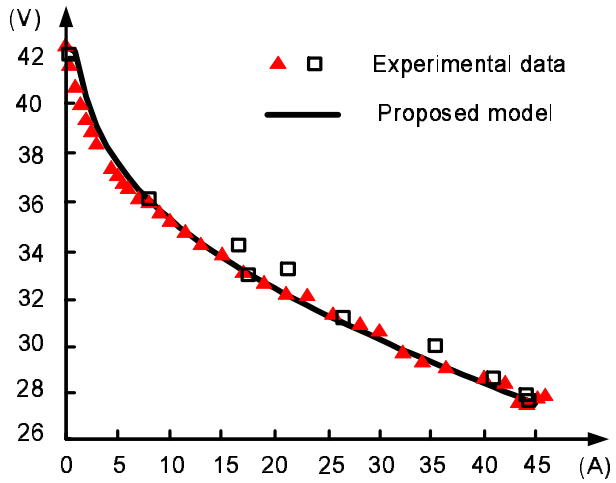

Figure 3.13: Steady state performance of the proposed fuel cell stack model (Fuel pressure $P_{H_2} = 4.0\ barg$, stack temperature $\theta = 28.7^oC \sim 67^oC$)

good correlation between the model and the experimental data indicates the validity of the proposed model in evaluating steady state performance of the fuel cell stack.

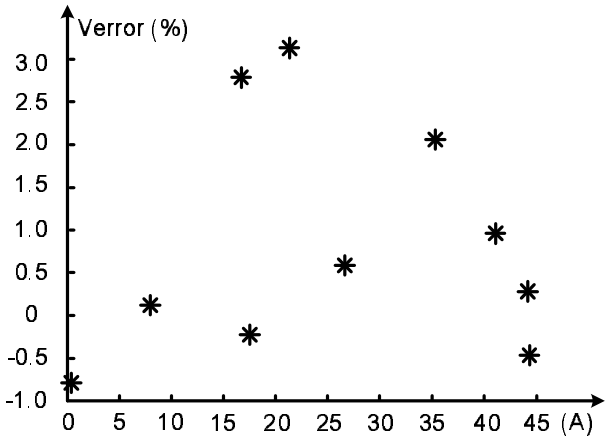

Figure 3.14: Steady state voltage error between the proposed fuel cell stack model and the experimental data

3.6 Summary

In order to obtain a simple and accurate fuel cell stack model suitable for electrical engineers, a hybrid stack model without comprehensive mathematics is proposed. By combining an empirical stack model, an electrical circuit stack model and temperature effect, this hybrid fuel cell stack model is capable of characterizing fuel cell stack's steady state performance as well as transient behavior. In this hybrid model, empirical stack model provides the characterization of the fuel cell nonlinear polarization relationship. Based on various operating point from the empirical stack model, the electrical circuit stack model regulates its "RC" parameters accordingly and reflects charge double layer dynamics. At the same time, temperature effect on the fuel cell is simulated as the modification of fuel cell internal resistance according to

the temperature variation. Interactions among these three parts and identification of the model parameters are described in details. Good correlation between the experimental data and the simulation results verified the validity of the proposed model. Although the model is designed for a specific stack, principle and method can extend to other PEMFC stacks too.

From the experimental results, a maximum of $2V$ error was observed during some of the large period of load transients. The problem may due to the linearization of the internal resistance. This problem will be solved in the next chapter.

Chapter 4

ANN PEM Fuel Cell Modelling

4.1 Introduction

The hybrid model proposed in Chapter 3, is developed with the combination of an empirical stack model and an electrical circuit stack model. The hybrid model is simple and can predict both steady state and dynamic characteristics of the fuel cell stack. However a maximum dynamic voltage error of $2V$ is observed during some of the large period of load insertions. This is due to the linear approximation of the nonlinear model parameters as explained later in Section 4.3. To solve this problem, a useful tool in nonlinear problem domain – the artificial neural network is chosen in this Chapter.

Survey on recent publications of fuel cell modelling shows that most ANN fuel cell models are for static modelling. They use ANN to achieve the fit of fuel cell

polarization curve without having to determine all system parameters [18] [19]. Two hybrid ANN models, each consisting of an ANN component and a physical component have been developed and tested in [39]. An ANN approach in [40] provides similar accuracy as the traditional analytical method in modelling a solid oxide fuel cell. An ANN model designed for a commercial PEM fuel cell system [41] shows successful performance prediction. Different ANN structure and training algorithm were discussed and compared. However the input-output mapping is not able to show dynamics of the fuel cell system. Similarly, the dynamic characteristics of fuel cell stack is also absent in [39] [40] too.

To simulate a complete model and include fuel cell dynamics using a neural network would require a large complex network and training time. Hence it is proposed to model a non-linear portion of the model using ANN and the rest of the model is based on the hybrid model developed in Chapter 3. Since the hybrid model shows good results in steady state as well as during dynamics for the full operating range, it is decided to retain its basic structure and only model its non-linear subsystem with the ANN. The aim of the research given in this chapter is to improve accuracy and flexibility of the fuel cell stack model and realize real-time implementation of the stack model.

4.2 Structure of ANN model

As shown in Fig. 3.1, the hybrid model proposed in Chapter 3 comprises of three blocks: empirical stack model, electrical circuit stack model and temperature effect. Interactions exist among all the three parts. As described in Eq. 3.17, total internal resistance R_{htot} in the empirical stack model can be represented as:

$$R_{htot} = R_h + \Delta R_h(t) = R_h + \Delta R_h \exp^{\frac{-t}{\tau_t}} . \tag{4.1}$$

It shows that R_{htot} is the summation of two parts: steady state value R_h and temperature dependant transient part $\Delta R_h(t) = \Delta R_h \exp^{\frac{-t}{\tau_t}}$. The transient part is realized by temperature effect block, as shown in Fig. 3.1. A maximum error of $2V$ is observed between the model and the experimental data during some large period of load insertions. This error is due to the linear approximation: the coefficient of transient part of the internal resistance of the fuel cell ΔR_h and the steady-state value R_h. The constant value of R_h is obtained using current-interruption technique explained in Chapter 3. While the constant value of ΔR_h is determined by data-fitting technique described in Chapter 3. That is a best fitted line is drawn which passes through most of ΔR_h values for different current step inputs. The gradient of this line is determined as constant ΔR_h as used in the hybrid model presented in Chapter 3. However in practice it is found that both R_h and ΔR_h are temperature dependant. Hence instead of relying on the constant value of R_h and ΔR_h, the inaccuracy of the dynamic model can be minimized if the transient part of the internal resistance of

the fuel cell $\Delta R_h(t)$ can adapt to vary with current and temperature. This is where the ANN comes in. By doing so, the temperature induced variation of R_h can also be compensated because the training of the ANN is performed on stack voltage level.

An artificial neural network is proposed to replace the existing temperature effect block (given in Eq. 4.1) in the hybrid model. The function of this ANN is to estimate temperature dependent transient part $\Delta R_h(t)$ in real time. Hence Eq. 4.1 can be rewritten as:

$$R_{htot} = R_h + \Delta R_h(t). \tag{4.2}$$

Where $\Delta R_h(t)$ is the output of the neural network. Block diagram of the fuel cell model is shown in Fig. 4.1. It consists of two main blocks. Block I (represented

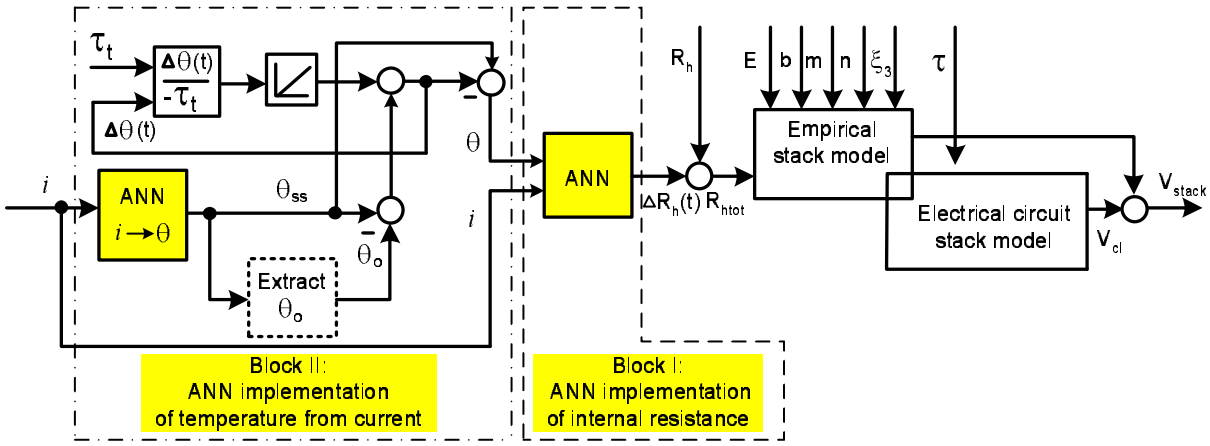

Figure 4.1: Block diagram of proposed fuel cell model

in dashed line) obtains the transient part of internal resistance $\Delta R_h(t)$ through an ANN with two hidden layers. Functions of both electrical circuit stack model and empirical stack model are not changed and are the same as in the earlier model in

Chapter 3. What is changed here is the internal resistance R_{htot} for empirical stack model. It is now the summation of R_h and the output of ANN block $\Delta R_h(t)$. While block II (represented with dashed-dot line), uses another ANN block with two hidden layers to determine temperature θ from current i. Both the blocks will be described in detail in the following sections.

4.3 ANN Model of Internal Resistance

4.3.1 Model Structure

Topology of the ANN in block I (shown in Fig. 4.1) is a multilayer perceptrons (MLP) with two hidden layers, one input layer and one output layer. Configuration of the proposed ANN is illustrated in Fig. 4.2. There are two neurons at the input

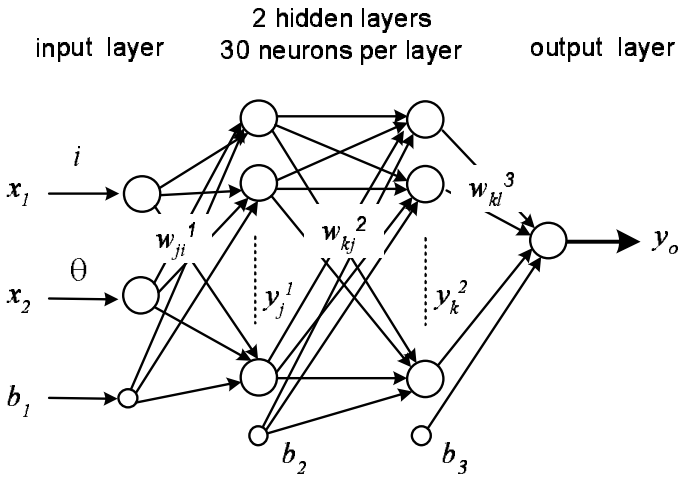

Figure 4.2: Schematic diagram of ANN structure to implement internal resistance (block I)

layer, one neuron at the output layer and 30 neurons at each of the hidden layers. The

number of hidden layers and the number of neurons used in each layer are determined by the following factors: the time needed to train the ANN, accuracy of the output results with the training data and the complexity of the parameters. This is done by trial and error during training. For single hidden layer with more neurons such as 200 neurons, training error becomes constant at about 0.0043 after 500 epochs, while for the two hidden layer structure with 30 neurons per layer, training error is 0.004 after 239 epochs. Moreover, it is found that dynamic response of the ANN model with single hidden layer is not able to model the fuel cell stack dynamic behavior satisfactorily. Hence a MLP is chosen with less neurons.

4.3.2 Selection of Training Examples

Unlike the ANN models proposed in most publications [18] [41], the ANN model designed here is not a $V - i$ curve mapping. It is a subsystem that provides the dynamic variation of the internal resistance $\Delta R_h(t)$. Two input variables are included in the network: fuel cell current i and fuel cell stack temperature θ. Before the training, sufficient training examples should be prepared. Input variables are directly collected from the experimental data while the calculation of the target $\Delta R_h(t)$ is based on the following equation:

$$\Delta R_h(t) = \frac{\Delta V}{I_2} = \frac{V(t) - V_{steady-state}}{I_2}. \tag{4.3}$$

Where $V(t)$ is the real time voltage after fuel cell current changes to I_2 (when $t > +0$), as shown in Fig. 4.3. $V(t)$ and $V_{steady-state}$ are all from experimental data. Fig. 4.3

shows one typical waveform of the fuel cell stack voltage response after a substantial time period with increased load current from I_1 to I_2. $V_{steady-state}$ is the steady state voltage after the load change and ΔV is the voltage undershoot caused by the variation of internal resistance.

Eighteen sets of experimental data listed in Table. 4.1, are used as the training

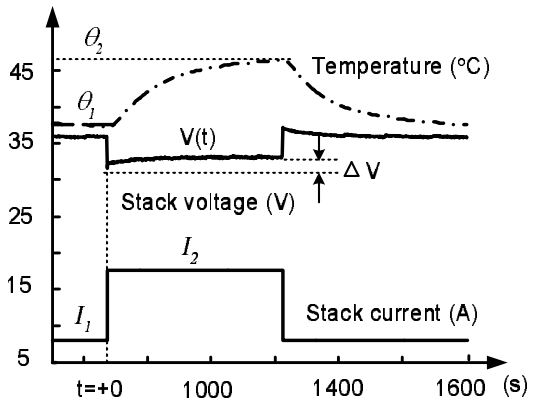

Figure 4.3: Stack voltage response to a long time interval current step (experiment)

examples. Temperature variation and desired output $\Delta R_h(t)$ related to each current step are plotted in Fig. 4.4 to show the whole picture of the training example. Since the current range of the fuel cell stack is $0 \leq I \leq 45A$, these training data are selected to cover the full operating range as possible in order to obtain good training result, as seen from Table. 4.1 and Fig. 4.4.

Table 4.1: Current steps used in the training example

No.	$I_1 - I_2 - I_1$ (A)	No.	$I_1 - I_2 - I_1$ (A)	No.	$I_1 - I_2 - I_1$ (A)
1	16.7-35.3-16.7	2	0.4-16.4-0.4	3	18.4-41-18.6
4	21.3-44.1-21.3	5	0.4-44.3-0.4	6	4.1-34.4-4.1
7	7.8-27.9-7.9	8	10.8-41.3-10.9	9	12.3-21.5-12.2
10	4-16.3-4	11	5.3-28.4-5.4	12	8-17.6-8
13	11.6-23.8-11.6	14	8-37.3-8	15	8-25.2-8
16	11.9-21.1-11.9	17	15.4-24-15.4	18	15.1-31.6-15.4

4.3.3 Training of the Network

Back propagation Levenberg-Marquardt training algorithm is used to train the proposed neural network in Fig. 4.2. Weights that link the neurons are adjusted under the influence of the training vector and the error signal between the desired response from training examples and the actual response from the network. The weight adjustment is carried out iteratively after processing the whole training data set (batch mode training). This results in a chain reaction of weight adjustments such that each of the ANN weight is moved along the negative gradient of the performance function (Eq. 4.7) until it reaches required criteria. Eventually weight adjustment results in an actual output $\Delta R_h(t)$ closer to the desired response.

Computations of the training process of the proposed network is summarized as follows:

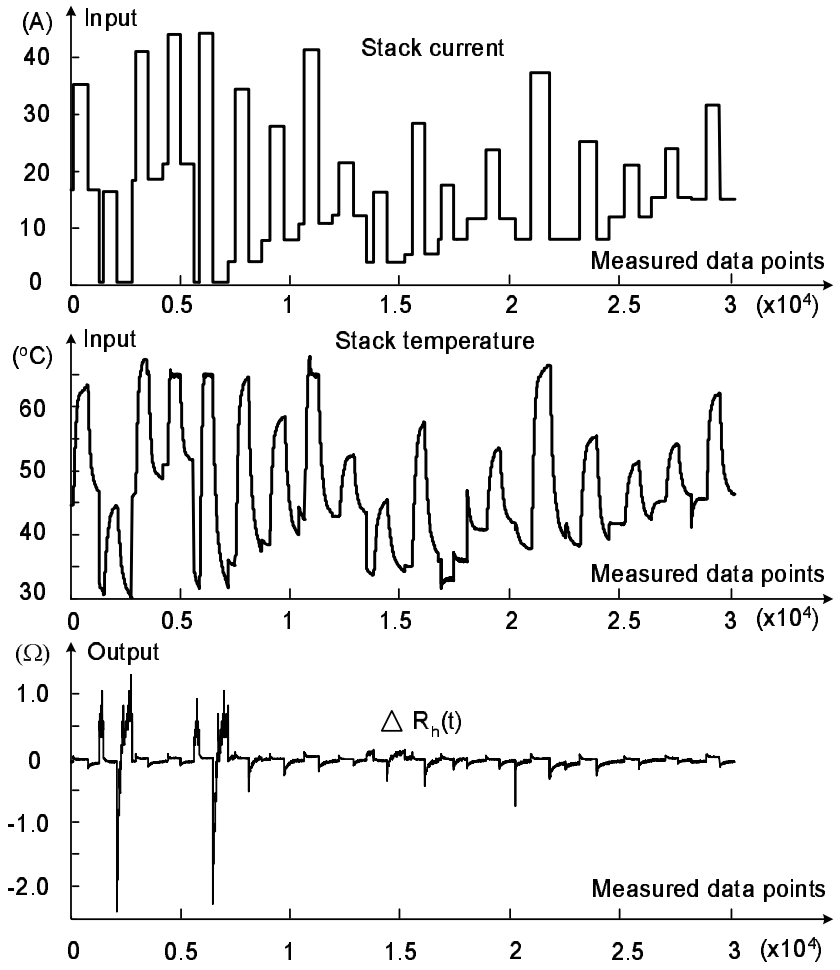

Figure 4.4: Training examples (experimental data): input vectors: stack current and stack temperature; output vector: ΔR_h

1. Initialize the weights randomly.

2. During the forward pass, calculate the output of the network for the nth process

at different layers.

$$y_j^1(n) = \varphi\Big(\sum_{i=1}^{n_i} w_{ji}^1(n)x_i\Big), \tag{4.4}$$

$$y_k^2(n) = \varphi\Big(\sum_{j=1}^{n_j} w_{kj}^2(n)y_j^1(n)\Big), \tag{4.5}$$

$$y_o(n) = \varphi_o\Big(\sum_{k=1}^{n_k} w_{lk}^3(n)y_k^2(n)\Big). \tag{4.6}$$

Where y_j^1 and y_k^2 are outputs at first and second hidden layer respectively, and y_o is the output at the the output layer. w_{ji}^1 are weights connection from neuron i at input layer to neuron j at first hidden layer. Similarly, w_{kj}^2 are weights connection between the two hidden layers and w_{lk}^3 are weights between the second hidden layer and the output layer. n_i, n_j, n_k are neuron numbers at the input layer and the hidden layers respectively. $\varphi(\cdot)$ is the hyperbolic tangent sigmoid function $f(x) = \dfrac{2}{1+e^{-2x}} - 1$ for all hidden layers while $\varphi_o(\cdot)$ is the identity function $f(x) = x$ used for output layer. The bias b_1 for first hidden layer shown in Fig. 4.2 has already been reformulated as a new neuron $x_{i+1} = 1$ at the input layer and the weights connection are $w_{j,i+1} = b_j$ [42]. Similar reformulation can be applied to b_2 and b_3.

3. Define the performance function as the mean squared error of the network.

$$E(n) = \frac{1}{N}\sum_{p=1}^{N}\Big(T_p(n) - y_p(n)\Big)^2. \tag{4.7}$$

Where $T_p(n)$ is the target value with pth pattern at nth iteration while $y_p(n)$ is the result at output layer with pth pattern at nth iteration. N denotes the

total number of pattern or examples.

4. The error signal generated is propagated back through the network. Weights of the network will be updated according to the back-propagation algorithm in [42]. Weight correction $\Delta w_{ji}^{l}(n)$ applied to $w_{ji}^{l}(n)$ can be written as:

$$\Delta w_{ji}^{l}(n) = -\eta \frac{\partial E(n)}{\partial w_{ji}^{l}(n)}, \tag{4.8}$$

$$w_{ji}^{l}(n+1) = w_{ji}^{l}(n) + \Delta w_{ji}^{l}(n). \tag{4.9}$$

   Where $\eta = 0.01$, is the learning rate.

5. Repeat the above steps until the stopping criteria is met: either when error $E(n)$ is less than 4×10^{-3} or when the maximum number of training epochs is greater than 500.

Fig. 4.5 shows the comparison of training performance of two ANN structures: one is the proposed structure with two hidden layers and 60 neurons in total; the other structure is single layer with 200 neurons. From Fig. 4.5, it is seen that after 239 epoches, mean squared error of the proposed structure has already reached the error goal of 0.004, while about 20% error offset remains for the single layer structure.

Once the training of neural network is finished, the input-output examples can be dispensed and the network can deal with the input data by itself. MATLAB neural network toolbox is used to train the network. "Newff" is used to create a feed-forward back propagation network. The network structure, training function, learning rate

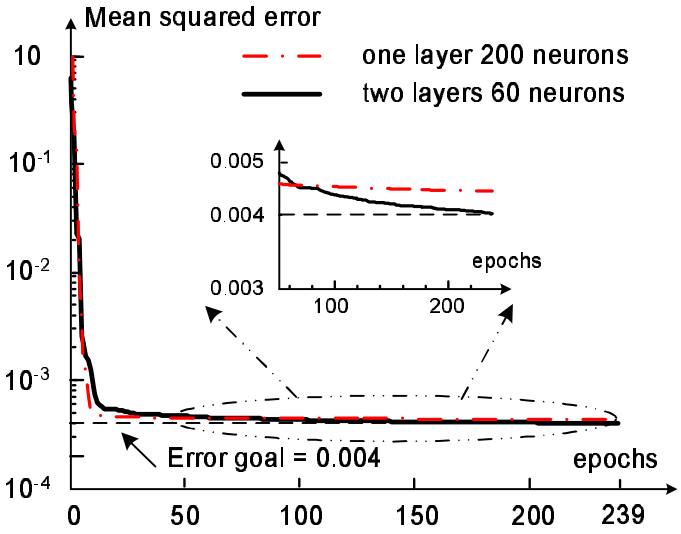

Figure 4.5: Training performance of the ANN structure

etc. can all be defined in this command. "NNtool" opens the network/Data Manager window which allows us to import, train and export neural networks and data. Since the ANN structure has inherited the fuel cell characteristics from training process, desired output could be recognized even for new input data. This is verified by experimental results in the following section.

4.3.4 Experimental verification

The same fuel cell system, as described in Chapter 3 is used for the experiments. Experimental data used for ANN training and test verification are all obtained from NexaMon, which transmits fuel cell working status to computer through RS485 communication cables.

Fig. 4.6 shows the experimental verification of fuel cell stack voltage response

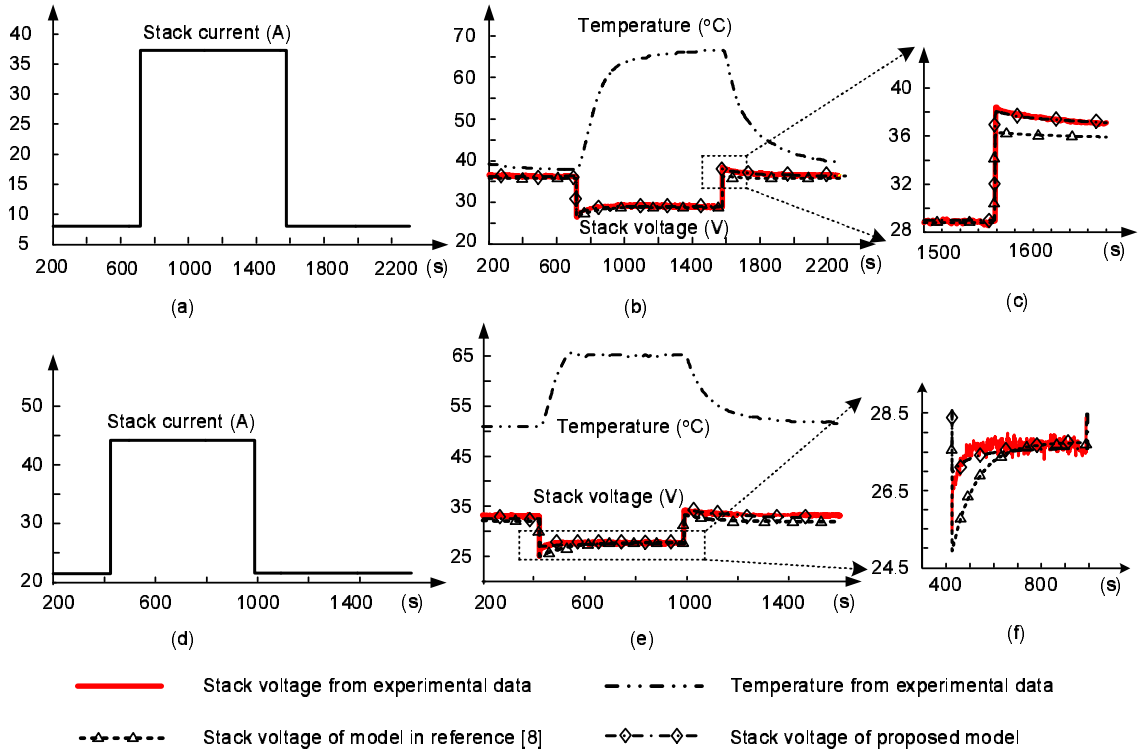

Figure 4.6: Dynamic response of ANN fuel cell stack model to large period of load insertion and extraction. (a)∼(c) Stack current, stack voltage and stack temperature during current step $8.0A - 37.3A - 8.0A$; (d)∼(f) Stack current, stack voltage and stack temperature during current step $21.3A - 44.1A - 21.3A$

for slow load step changes. By zooming in the dynamic part in Fig. 4.6 (c) and (f), it is noticed that the maximum voltage error of the proposed model is only around $0.5V$. Compared to $2V$ error of the hybrid model described in Chapter 3, accuracy is improved. In order to evaluate errors during the whole process of these two current steps, Table 4.2 compares the mean squared error mse between fuel cell stack models (ANN model proposed here and hybrid model in Chapter 3) and the experimental data. It is clear to see that significant improvement on dynamic accuracy is achieved for the ANN model.

Fig. 4.7 shows the experimental results of the proposed model to load steps

Table 4.2: Comparison of Mean Squared Error of ANN model and hybrid Model

Current steps	ANN model	Hybrid model in Chapter 3
$8.0 - 37.3 - 8.0A$	$mse = 0.089V^2$	$mse = 0.5118V^2$
$21.3 - 44.1 - 21.3A$	$mse = 0.2155V^2$	$mse = 1.1484V^2$

which are not in the training set. Two sets of new current steps are tested, as seen in Fig. 4.7. Good correlation is observed between the ANN model and the experimental data. It verifies the capability of the proposed model to work with the new input conditions.

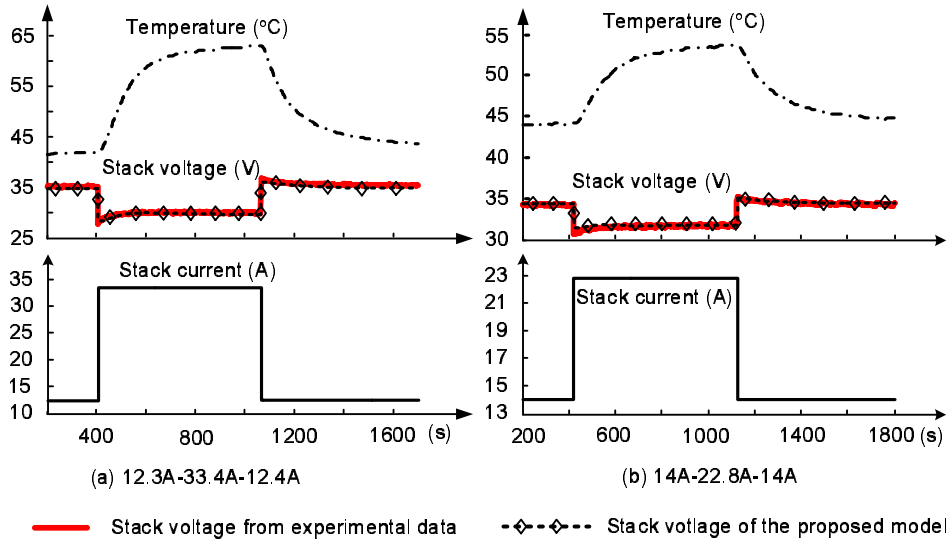

Figure 4.7: Dynamic response of the proposed stack model in recognizing new load steps. (a) Stack current, stack voltage and stack temperature during current step $12.3A - 33.4A - 12.4A$; (b) Stack current, stack voltage and stack temperature during current step $14A - 22.8A - 14A$.

4.4 ANN Model for Temperature Estimation

In earlier Section 4.3, the nonlinear structure within the hybrid model of a PEM fuel cell has been modelled by using an ANN block. It is noticed that training vectors for this ANN include both current i and temperature θ, as shown in Block I in Fig. 4.1. However in practical applications, it is not convenient to measure fuel cell stack temperature. Hence an interesting question arises: is it possible to convert this direct input vector– temperature θ to an intermediate input vector by finding out the relationship between fuel cell current and temperature? By doing so, temperature effect on the stack can be finally represented as fuel cell current effect. This is realized by block II as shown in Fig. 4.1.

4.4.1 ANN structure

Fuel cell temperature can be represented as a first order exponential function [43]:

$$\theta = \theta_{ss}(1 - e^{\frac{-t}{\tau_t}}) + \theta_0 e^{\frac{-t}{\tau_t}}. \tag{4.10}$$

Where θ_0 and θ_{ss} are initial and steady state temperature of fuel cell stack after the load step, while τ_t is the time constant. Since fuel cell temperature can be represented as a function of parameters θ_0, θ_{ss} and τ_t, it is possible to find the relationship between θ and i by knowing the relationship between parameters θ_0, θ_{ss}, τ_t and current i. This is where the ANN $i \rightarrow \theta$ comes in (Block II in Fig. 4.1).

Structure of ANN $i \rightarrow \theta$ is shown in Fig. 4.8. It consists of one input layer, two

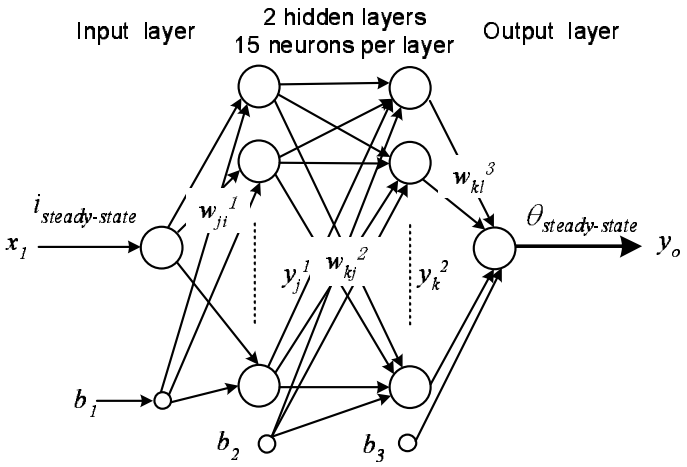

Figure 4.8: ANN structure to map the steady state current to steady state temperature (block II)

hidden layers and one output layer. There are 15 neurons at each of the hidden layers and one neuron at the output layer. Input to the neural network is steady-state current and the output of the network is steady-state temperature. The function of this ANN $i \rightarrow \theta$ is to map the operating current of the fuel cell to the steady state temperature. For example in Fig. 4.3, fuel cell currents I_1 and I_2 are mapped to temperatures θ_1 and θ_2 through the ANN $i \rightarrow \theta$. Tab. 4.3 shows the training patterns during the training process. Since the current range of the fuel cell stack is $0 \leq I \leq 45A$, these data are selected to cover the full operating range as possible. Using the same training process described in Section 4.3, a trained neural network as shown in Block II in Fig. 4.1 can be obtained.

It must be noticed that in Block II, there is a sub-block designed to extract the initial temperature θ_0 (shown as the dot line). The initial temperature θ_0 is nothing but the past steady state temperature before any current step occurs. While the past

Table 4.3: Training example for ANN model of temperature estimation

No.	I (A)	θ (C^o)	No.	I (A)	θ (C^o)	No.	I (A)	θ (C^o)
1	0.4	30.99	2	8.8	39.33	3	11.9	41.74
4	16.7	44.56	5	18.4	44.64	6	19.0	49.52
7	21.1	50.9	8	21.3	51.48	9	29.3	60.18
10	35.3	63.4	11	41	65.12	12	44	65.12

steady-state temperature is correlated to the past fuel cell current and can be obtained via the ANN $i \rightarrow \theta$. Hence this sub-block and ANN $i \rightarrow \theta$ together can remember the initial temperature θ_0 by remembering the past fuel cell current operating conditions. After θ_0 and θ_{ss} are all determined, Eq. 4.10 can be rewritten as:

$$\theta = \theta_{ss} - (\theta_{ss} - \theta_o)e^{\frac{-t}{\tau_t}}, \tag{4.11}$$

$$= \theta_{ss} - \Delta\theta(t). \tag{4.12}$$

Because

$$\frac{d\Delta\theta(t)}{dt} = \frac{\Delta\theta(t)}{-\tau_t} \tag{4.13}$$

Using Laplace transform,

$$\Delta\theta(s) = \frac{\Delta\theta(s)}{-\tau_t} \cdot \frac{1}{s} \tag{4.14}$$

Eq. 4.14 can be realized by using the integrator function shown in Block II of Fig. 4.1. Now fuel cell temperature becomes an intermediate input vector and the temperature effect on the stack has been represented as fuel cell current effect.

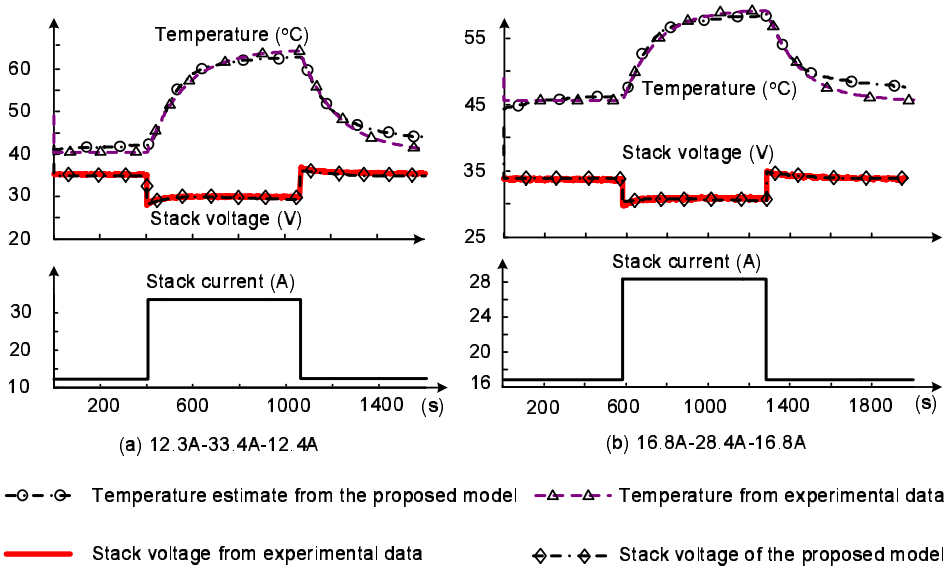

Figure 4.9: Comparison between temperature from experimental data and estimated temperature of the proposed model. (a) Stack temperature, stack current and stack voltage during current step $12.3A - 33.4A - 12.4A$; (b) Stack temperature, stack current and stack voltage during current step $16.8A - 28.4A - 16.8A$.

4.4.2 Experimental results

Fig. 4.9 shows voltage and temperature responses of the proposed fuel cell model with only one input vector: fuel cell current i. From this figure, it can be seen that temperature from proposed model can match the experimental value with small errors. This verifies the capability of ANN $i \rightarrow \theta$ to obtain fuel cell temperature by "sensing" fuel cell current. Moreover, a good agreement is observed between the fuel cell stack voltage of the proposed model and the experimental data.

4.5 Real-time Implementation of the ANN Model

In the previous sections, an ANN fuel cell model is developed to model some non-linear structures within the hybrid model of a PEM fuel cell. It improves accuracy and allows the model to work with varying operating conditions. For converter design and dynamic control, it would be very valuable to implement the same in real-time. A dSPACE-1104 system is used for the real-time implementation. The dSPACE's realtime interface (RTI) is used to link between the dSPACE' realtime hardware and the MATLAB/Simulink development software.

Experimental setup is shown in Fig. 4.10. S_1 and S_2 are used to switch on/off the load resistance network according to different current step requirement. The ANN

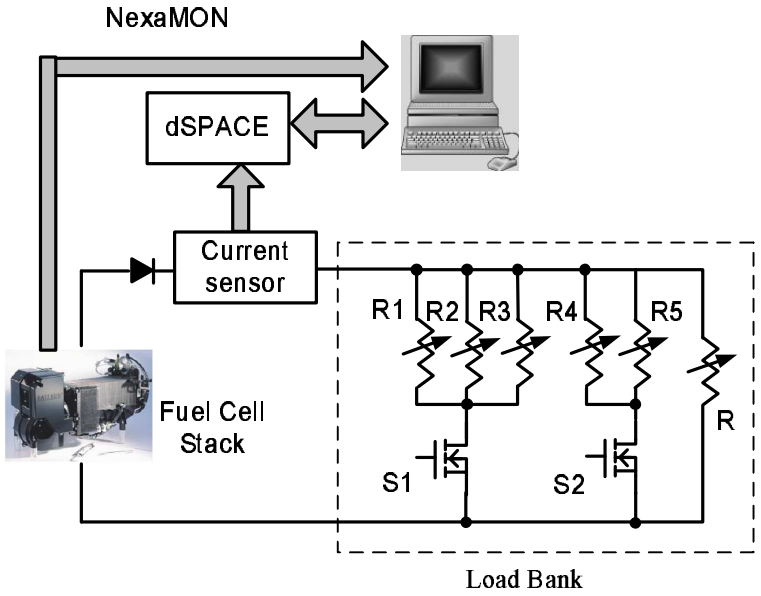

Figure 4.10: Platforms for implementation of a real-time ANN fuel cell model

fuel cell model is programmed and realized on the dSPACE system. While the in-

put to the real-time model is the measured fuel cell current. The fuel cell current ($0A \sim 50A$) is sensed in real-time through a current sensor and converted to a signal between $0V \sim 9V$. It is fed to the model via the A/D converters in the dSPACE system. The signal is conditioned using the appropriate conversion factor and fed to the ANN fuel cell model and the real-time stack voltage is obtained. At the same time, the actual stack temperature, stack voltage and other parameters are extracted using the NexaMon. Finally, the real-time ANN model is verified by comparing the results from the real-time model simulated by dSPACE and the actual parameters extracted by NexaMon.

Fig. 4.11 shows the comparison of stack response between the dSPACE model and the experimental data. From Fig. 4.11, it is noticed that a good correlation is observed between the real-time model and the experimental data. Although the estimated temperature of the real-time model does not exactly match the experimental temperature, stack voltage predicted by the real-time model agrees quite well with the actual value.

4.6 Summary

An ANN PEM fuel cell model is proposed in this chapter to model the nonlinear behavior of a hybrid model. The hybrid model is a combination of an empirical stack model, an electrical circuit stack model and temperature effect. Hence it is

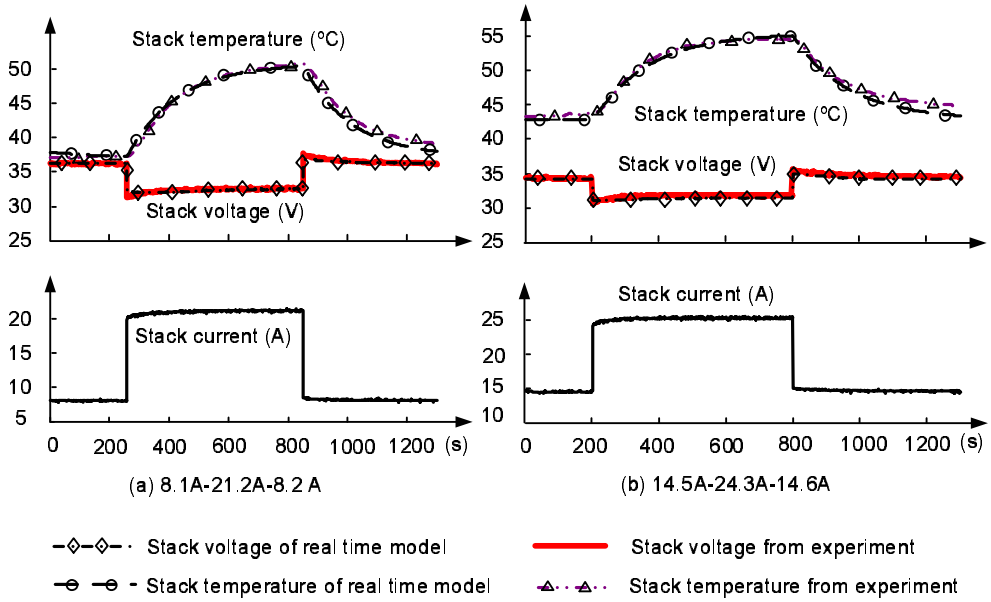

Figure 4.11: Comparison between real-time dSPACE model and experimental data (a) Stack temperature, stack current and stack voltage during current step $8.1A - 21.2A - 8.2A$; (b) Stack temperature, stack current and stack voltage during current step $14.5A - 24.3A - 14.6A$.

capable of characterizing both steady state and dynamic performance of the fuel cell stack. Due to the linear approximation of the nonlinear model parameters, the hybrid model shows errors during some of the large period of load insertions. Therefore by retaining the basic structure of the hybrid model, the nonlinear subsystem is modelled with ANN to improve the model dynamic accuracy and flexibility. Two ANN blocks are used: one with two hidden layers and 30 neurons at each layer is proposed to obtain the nonlinear cell internal resistance. The other block, two hidden layers with 15 neurons per layer, is used to map the relationship between fuel cell current and temperature. In doing so, fuel cell temperature effect on the stack is finally represented as fuel cell current effect by sensing fuel cell current via an ANN block.

In order to help the converter design and dynamic control, the ANN model is also implemented in real-time on a dSPACE-1104 system. Good correlations are achieved between the real-time ANN model and the experimental results.

Chapter 5

Survey of DC/DC Converters

5.1 Requirements of the Selection of DC/DC Converter Topology

DC/DC converter is one of the important components for a fuel cell based power supply [44] [45]. It allows us to obtain a desired level of DC voltage without having to increase the stack size. However due to the inherent characteristics of the fuel cell, not all converters can be used. Following criteria are required when choosing DC/DC converter topologies for a fuel cell based power supply:

- **Large boost ratio**

  For a PEM fuel cell stack, the DC output is usually around several tens of volts. When fuel cell stack is connected with other electrical loads, a regulated 400V DC is normally required. Hence a large boost ratio from ten to twenty is

necessary for the DC/DC converters.

- **Low input current ripple**

  The ripple current seen by the fuel cell stack due to the switching of the DC/DC converter has to be low [46]. One possible reason of this is because a higher hydrogen consumption is observed when the fuel cell current has a higher current ripple. Some test is reported in Appendix A. According to [47], fuel cell current ripple plays an important role in the catalyst lifetime of fuel cell plates. In particular, sharp current rise/fall and large magnitude of high frequency current ripple should be avoided. Furthermore, fuel cell current should be strictly nonnegative and should not exceed the maximal current limit for a certain maximal fuel flow rate. Moreover, since fuel cell current is proportional to hydrogen input, the amount of hydrogen generated in a direct hydrogen system could be better controlled if the fuel cell stack current is directly controlled [46].

- **Isolation**

  A transformer coupled converter not only realizes the electrical isolation between the fuel cell and the high voltage output side, but also allows series connection at the output of DC/DC converters.

5.2 Survey of DC/DC Converter Topologies

There are currently two groups of converters used for a fuel cell based power supply: voltage-fed converters and current-fed converters.

5.2.1 Voltage-fed DC/DC Converter Topologies

There are several kinds of voltage-fed DC/DC converter topologies used in fuel cell systems such as half bridge converters, flyback converters, push-pull converters, three phase converters and full bridge converters. Circuit diagram of these topologies are shown in Fig. 5.1.

The half bridge converter (Fig. 5.1 (a)) is a good candidate for low power systems. However by operating the two switches asymmetrically, it may create unbalance problems on the high frequency transformer and requires a semiconductor device with twice of the current rating as compared to full bridge converters [48]. The flyback converter (Fig. 5.1 (b)) is popular particularly at low power level less than $75W$ [49]. With simple structure and only one switch, this converter is usually used to achieve high output voltage. However the leakage inductance of the coupled inductors can induce high voltage stress as well as high loss. In order to improve the efficiency, authors in [50] proposed a new converter which is similar to an active-clamp converter. It utilizes one additional diode and one coupled winding to replace the active switch. By doing so, the leakage energy is recovered with low circulating current. With the lower voltage stress of the switch and the improved reverse-recovery of the output

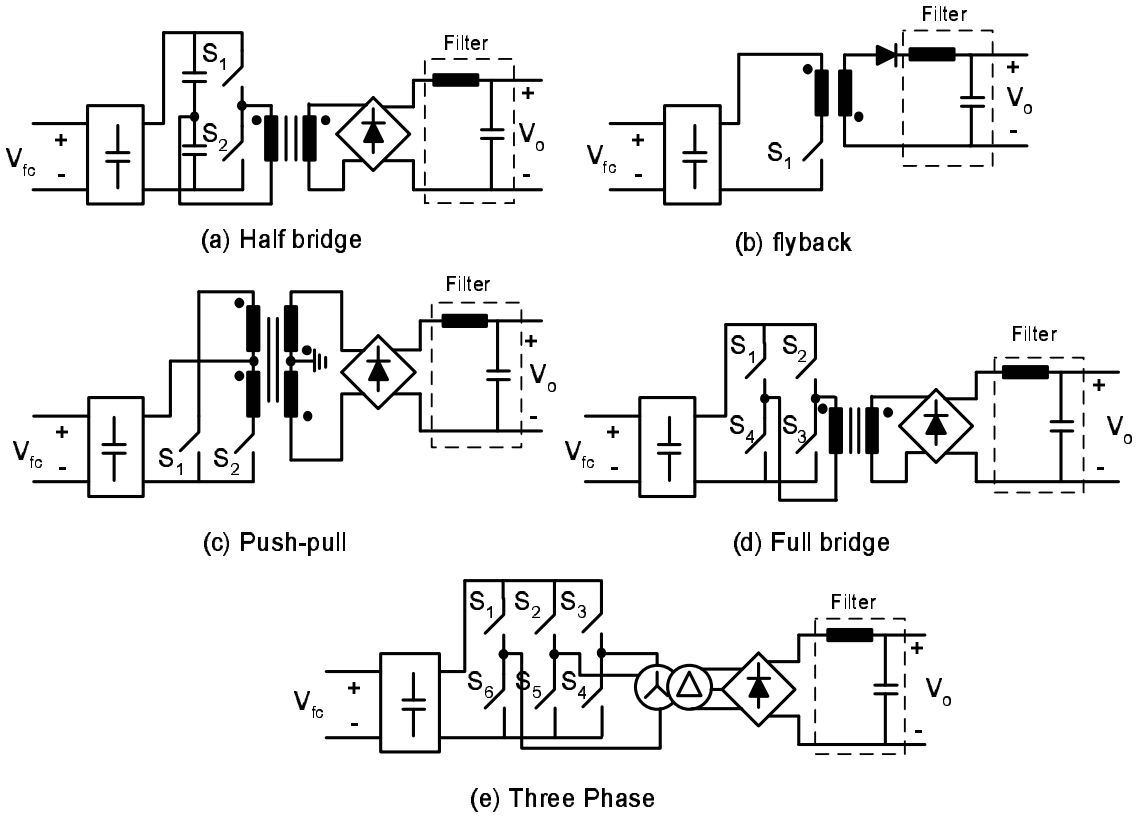

Figure 5.1: Voltage-fed DC/DC Converter Topologies in Fuel Cell Systems

rectifier, a higher efficiency can be achieved. Another converter topology which was claimed to have high boosting output voltage, component utilization and high efficiency characteristics [51], is a superposition of sepic converter and flyback converter. Push-pull converters (Fig. 5.1 (c)) also work well for low power systems [52]. In [53] [54], they are used to boost fuel cell stack voltage from $48V$ to $200V$ at high switching frequency. Since the push-pull converter utilizes center-tapped transformer and the windings of the two halves cannot be symmetrically wound. A slightly unbalanced excitation at high power can cause saturation of the transformer [55]. To solve this

problem, the authors in [56] use three paralleled push-pull converters for high power systems. Moreover, a coupled inductor is employed on the secondary side of the transformer to ensure that there is no significant imbalance between the two device currents. The three phase DC/DC converter (Fig. 5.1 (e)) has attractive characteristics like small current ripple, reduced filter size and evenly divided switch stress [57]. Although it appears to be better of current-sharing, the driver circuit and control design become more complicated as the phase number increases. The application of the asymmetrical duty cycle to the three phase DC/DC converter was presented in [58]. The converter combines the advantages of the three phase configurations with the ZVS commutation of the main switches for a wide load range.

Voltage-fed full bridge DC/DC converters (Fig. 5.1 (d)) are popularly used in fuel cell energy systems [32] [59] [60] [61] [62] [63] [64]. Because the devices are fully utilized, and the switching losses can be eliminated by adopting soft-switching techniques. Since this kind of topology is a transformer isolated "buck" converter, it is commonly used in converters producing low voltage. When a high output voltage is required, the step-up action can only be performed by the transformer turns ratio. Hence a high turns-ratio transformer is necessary for the voltage-fed full bridge topology, which increases leakage inductance and transformer loss. Another disadvantage, which is common for all voltage-fed converters, is the lack of direct control of input current. Not only a large LC filter should be put on the output side, large capacitors are also needed on the input side to obtain low switching current ripple.

5.2.2 Current-fed DC/DC Converter Topologies

Due to the requirement of direct control of input current and high boost ratio, a current-fed DC/DC converter shows its advantages. Several current-fed DC/DC topologies are found in the literature survey: simple boost converters, two phase boost converters, current-fed push-pull converters, current-fed half bridge converters, cascaded boost converters and current-fed full bridge converters. Circuit diagram of these topologies are shown in Fig. 5.2. The presence of a large inductance at the input causes a smaller current ripple in continuous conduction mode. Moreover the input current can be controlled.

Current-fed half bridge converters (Fig. 5.2 (a)) and current-fed push-pull converters (Fig. 5.2 (b)) are both good candidates for fuel cell applications at low power level [31] [65]. The simple boost converter (Fig. 5.2 (c)) utilizes the least components to boost fuel cell voltage [66] [67]. But boost ratio and the delivered power are limited due to the high stress of the switch. Although the two phase boost converter (Fig. 5.2 (d)) can be utilized to reduce the input current ripple and the size of passive components [52] [68] [69] [70], it is still difficult to achieve high boost ratio. In order to solve this problem, cascaded boost (Fig. 5.2 (e)) with two stage converters is proposed [71] [72]. A simple boost converter is usually used as the first stage which is interfaced with the fuel cell. While the second stage can be an isolated half bridge converter or a push-pull converter, which is mainly used to step up the output voltage. Although the cascaded converter has low stress of the switch and simple control method, it

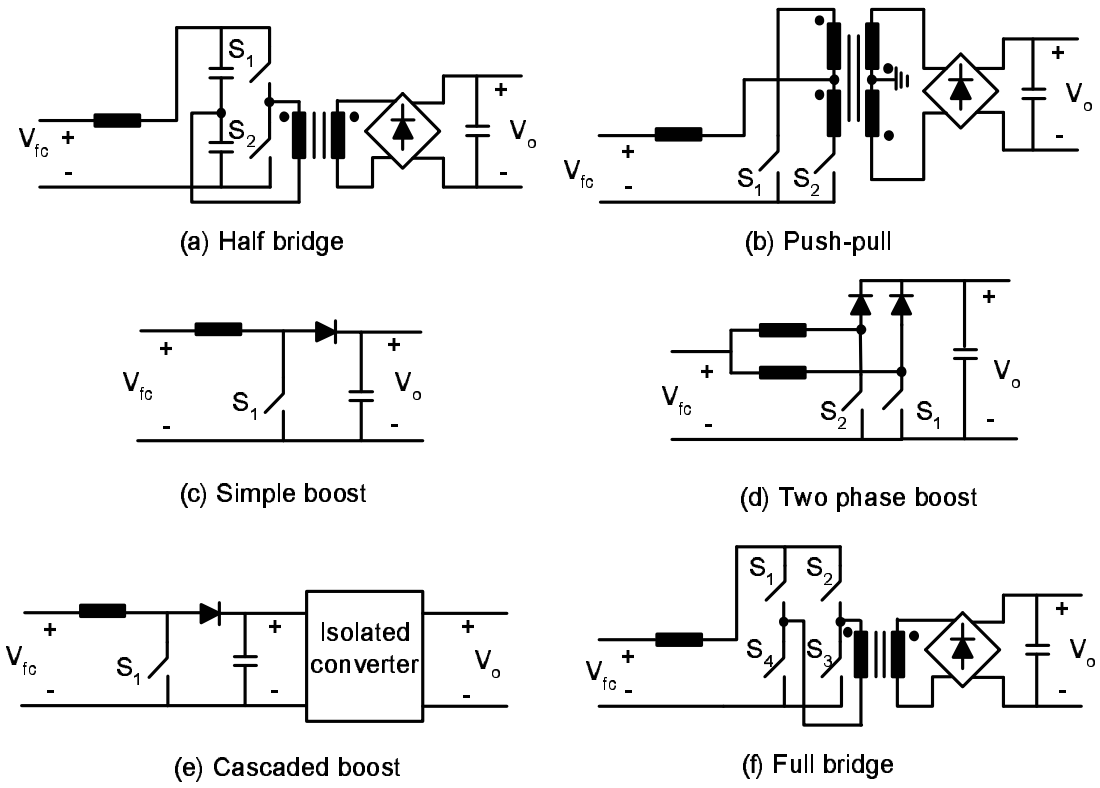

Figure 5.2: Current-fed DC/DC Converter Topologies in Fuel Cell Systems

increases the total converter size and reduces the efficiency.

Current-fed full bridge converters (Fig. 5.2 (f)) are popular in applications of power factor correction and battery charger [73] [74] [75] [76]. Input current ripple can be reduced due to the existence of the input inductor. More important, this converter is an isolated "boost" converter. Hence voltage step-up can be performed from both boost action and the winding ratio of the transformer. In doing so, transformer turns ratio can be much lower than that in a voltage-fed full bridge converter. Therefore leakage inductance and power loss of the transformer can be reduced. Detailed comparison of pros and cons between current-fed and voltage-fed full bridge

converters is shown in Table. 5.1.

Despite its advantages, the current-fed full bridge topology is seldom used in a

Table 5.1: Comparison between voltage-fed and current-fed full bridge converters

	Current-fed Full Bridge	Voltage-fed Full Bridge
Components	High current inductor	Bulky input capacitors
Switching stress	High voltage stress	High current spikes
Start-up	Cannot start with low output voltage	no start up problem
Transformer	Low winding ratio	high winding ratio
Characteristics	A boost converter	A buck converter
Signals	Overlap to charge the inductor	Dead time to avoid short-circuit

fuel cell system except as a battery charger. This can be attributed to two reasons: high current inductor and additional start-up circuit. High current inductor results in large core volume and bulky size. While the reason of using an additional start-up circuit is to eliminate the large inrush current during the initial stage when the output voltage is lower than the input voltage. Several start-up schemes have been proposed for current-fed converters. For low power boost converter, a thermistor or a resistor is usually put on the input side to limit the inrush current [77] [78] [79]. But for high power converter, where input current is high, putting a thermistor or resistor is not an efficient way due to the high power loss of the thermistor/resistor. L. Zhu [80] proposed a new start-up scheme by introducing a flyback winding coupled with the input inductor choke. Only after output capacitor is gradually charged up to rated

value then the circuit switches to normal boost operation. However the use of an additional circuit for start-up increases the total volume of the converter and control complexity. Other start-up schemes that designed for different isolated current-fed converters, also use additional circuits to eliminate the large inrush current during start-up [81] [82].

5.2.3 Z-source Converter

Z-source converter (Fig. 5.3) employs an impedance network to couple the converter main circuit to the power source, hence providing unique features that cannot be obtained in traditional voltage-fed and current-fed converters [83] [84] [85]. Although the Z-source concept can be extended to DC-DC, DC-AC or AC-DC appli-

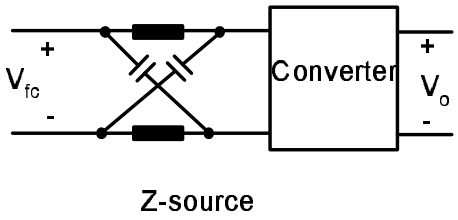

Figure 5.3: Z-source Converter

cations [83], the most popular application is Z-source inverter. Not only because the Z-source inverter can produce an AC voltage greater or less than the input voltage, but also because it eliminates the use of DC/DC boost converter, which is usually put between the input voltage and the normal inverter. Hence efficiency of the overall system can be improved. But total voltage gain of the Z-source inverter is reported

to be less than five [86], which is not quite suitable for applications that require large boost ratio. On the other hand, since the Z-source inverter can be connected directly to fuel cell stack without the boost DC/DC converter, it seems unnecessary to implement a Z-source DC/DC converter between the fuel cell stack and the other inverters. By doing so, the advantage of the Z-source inverter will be compromised.

5.3 Problem Definition

From the above survey, it is found that:

- Voltage-fed full bridge converter can fully utilize the switching devices and soft-switching techniques, which is a popular candidate for the fuel cell system. However the input current cannot be directly controlled. Not only a large LC filter should be put on the output side, large capacitors are also needed on the input side to obtain low switching current ripple. Moreover, the isolated " buck" characteristics of the voltage-fed full bridge converter makes it inefficient for applications requiring large boost ratio.

- Current-fed converter maybe a good choice for a fuel cell based power supply due to its direct control of input current. Among them, current-fed full bridge converter has the potential advantage for high power system due to its large boost ratio. However the bulky input inductor and additional start-up circuit restrict further application of current-fed full bridge DC/DC converters.

Based on these problems, one aim of our research is to develop a current-fed full bridge DC/DC converter with small input current ripple and high efficiency. This converter should also have small magnetic components and soft start-up capability.

5.4 Summary

This chapter has done a detailed literature survey of DC/DC converters for fuel cell based power supply. Possible candidates of the DC/DC converter topologies are discussed and compared. Half-bridge, push-pull converters are not suitable for high power systems, while simple boost and two phase boost converters are hardly capable of producing high voltage ratio. Although cascaded boost with two converter stages may have higher boost ratio and lower components stress, it adds the cost and converter size. Compared to voltage-fed converters [32] [48] [54], current-fed converters [31] [52] [74] have isolated high boost ratio and direct control of fuel cell current, which seems to be a good choice. Among all the current-fed converters, the current-fed full bridge converters have shown promising advantages for medium to high power fuel cell systems. The bulky magnetic components and the additional start-up circuit limit the further application of this kind of converter. A complete circuit analysis and closed loop control for a current-fed full bridge converter are presented in Chapter 6. Based on this analysis, an interleaved current-fed full bridge converter is proposed in Chapter 7. Not only high efficiency and small input current ripple can be achieved, but also the converter can obtain small input inductors and

soft start-up without adding any additional circuit except a small current rating switch.

Chapter 6

Isolated Current-fed Full Bridge Converter

In Chapter 5, three criteria are summarized when choosing DC/DC converter topologies for a fuel cell energy system: large boost ratio, low input current ripple and isolation. Due to the requirement of direct control of input current and high boost ratio, a current-fed DC/DC converter seems to be a competitive choice. Of all current-fed DC/DC topologies, an isolated current-fed full bridge converter (CFFB) exhibits good control of input current and inherent high boost ratio for high power systems. The aim of this chapter is to present the design and control strategy of an improved CFFB converter with a voltage doubler on the output side.

6.1 Operating States of the Isolated Current-fed Full Bridge Converter

Topology of the proposed current-fed full bridge converter is shown in Fig. 6.1. Compared to the conventional current-fed full bridge converter [55], the proposed

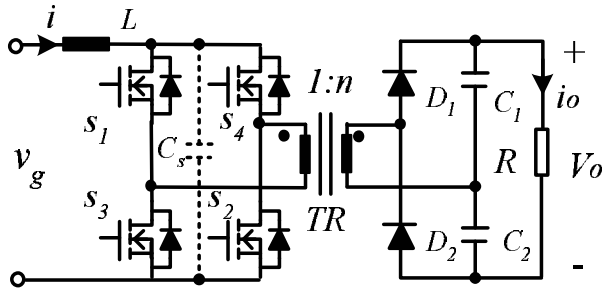

Figure 6.1: Topology of the proposed current-fed full bridge converter

CFFB converter has a voltage doubler on the output side. As seen in Fig. 6.1, instead of using a full bridge rectifier with four power diodes on the secondary side of the transformer, a voltage doubler with two diodes and two capacitors is used. Since fewer power diodes are used, power loss due to the conduction of power diodes is reduced. Moreover, output voltage V_o is now shared by two capacitors C_1 and C_2, lower voltage rating of capacitors can be used. Characteristic waveforms of the converter are shown in Fig. 6.2. During one switching cycle T_s, each switch conducts for DT_s period, where D is duty ratio. One operating cycle of the CFFB converter can be divided into four stages and equivalent circuits of the CFFB converter for each operating state are shown in Fig. 6.3. Circuit parameters are listed in Table.

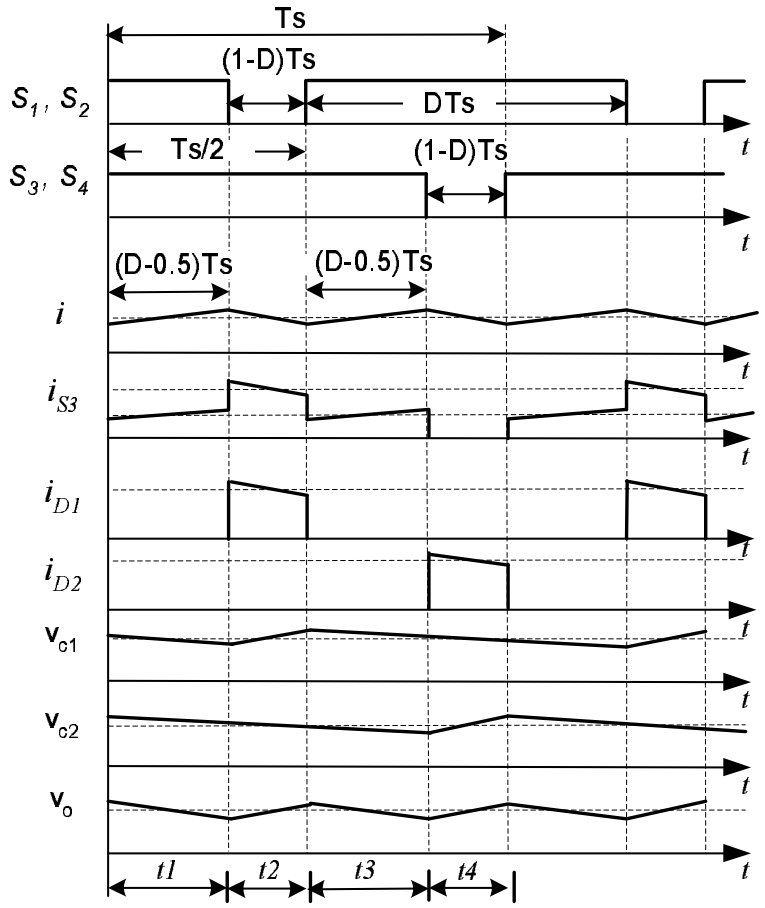

Figure 6.2: Gate signals and main waveforms

6.1. "C_s" denotes snubber capacitor. It absorbs over voltage caused by the current interruption in the leakage inductance of the transformer. They do not influence the main switching states of the circuit.

1. **Stage 1**, **3** (t1 = t3 = $(D - 0.5)T_s$): As shown in Fig. 6.3 (a), all switches ($S_1 \sim S_4$) turn on, inductor L is charged up. While on the secondary side of the transformer, load current flows through C_1 and C_2, all capacitors are discharged

Table 6.1: CFFB Converter Parameter Definition

v_g	Input voltage	v_o	Output voltage
v_{c1}/v_{c2}	Capacitor voltage	i	Inductor current
n	Transformer turns ratio	C_s	Snubber capacitor
r_L	Parasitic resistance of L	D	Duty ratio
r_{c1}/r_{c2}	Parasitic resistance of C	D'	$1-D$

by load current i_o. Dynamic equations during this stage are:

$$\begin{cases} L\dfrac{di}{dt} + r_L i = v_g, \\ C_1\dfrac{dv_{c1}}{dt} = C_2\dfrac{dv_{c2}}{dt} = \dfrac{-v_o}{R}. \end{cases} \tag{6.1}$$

2. **Stage 2** (t2 $= (1-D)T_s$): Switches S_1 and S_2 turn off (Fig. 6.3 (b)), inductor L is discharged as the energy is transferred to the secondary side through transformer TR. Hence D_1 conducts and C_1 is charged up while C_2 is discharged by load current i_o, as shown in Fig. 6.2. Dynamic equations during this stage are:

$$\begin{cases} L\dfrac{di}{dt} + r_L i = v_g - \dfrac{1}{n}(v_{c1} + r_{c1}C\dfrac{dv_{c1}}{dt}), \\ C_1\dfrac{dv_{c1}}{dt} = \dfrac{i}{n} - \dfrac{v_o}{R}, \\ C_2\dfrac{dv_{c2}}{dt} = -\dfrac{v_o}{R}. \end{cases} \tag{6.2}$$

3. **Stage 4** ($t4 = (1-D)T_s$): Switches S_3 and S_4 turn off (Fig. 6.3 (c)), inductor L is discharged and the energy is transferred to the secondary side through transformer TR. C_2 is charged up by means of D_2, while C_1 is discharged by

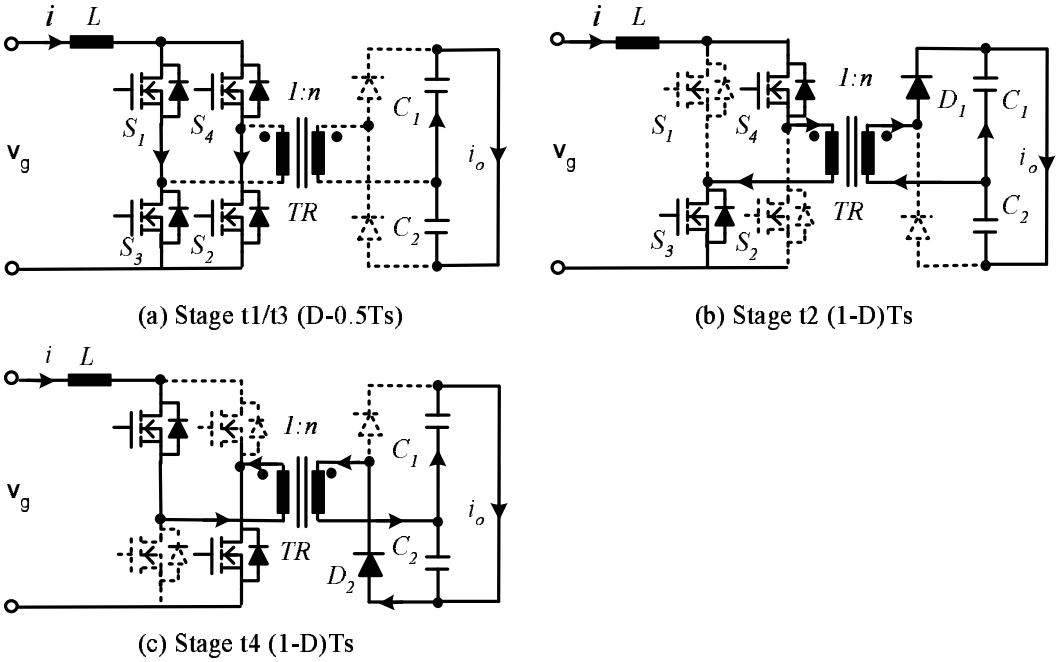

Figure 6.3: Equivalent circuits of CFFB converter for each operating state

load current i_o . Dynamic equations during this stage are:

$$\begin{cases} L\frac{di}{dt} + r_L i = v_g - \frac{1}{n}(v_{c2} + r_{c2}C\frac{dv_{c2}}{dt}), \\ C_1\frac{dv_{c1}}{dt} = -\frac{v_o}{R}, \\ C_2\frac{dv_{c2}}{dt} = \frac{i}{n} - \frac{v_o}{R}. \end{cases} \tag{6.3}$$

From Fig. 6.2, it is noticed that ripple frequency of the input current and output voltage are twice of the switching frequency. This helps reduce the input current and output voltage ripple without increasing switching frequency. In the next section, a small signal model of the proposed circuit is developed before the design of a closed loop controller.

6.2 Derivation of Small Signal Transfer Function

In order to simplify the calculation, it is reasonable to assume that $C_1 = C_2 = C$ and $r_{c1} = r_{c2} = 0$. Because the parasitic resistance of the electrolyte capacitor used in the converter design ($330\mu F/450V$) is about $180m\Omega$, which is only about 0.07% of the rated load resistance (266.7Ω). Hence the parasitic resistance of the capacitor can be neglected. By applying volt-seconds balance to the input inductor and charge balance to the output capacitors, the averaged equations during one T_s can be obtained:

$$\begin{cases} L\frac{d\langle i(t)\rangle_{T_s}}{dt} = (v_g(t) - r_L i(t)) - \frac{v_o(t)}{n}D' \\ C\frac{d\langle v_{c1}(t)\rangle_{T_s}}{dt} = \frac{i(t)}{n}D' - \frac{v_o(t)}{R} \\ C\frac{d\langle v_{c2}(t)\rangle_{T_s}}{dt} = \frac{i(t)}{n}D' - \frac{v_o(t)}{R} \end{cases} \tag{6.4}$$

Voltage transfer ratio of the proposed CFFB converter at steady state can be obtained from Eq. 6.4:

$$\frac{V_o}{V_g} = \frac{\frac{D'}{n}}{\frac{r_L}{R} + (\frac{D'}{n})^2}. \tag{6.5}$$

When under ideal conditions where parasitic resistance of the input inductor is neglected, Eq. 6.5 can be simplified as:

$$\frac{V_o}{V_g} = \frac{n}{D'}. \tag{6.6}$$

Compared to voltage ratio ($\frac{n}{2D'}$) in a conventional current-fed full bridge converter, voltage ratio of the proposed converter is twice of that in a conventional current-fed full bridge converter, as shown in Eq. 6.6. This is mainly due to the voltage-doubler

circuit on the secondary side.

Linearizing Eq. 6.4 at steady-state, and applying Lapalace transformation, control to output small signal transfer functions of the CFFB converter can be obtained as:

$$\begin{cases} \dfrac{\hat{i}(s)}{\hat{d}(s)} = \dfrac{\dfrac{CV_o}{n}s + \dfrac{4V_o}{nR}}{LCs^2 + (\dfrac{2L}{R} + r_L C)s + \dfrac{2r_L}{R} + 2(\dfrac{D'}{n})^2} \\ \dfrac{\hat{v_o}(s)}{\hat{i}(s)} = \dfrac{\dfrac{-2LV_o}{RD'}s + 2V_o(\dfrac{D'}{n^2} - \dfrac{r_L}{RD'})}{\dfrac{CV_o}{n}s + \dfrac{4V_o}{nR}} \end{cases} \tag{6.7}$$

Since direct current control is necessary, a closed loop current controller for the CFFB converter is designed in the next section.

6.3 Controller design

Maximum power rating of the CFFB converter is designed as $1.2kW$ according to the maximum power supplied by the Ballard fuel cell stack. Operating continuously at full power degrades the fuel cell stack performance at a rate of about 0.54 mV/hour. But the stack exhibits essentially zero degradation when it operates continuously under part load conditions ($< 35A$) [33]. Hence rated power of the converter is chosen as $600W$. The output voltage of CFFB converter is controlled at $V_o = 400V$, where output voltage of the fuel cell stack is around $33V$. Circuit specifications are listed in Table. 6.2.

Based on the circuit specifications, small signal transfer functions of the designed

Table 6.2: Converter specification

Switching frequency	$f_s = 10kHz$
Max power/voltage	$1200W/400V$
Switches	IXFK90N20 MOSFETs, $R_{DS(ON)} = 40m\Omega(100^oC)$
Diodes	2×Ultra fast MUR860 $8A/600V$
Output capacitors	$330\mu F$, $400V$ Electrolytic + $0.027\mu F$ polyester
Snubber capacitors	$0.44\mu F$ polyester
Input inductors	$PM114/93$, Ferrite Pot-core $N27$, L: $276\mu H$, $r_L = 51.2m\Omega$
Transformers	$PM114/93$, Ferrite Pot-core $N27$, $n_1/n_2 = 1:4$ $L_m = 784\mu H$, leakage inductance $L_k = 0.92\mu H$

CFFB converter can be obtained by substituting all above parameters into Eq. 6.7:

$$\begin{cases} G_{vid}(s) = \dfrac{\hat{i}(s)}{\hat{d}(s)} = \dfrac{3.623 \times 10^5 (s + 45.45)}{s^2 + 208.2s + 1.537 \times 10^5} \\ \\ G_{vi}(s) = \dfrac{\hat{v}_o(s)}{\hat{i}(s)} = \dfrac{-0.076032(s - 6391)}{(s + 45.45)} \end{cases} \tag{6.8}$$

For purpose of regulating both input current and output voltage of the CFFB converter, average current mode control is used due to the following two reasons:

- Current mode control can achieve a fast transient response during the load command.
- It is easy to limit the input current below the maximum allowable current value, which is important for the fuel cell.

Control scheme of the proposed converter is shown in Fig. 8.1. In this cascaded controller, the error between actual output voltage and reference is compensated. Output of this compensation is the input current reference and is sent to the inner current loop. Overall closed loop function is obtained as:

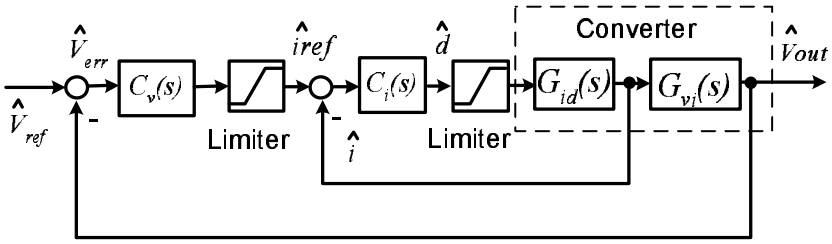

Figure 6.4: Schematic diagram of the cascaded controller

$$\begin{cases} \dfrac{\hat{d}(s)}{\hat{i}_{ref}(s)} = \dfrac{C_i(s)}{1 + C_i(s)G_{id}(s)} \\ \dfrac{\hat{V}_o(s)}{\hat{V}_{ref}(s)} = \dfrac{C_v(s)T_i(s)G_{vi}(s)}{1 + C_v(s)T_i(s)G_{vi}(s)} \end{cases} \tag{6.9}$$

Where

$$T_i(s) = \frac{C_i(s)G_{id}(s)}{1 + C_i(s)G_{id}(s)} \tag{6.10}$$

In order to ensure that averaging techniques is valid, one tenth of the switching frequency is chosen as the crossover frequency ω_c of the open current loop transfer function, which is around $1kHz$. Meanwhile a phase margin φ of 60^o is selected (Fig. 6.5). Similarly, one tenth of the inner current loop crossover frequency (100Hz) is chosen as the outer voltage loop crossover frequency, as shown in Fig. 6.6. Therefore, compensators $C_i(s)$ and $C_v(s)$ are obtained as:

$$C_i(s) = \frac{0.01473s + 56.72}{s} \tag{6.11}$$

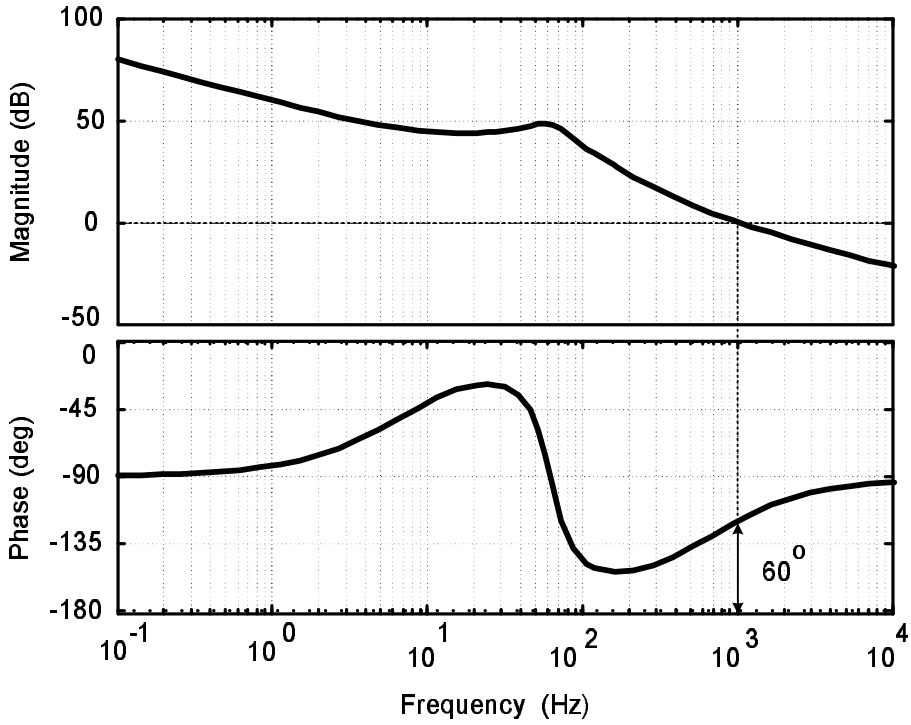

Figure 6.5: Bode plot of $C_i(s) * G_{id}$(s)

$$C_v(s) = \frac{1.125s + 377.8}{s} \tag{6.12}$$

It must be pointed out that although the controller is designed with constant input voltage V_g, it also works with large operating range of V_g. But the voltage undershoot and the settling time with the large range of V_g is slightly larger. This is verified from Matlab simulation in Fig. 6.7. Curves with dashed line gives the dynamic performance of the converter with constant V_g. While curves with solid line shows the dynamic response when V_g is represented as the nonlinear fuel cell polarization curve described in Chapter 3. The input voltage of the CFFB converter

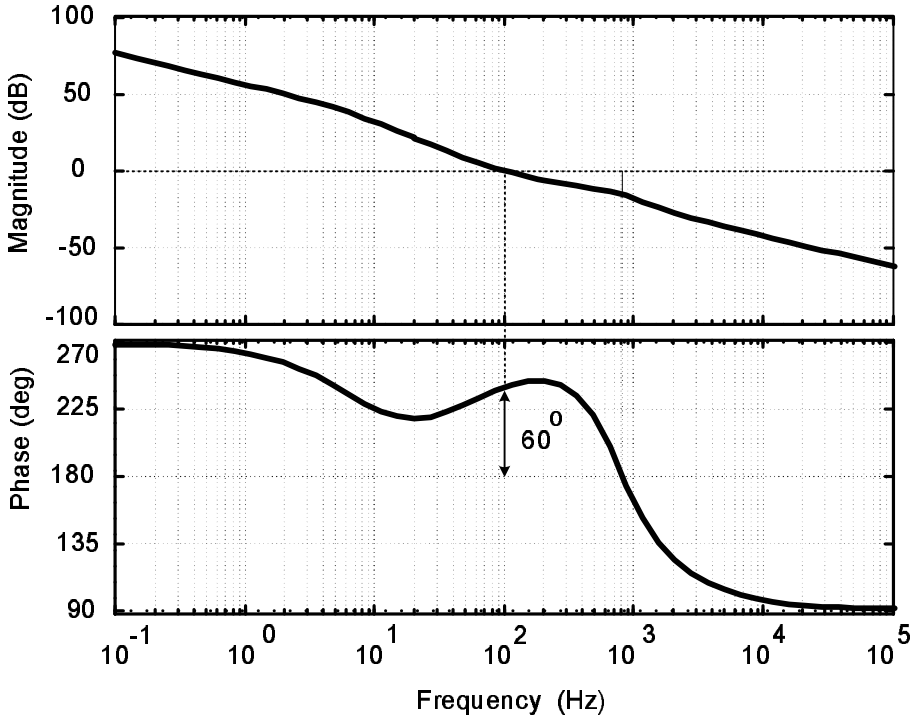

Figure 6.6: Bode plot of $C_v(s) * T_i(s) * G_{vi}(s)$

V_g is simulated as the following relationship from input current i:

$$V_g = 42 - 0.098i - 2.61 \log i - 0.009 \exp(0.01i) \tag{6.13}$$

Circuit simulation is performed via SIMPLORER $V6.0$ software tools [87] using parameters defined in Table 6.2. Fig. 6.8 shows the simulated waveforms when operating at power $1200W$. Compared to the analytical waveforms in Fig. 6.2, these waveforms verify the validity of the circuit analysis performed in section 6.1. Moreover, a voltage spike about $100V$ is noticed across the transformer primary side in Fig. 6.8. It is because whenever the circuit changes from stage **1** to stage **2** or from

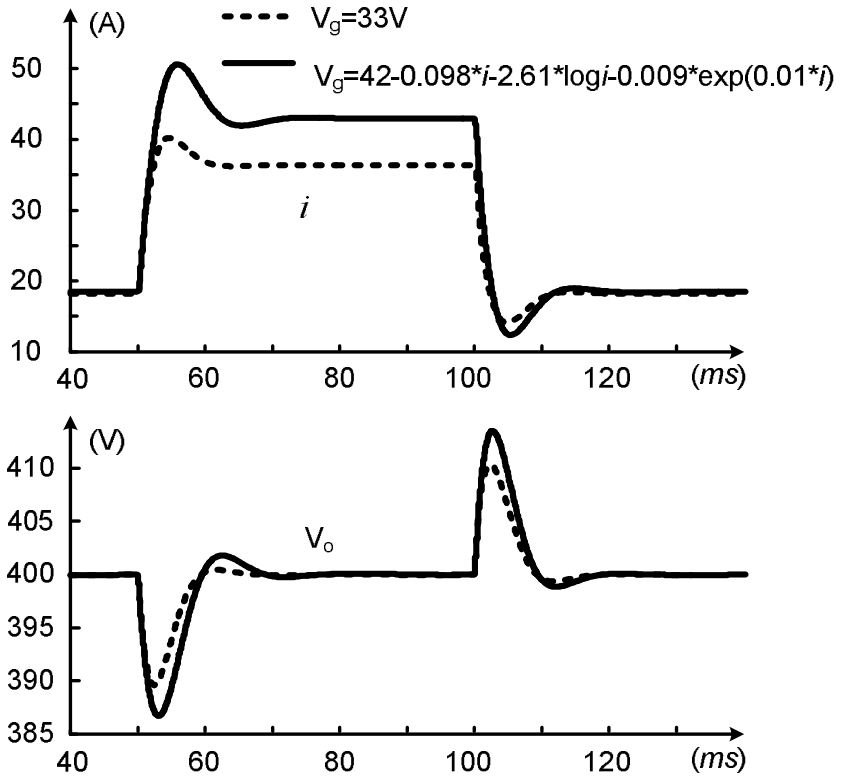

Figure 6.7: Simulation of output voltage V_o and input current i with different input voltage model V_g for load steps up from $600W$ to $1200W$ and steps down from $1200W$ to $600W$

stage **3** to stage **4**, current through the transformer leakage inductor changes from zero to input inductor current I_L. This causes a large di/dt in the leakage inductor of the transformer, which produces voltage spikes across the transformer primary. Hence, snubber capacitor C_s is connected across the bridge in the experiment to snub down the voltage spikes. Fig. 6.9 shows the simulated dynamic response of input current i and output voltage V_o to a load step up from $600W$ to $1200W$ and a step down from $1200W$ to $600W$. It is found that the output voltage can be regulated back to $400V$ in about $20ms$.

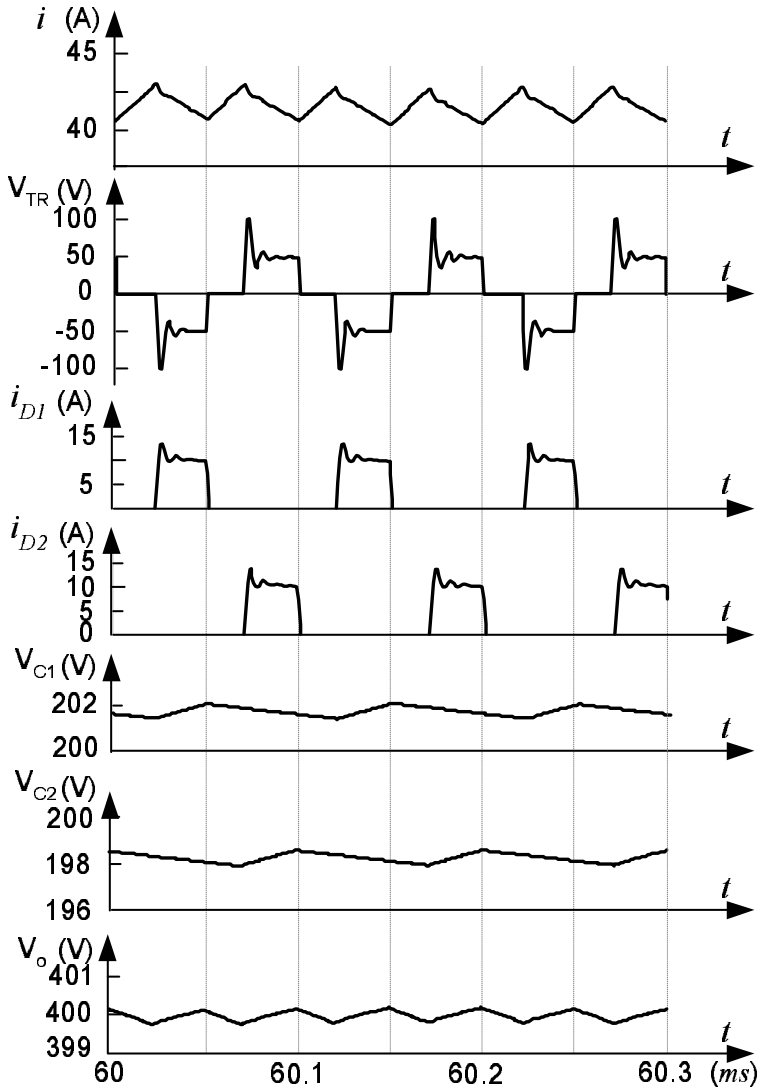

Figure 6.8: Main waveforms of CFFB converter (simulation): input current i, transformer primary voltage V_{TR}, diode current i_{D1} and i_{D2}, output capacitor voltage V_{C1} and V_{C2}, and total output voltage V_o

6.4 Controller implementation

Texas Instrument (TI) TMS320F243 DSP microcontroller is used to implement PWM functions and closed loop control. The DSP system has six PWM signals, eight channels of analog input and one 10-bit analog-to-digital converter (ADC).

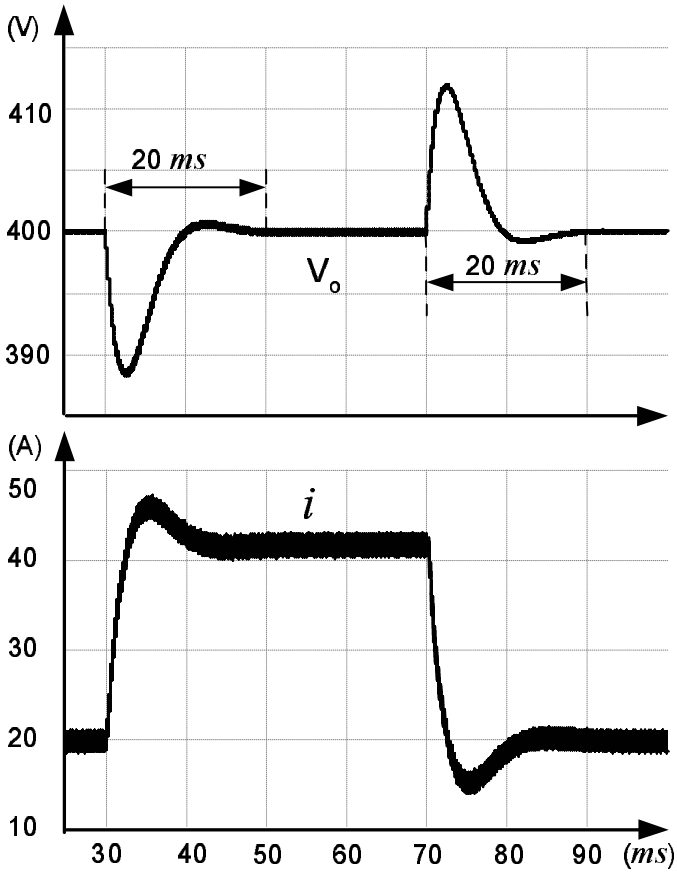

Figure 6.9: Waveforms of output voltage V_o and input current i when load steps up from $600W$ to $1200W$ and steps down from $1200W$ to $600W$ (simulation)

Minimum ADC conversion time for a simultaneous dual-conversion is about $850ns$ for each signal. Due to the inherent delay from A/D conversion, switching frequency of a DSP controlled system cannot go beyond tens of kilo Hertz. Hence $10kHz$ is selected as the converter switching frequency. Interrupt mask registers IMR and EVIMRA are configured to allow Timer1 to generate interrupt on period match. Fig. 6.10 shows the interfaced block diagram of controller implementation in DSP. The sensed voltage and current signals are fed to DSP by two ADC channels ADCIN1 and ADCIN2 respectively. The digitized feedback output voltage, V_o, is compared

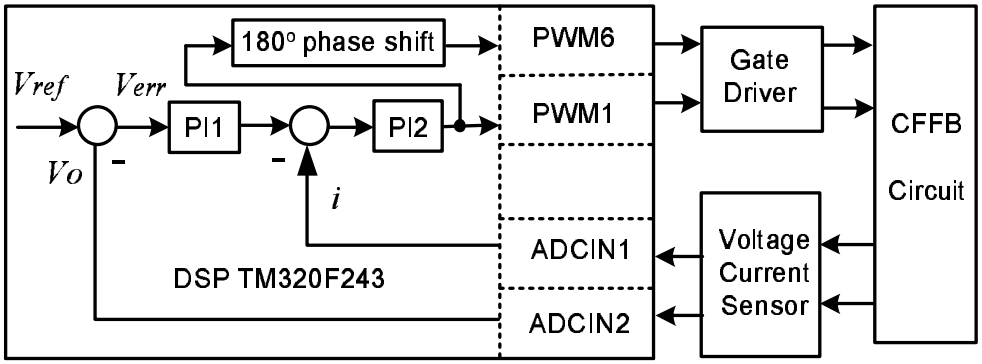

Figure 6.10: Interfaced block diagram of controller implementation in DSP

to an internally defined V_{ref}. The difference between these two voltages, V_{err}, is fed to voltage compensator PI1. The output of this compensator is the reference current command for the inner current loop. After comparing with the digitized inductor current feedback i, the difference is sent to the current compensator PI2. Output of this current compensator is fed to PWM module and written on the full compare register CMPR1. This CMPR1 is compared with a $10kHz$ triangle waveform generated internally by Timer1. PWM1 is generated to control switches S_1 and S_2. While PWM6 is used to control S_3 and S_4, which is 180^o phase shifted to PWM1 due to the proper configuration of the compare action control register ACTR. Flow chart for the main program and interrupt service routine are shown in Fig. 6.16 and Fig. 6.17 respectively (please refer to the rear part of this chapter).

6.4.1 Circuit Implementation

Schematic diagram of the driver circuit is shown in Fig. 6.11. As seen from the

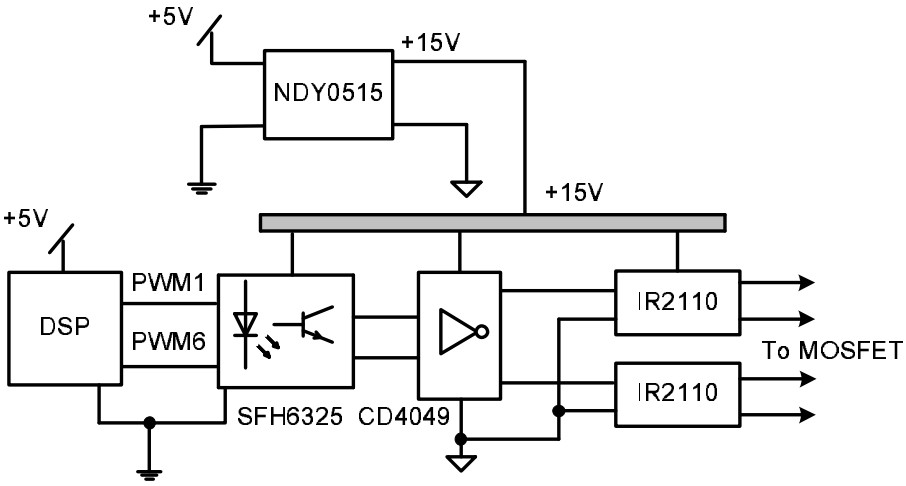

Figure 6.11: Schematic diagram of the driver circuit

figure, two IR2110s were used as MOSFET gate drivers, which were powered by an isolated $+15V$ supply. The isolated $+15V$ supply was provided by an isolated DC/DC converter NDY0515 to isolate the digital ground and analogue ground. High-speed dual optocoupler SFH6325 from Infineon Technologies and CD4049 from FAIRCHILD were used to isolate the grounds and match the electrical level between DSP and the MOSFET driver.

The feedback signals of output voltage and input current were obtained through current and voltage transducer LEM LA55P and LEM LV25-P. Since both output voltage and input current are positive, the LEM output signals were translated into voltage signals in range of $0 \sim 5V$. After ADC conditioning, the $0 \sim 5V$ signal was converted into a ten-bits digital value. The complete current and voltage sensing and scaling is described in Fig. 6.12.

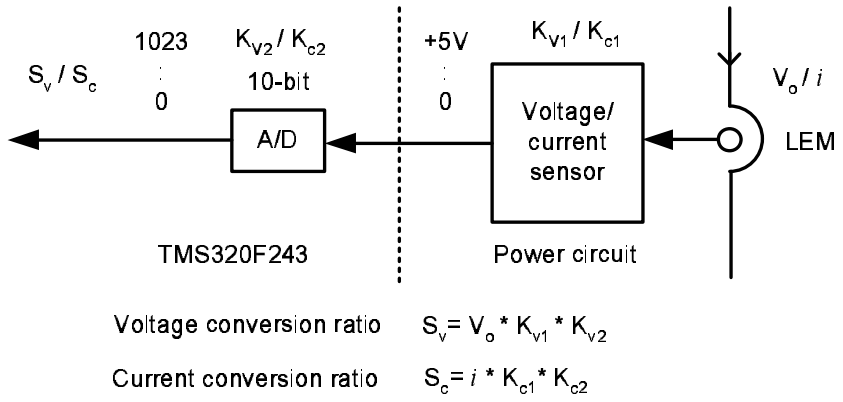

Figure 6.12: Block diagram of current and voltage sensing and scaling

6.5 Experimental Results

Fig. 6.13 shows the steady-state waveforms of the proposed converter operating at output power $1140W$. Inductor current ripple is about 8.3% of the rated average current and output voltage is almost ripple-free. Fig. 6.14 shows the measured converter efficiency at different output power from $0W$ to $1200W$. Efficiency at $1.2kW$ is about 89%.

Fig. 6.15 shows the dynamic response of the proposed converter during the load insertion and rejection. Output voltage can be regulated back to $400V$ in about $35ms$, when required output power changes from $680W$ to $1160W$.

6.6 Summary

To meet the criteria of selecting front-end DC/DC converters for a fuel cell system, an isolated current-fed full bridge converter (CFFB) is proposed in this chapter with

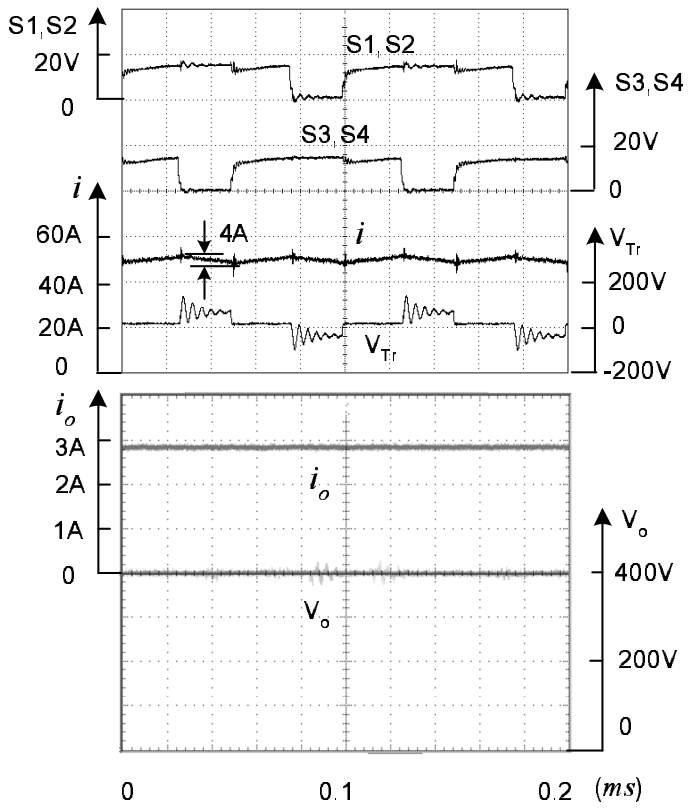

Figure 6.13: Steady-state waveforms of CFFB converter (experiment at $P_{out} = 1140W$, $V_g = 26V$) (a) Gate signals S_1, S_2 and S_3, S_4, input current i and transformer primary voltage V_{TR}; (b) output current i_o and output voltage V_o

a voltage doubler on the secondary side, which has a voltage conversion ratio twice of that in a conventional current-fed full bridge converter. Due to its high voltage conversion ratio and ability to dynamically control the input current, it is considered as a suitable DC/DC converter to boost the low output voltage of the fuel cell stack. Detailed circuit analysis is performed and a closed loop controller for the proposed converter is designed in detail. These analysis could be complementary for the existing current-fed full bridge converters, and it provides a good basis for the interleaved current-fed full bridge converter proposed in the next chapter. Another advantage of

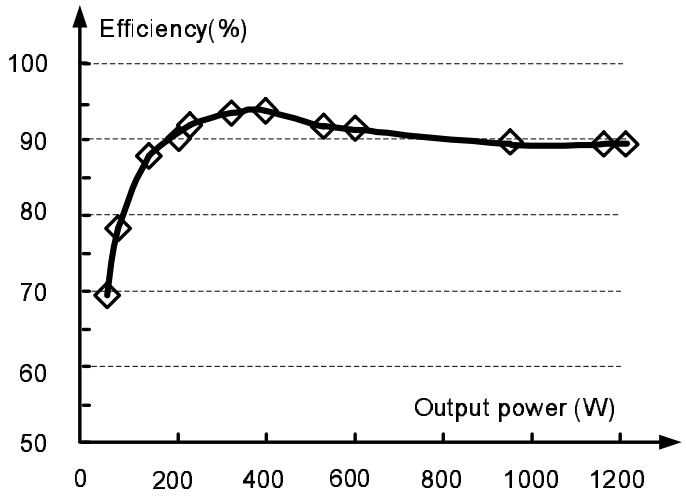

Figure 6.14: Measured converter efficiency vs. output power (experiment) ($V_o = 400V, D = 0.67$)

using this transformer coupled CFFB is its modularity. It could have many CFFB modules connected in parallel and series. By doing so, not only the power can be shared by several modules, but the input current ripple can be further reduced. Moreover, it becomes easy and convenient to connect this transformer coupled CFFB with multilevel inverters.

To verify the circuit analysis, a $1.2kW$ power converter is set up and the proposed current controller is implemented on a digital signal processor DSP TMS320F. Less than 10% input current ripple and 89% efficiency have been achieved at the full power rating. Regulation of the output voltage can be realized within 34 ms during the load step. These results show that the proposed converter is a good candidate for a front-end DC/DC converter in a fuel cell system.

However, inherent problems of the CFFB converter still exist: high current input inductor and large inrush current during start-up. In order to solve these problems,

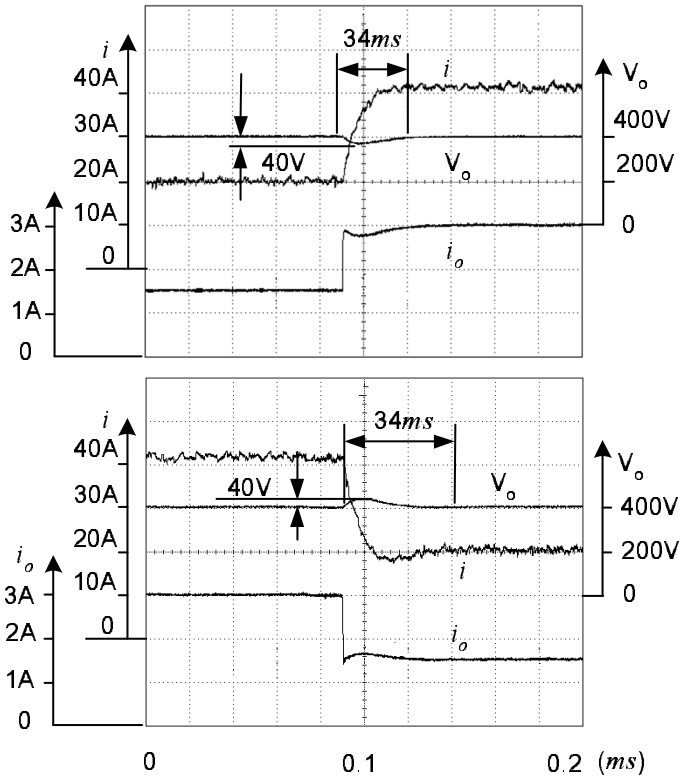

htb

Figure 6.15: output voltage V_o, output current i_o and input current i (experiment) (a) Load steps from $680W$ to $1160W$; (b) Load steps from $1160W$ to $680W$

a new ICFFB converter will be proposed in the next chapter.

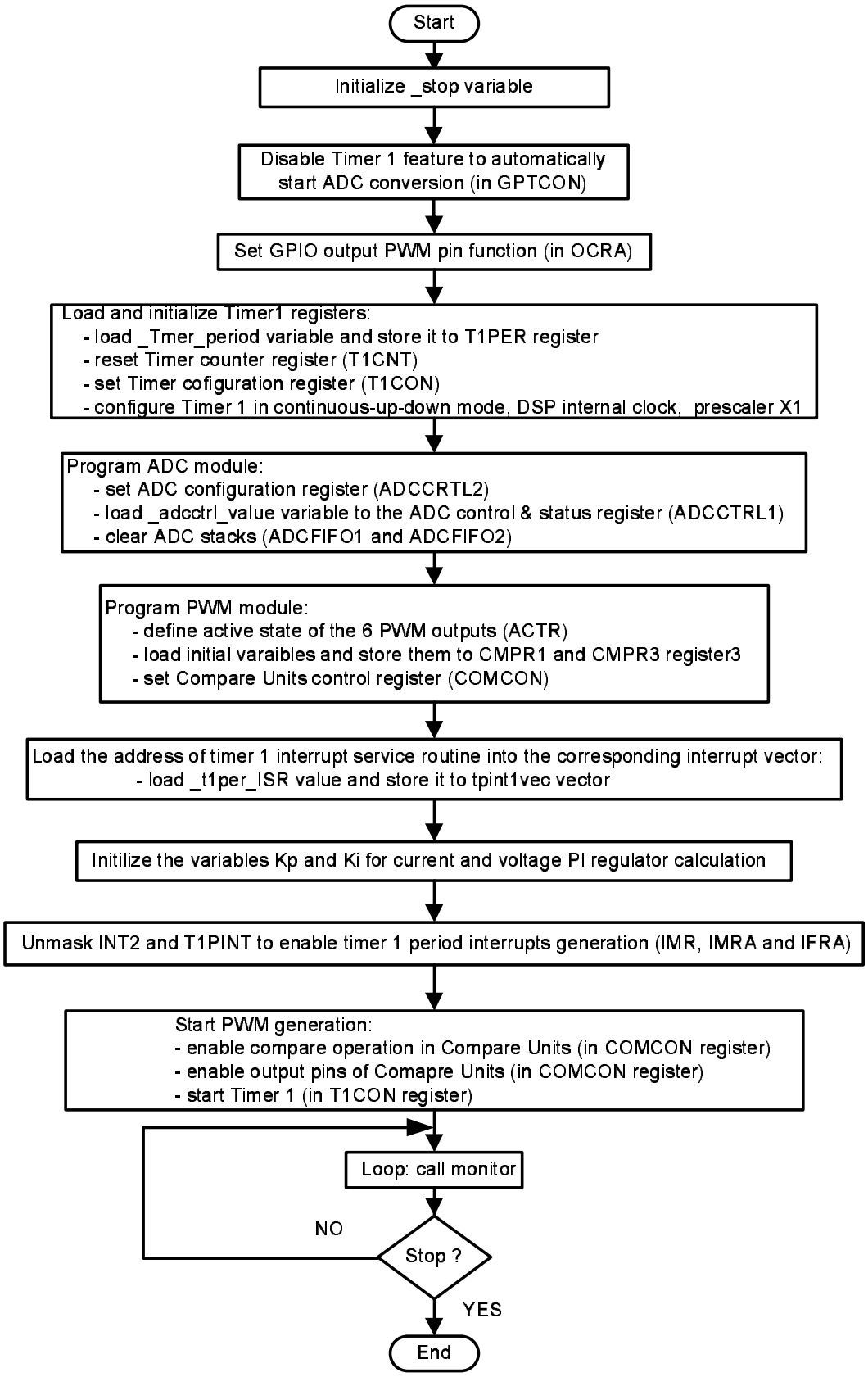

Figure 6.16: Flow chart for the main program

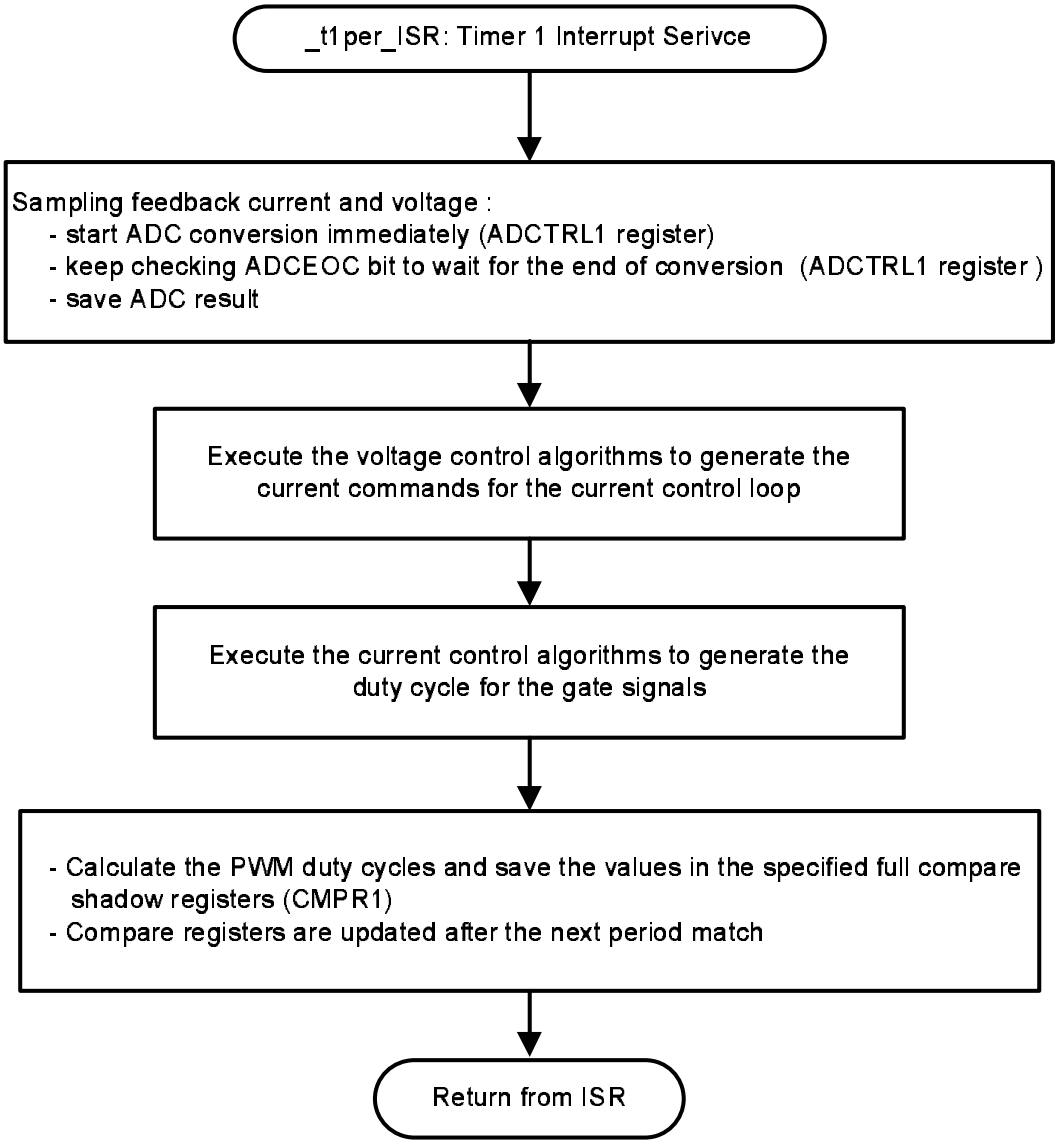

Figure 6.17: Flow chart for interrupt service routine

Chapter 7

An Interleaved Current-fed Full Bridge Converter

In Chapter 6, an improved current-fed full bridge converter is proposed with a voltage doubler on the output side. Compared to conventional current-fed full bridge converters, the CFFB converter has a higher boost ratio. However, as presented in Chapter 5, common problems still exist in this CFFB converter.

- Size and weight of a high current inductor become problematic for a high power system.
- Large inrush current during start-up.

In order to reduce the size of the magnetic components and further improve the converter efficiency, an interleaved current-fed full bridge converter (ICFFB) is pro-

posed with a parallel input and a series output scheme. By parallelling input of the converter system, input current and hence the power can be equally shared between the modules of the converter system. Therefore current stress on the semiconductor devices on the input side is reduced. On the other hand, the series connection on the output side results in lower voltage ratings for output capacitors and diodes. Furthermore, phase shifted PWM is used for the interleaved converter. In so doing, the input current ripple frequency and the output voltage ripple frequency becomes four times of the switching frequency. Hence for the same input current and output voltage ripple requirement, smaller input inductors and output capacitors can be used. Moreover, large inrush current during start-up is eliminated via a soft start-up scheme without additional complex start-up circuit for this ICFFB converter.

7.1 Operating States of the Interleaved Current-Fed Full Bridge Converter

Fig. 7.1 shows the schematic diagram of the interleaved current-fed full bridge converter. Two CFFB converters are connected with parallel inputs and serial outputs. Characteristic waveforms of the circuit are shown in Fig. 7.2.

During one switching cycle T_s, each switch conducts for DT_s period, where D is duty ratio. For the first module (upper one in Fig. 7.1), three switching states are possible: S_1, S_2 off and S_3, S_4 on (t4 state in Fig. 7.2), S_3, S_4 off and S_1, S_2 on (t8

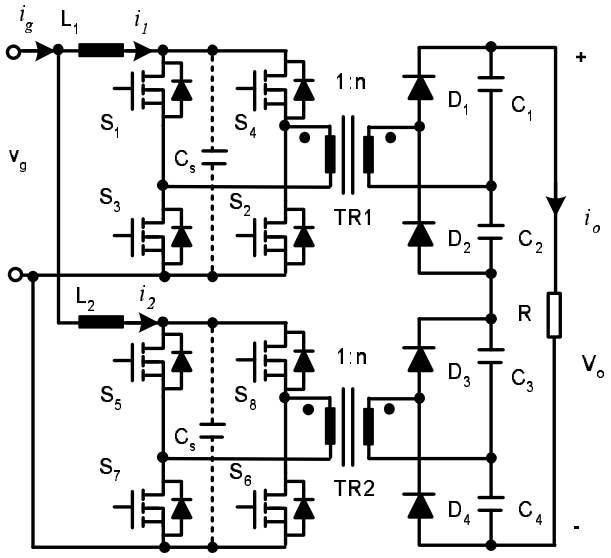

Figure 7.1: Schematic diagram of ICFFB converter

state in Fig. 7.2) and $S_1 \sim S_4$ all on (other states in Fig. 7.2). State t8 follows t4 by a phase shift of 180^o.

Similarly, the second module (lower one in Fig. 7.1) has three switching states. It also uses the switching state sequence like the first converter. In order to interleave the two converters, the switching scheme of the second converter is shifted by 90^o to follow the first one. Hence 90^o phase shift can be achieved among all the four switching gate signals, as shown in Fig. 7.2.

From Fig. 7.2, it is seen that one switching period T_s can be divided into eight states (t1 $\sim$ t8). In order to obtain the same output voltage when input voltage changes, D may go from < 0.75 to > 0.75. The ripple waveform for $D > 0.75$ (Fig. 7.2 (a)) is different from that in case of $D < 0.75$ (Fig. 7.2 (b)). Hence equivalent circuits of ICFFB converter for each operating state are shown in Fig. 7.3 and Fig.

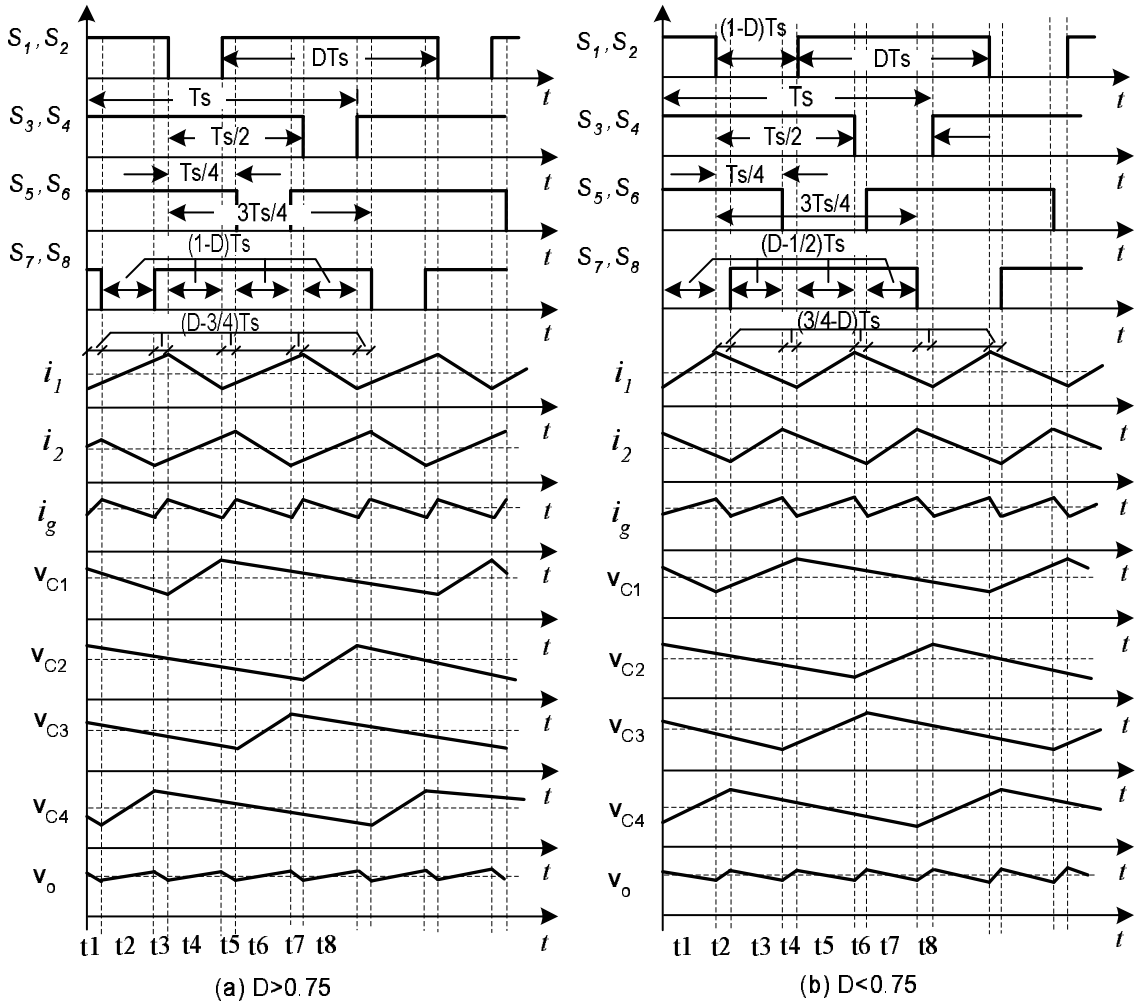

Figure 7.2: Gate signals and main waveforms

7.4 for $D > 0.75$ and $D < 0.75$ respectively.

Parameters for the circuit are listed in Table 7.1. "C_s" denotes snubber capacitors. They absorb the over voltage caused by the current interruption in the leakage inductance of the transformer. They do not influence the main switching states of the circuit.

Operating stages of ICFFB converter when $D > 0.75$ (Fig. 7.3) are:

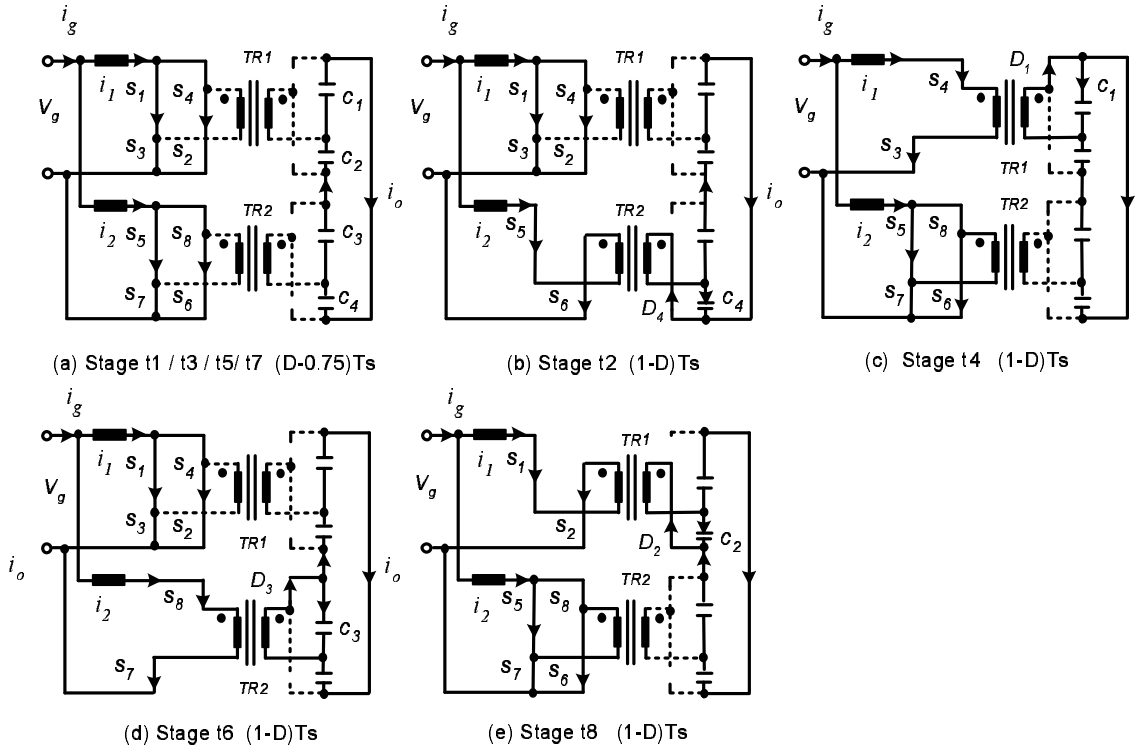

Figure 7.3: Equivalent circuits of ICFFB converter for each operating state when $D > 0.75$

Table 7.1: Converter parameter definition

i_1/i_2	Inductor current	i_g	Input current
$v_{c1} \sim v_{c4}$	Capacitor voltage	v_o	Output voltage
$r_1 \sim r_2$	Parasitic resistance of L	D	Duty ratio
C_s	Snubber capacitor	D'	$1 - D$

1. **States t1**, **t3**, **t5**, **t7** (t1 = t3 = t5 = t7 = $(D - 0.75)T_s$): As shown in Fig. 7.3 (a), all switches are on, both inductor currents increase. While on the secondary side of the transformer, all capacitors are discharged by the load

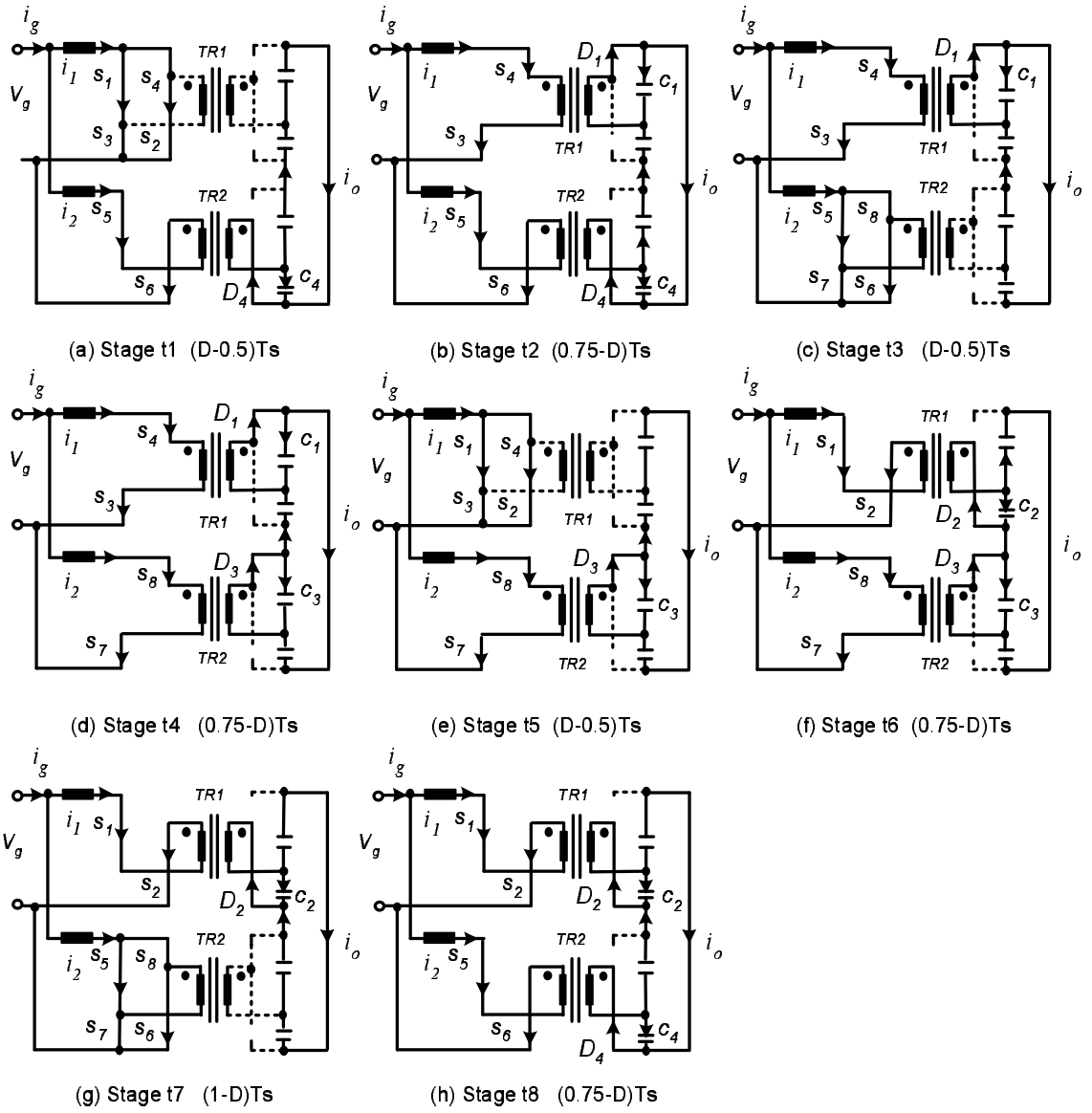

Figure 7.4: Equivalent circuits of ICFFB converter for each operating state when $D < 0.75$

current i_o. Dynamic equations during this stage are:

$$\begin{cases} L_1 \dfrac{di_1}{dt} + r_{L1} i_1 = v_g, \\ L_2 \dfrac{di_2}{dt} + r_{L1} i_2 = v_g, \\ C_1 \dfrac{dv_{c1}}{dt} = C_2 \dfrac{dv_{c2}}{dt} = C_3 \dfrac{dv_{c3}}{dt} = C_4 \dfrac{dv_{c4}}{dt} = \dfrac{-v_o}{R}. \end{cases} \tag{7.1}$$

2. **State t2** (t2 = $(1-D)T_s$): Switches S_7 and S_8 turn off (Fig. 7.3 (b)). Current in inductor L_1 keeps increasing. However inductor L_2 is discharged as the energy is transferred to the secondary side through transformer $TR2$. Hence C_4 is charged up by means of D_4, while all the other capacitors are discharged by the load current i_o, see waveforms in Fig. 7.2 (a). Dynamic equations during this stage are:

$$\begin{cases} L_1\dfrac{di_1}{dt} + r_1 i_1 = v_g, \\ L_2\dfrac{di_2}{dt} + r_2 i_2 = v_g - \dfrac{v_{c4}}{n}, \\ C_1\dfrac{dv_{c1}}{dt} = C_2\dfrac{dv_{c2}}{dt} = C_3\dfrac{dv_{c3}}{dt} = -\dfrac{v_o}{R}, \\ C_4\dfrac{dv_{c4}}{dt} = \dfrac{i_2}{n} - \dfrac{v_o}{R}. \end{cases} \tag{7.2}$$

3. **State t4** (t4 = $(1-D)T_s$): Switches S_1 and S_2 turn off (Fig. 7.3 (c)). Current in inductor L_2 keeps increasing. However inductor L_1 is discharged as the energy is transferred to the secondary side through transformer $TR1$. Hence D_1 conducts and C_1 is charged up while all the other capacitors are discharged by the load current i_o (Fig. 7.2 (a)). Dynamic equations during this stage are:

$$\begin{cases} L_1\dfrac{di_1}{dt} + r_1 i_1 = v_g - \dfrac{v_{c1}}{n}, \\ L_2\dfrac{di_2}{dt} + r_2 i_2 = v_g, \\ C_1\dfrac{dv_{c1}}{dt} = \dfrac{i_1}{n} - \dfrac{v_o}{R}, \\ C_2\dfrac{dv_{c2}}{dt} = C_3\dfrac{dv_{c3}}{dt} = C_4\dfrac{dv_{c4}}{dt} = -\dfrac{v_o}{R}. \end{cases} \tag{7.3}$$

4. **State t6** (t6 = $(1-D)T_s$): This state (Fig. 7.3 (d)) is very similar to **State t2** (Fig. 7.3 (b)). However here switches S_5 and S_6 are off, which reverses the

polarity at the secondary of $TR2$. Hence, D_3 conducts and C_3 is charged up. Dynamic equations during this stage are:

$$\begin{cases} L_1\dfrac{di_1}{dt} + r_1 i_1 = v_g, \\ L_2\dfrac{di_2}{dt} + r_2 i_2 = v_g - \dfrac{v_{c3}}{n}, \\ C_1\dfrac{dv_{c1}}{dt} = C_2\dfrac{dv_{c2}}{dt} = C_4\dfrac{dv_{c4}}{dt} = -\dfrac{v_o}{R}, \\ C_3\dfrac{dv_{c3}}{dt} = \dfrac{i_2}{n} - \dfrac{v_o}{R}. \end{cases} \tag{7.4}$$

5. **State t8** (t8 $= (1-D)T_s$): As shown in Fig. 7.3 (e), this state is quite similar to **State t4** (Fig. 7.3 (c)). Switches S_3 and S_4 are off, which reverses the polarity at the secondary winding of $TR1$. Hence, D_2 conducts and C_2 is charged up, see waveforms in Fig. 7.2 (a). Dynamic equations during this stage are:

$$\begin{cases} L_1\dfrac{di_1}{dt} + r_1 i_1 = v_g - \dfrac{v_{c2}}{n}, \\ L_2\dfrac{di_2}{dt} + r_2 i_2 = v_g, \\ C_2\dfrac{dv_{c2}}{dt} = \dfrac{i_1}{n} - \dfrac{v_o}{R}, \\ C_1\dfrac{dv_{c1}}{dt} = C_3\dfrac{dv_{c3}}{dt} = C_4\dfrac{dv_{c4}}{dt} = -\dfrac{v_o}{R}. \end{cases} \tag{7.5}$$

Similarly, when converters operate at $D < 0.75$ (Fig. 7.4), **State t1** in Fig. 7.3 (a) does not exist anymore but some new states are generated. Operating states **t1**, **t3**, **t5** and **t7** (Fig. 7.4 (a) (c) (e) (g)) are very similar to the states t2, t4, t6 and t8 in Fig. 7.3 (a) respectively. Time interval for each of the states in Fig. 7.4 (a) (c) (e) (g) is $(D-0.5)T_s$. The new operating states are:

1. **State t2** (t2 $= (0.75-D)T_s$): Switches S_7, S_8, S_1, S_2 turn off (Fig. 7.4 (b)), both inductors are discharged as the energy is transferred to the secondary side

through both transformers $TR1$ and $TR2$. C_4 and C_1 are charged up by means of D_4 and D_1, while the other capacitors are discharged by the load current i_o, see waveforms in Fig. 7.2 (b). Dynamic equations during this stage are:

$$\begin{cases} L_1\dfrac{di_1}{dt} + r_1 i_1 = v_g - \dfrac{v_{c1}}{n}, \\ L_2\dfrac{di_2}{dt} + r_2 i_2 = v_g - \dfrac{v_{c4}}{n}, \\ C_1\dfrac{dv_{c1}}{dt} = \dfrac{i_1}{n} - \dfrac{v_o}{R}, \\ C_4\dfrac{dv_{c4}}{dt} = \dfrac{i_2}{n} - \dfrac{v_o}{R}, \\ C_2\dfrac{dv_{c2}}{dt} = C_3\dfrac{dv_{c3}}{dt} = -\dfrac{v_o}{R}. \end{cases} \tag{7.6}$$

2. **State t4** (t4 $= (0.75 - D)T_s$): This state (Fig. 7.4 (d)) is very similar to **State t2** (Fig. 7.4 (b)) except that S_5, S_6 turn off instead of S_7, S_8. Polarity at the secondary of $TR2$ is reversed. Hence D_1 and D_3 conduct, C_1 and C_3 are charged up. Dynamic equations during this stage are:

$$\begin{cases} L_1\dfrac{di_1}{dt} + r_1 i_1 = v_g - \dfrac{v_{c1}}{n}, \\ L_2\dfrac{di_2}{dt} + r_2 i_2 = v_g - \dfrac{v_{c3}}{n}, \\ C_1\dfrac{dv_{c1}}{dt} = \dfrac{i_1}{n} - \dfrac{v_o}{R}, \\ C_3\dfrac{dv_{c3}}{dt} = \dfrac{i_2}{n} - \dfrac{v_o}{R}, \\ C_2\dfrac{dv_{c2}}{dt} = C_4\dfrac{dv_{c4}}{dt} = -\dfrac{v_o}{R}. \end{cases} \tag{7.7}$$

3. **State t6** (t6 $= (0.75 - D)T_s$): Switches S_3, S_4, S_5, S_6 turn off (Fig. 7.3 (f)), Polarity at secondary of $TR1$ is reversed. Energy is transferred to the secondary side through both transformers. C_2 and C_3 are charged up by means of D_2 and D_3, while the other capacitors are discharged by the load current i_o,

see waveforms in Fig. 7.2 (b). Dynamic equations during this stage are:

$$\begin{cases} L_1\dfrac{di_1}{dt} + r_1 i_1 = v_g - \dfrac{v_{c2}}{n}, \\ L_2\dfrac{di_2}{dt} + r_2 i_2 = v_g - \dfrac{v_{c3}}{n}, \\ C_2\dfrac{dv_{c2}}{dt} = \dfrac{i_1}{n} - \dfrac{v_o}{R}, \\ C_3\dfrac{dv_{c3}}{dt} = \dfrac{i_2}{n} - \dfrac{v_o}{R}, \\ C_1\dfrac{dv_{c1}}{dt} = C_4\dfrac{dv_{c4}}{dt} = -\dfrac{v_o}{R}. \end{cases} \tag{7.8}$$

4. **State t8** (t8 $= (0.75 - D)T_s$): This state (Fig. 7.4 (h)) is similar to **State t6** (Fig. 7.3 (f)) except that S_7, S_8 turn off instead of S_5, S_6. Hence D_2 and D_4 conducts, C_2 and C_4 are charged up. Dynamic equations during this stage are:

$$\begin{cases} L_1\dfrac{di_1}{dt} + r_1 i_1 = v_g - \dfrac{v_{c2}}{n}, \\ L_2\dfrac{di_2}{dt} + r_2 i_2 = v_g - \dfrac{v_{c4}}{n}, \\ C_2\dfrac{dv_{c2}}{dt} = \dfrac{i_1}{n} - \dfrac{v_o}{R}, \\ C_4\dfrac{dv_{c4}}{dt} = \dfrac{i_2}{n} - \dfrac{v_o}{R}, \\ C_1\dfrac{dv_{c1}}{dt} = C_3\dfrac{dv_{c3}}{dt} = -\dfrac{v_o}{R}. \end{cases} \tag{7.9}$$

It is clearly observed from Fig. 7.2 that ripple frequency of the input current and output voltage is four times the switching frequency.

Next, a closed loop voltage controller with current sharing between the input inductors is to be developed. To achieve this, the small signal model of the circuit has to be derived.

7.2 Small Signal Analysis

Applying circuit analysis and averaging state variable for Eq. 7.1 $\sim$ Eq. 7.9 over switching period T_s for $D < 0.75$ and $D > 0.75$ respectively, the same averaged equations during one switching cycle are obtained:

$$\begin{cases} L_1 \frac{d\langle i_1(t)\rangle_{T_s}}{dt} = (v_g(t) - r_1 i_1(t)) - \frac{v_o(t)}{2n} D', \\ L_2 \frac{d\langle i_2(t)\rangle_{T_s}}{dt} = (v_g(t) - r_2 i_2(t)) - \frac{v_o(t)}{2n} D', \\ C_1 \frac{d\langle v_{c1}(t)\rangle_{T_s}}{dt} = C_2 \frac{d\langle v_{c2}(t)\rangle_{T_s}}{dt} = \frac{i_1(t)}{n} D' - \frac{v_o(t)}{R}, \\ C_3 \frac{d\langle v_{c3}(t)\rangle_{T_s}}{dt} = C_4 \frac{d\langle v_{c4}(t)\rangle_{T_s}}{dt} = \frac{i_2(t)}{n} D' - \frac{v_o(t)}{R}. \end{cases} \tag{7.10}$$

In order to simplify the calculations, it is reasonable to assume that $C_1 \sim C_4 = C$. By applying volt-seconds balance to the input inductors and charge balance to the output capacitors, voltage transfer ratio of the proposed converter can be written as:

$$\frac{V_o}{V_g} = \frac{2 \times 2 \times (\frac{n}{2D'})}{1 + \frac{n^2(r_1 + r_2)}{RD'^2}}. \tag{7.11}$$

When under ideal condition where the parasitic resistance of inductors is neglected, voltage transfer ratio of this ICFFB converter is:

$$\frac{V_o}{V_g} = 2 \times 2 \times (\frac{n}{2D'}). \tag{7.12}$$

Compared to the voltage ratio $(\frac{n}{2D'})$ in a conventional current-fed full bridge converter, voltage ratio of the proposed converter is four times of that in a conventional current-fed full bridge converter, as shown in Eq. 7.12. This is mainly due to the voltage-doubler circuit on the secondary side and the series connection of output rectifiers. Therefore according to Eq. 7.12, four parameters can be used to step up the

input voltage: (i) converter duty ratio ($2D'$), (ii) transformer turns-ratio (n), (iii) voltage-doubler feature of output rectifiers ($\times 2$), (iv) series connection of output rectifiers ($\times 2$).

Linearizing Eq. 7.10 at steady-state, and applying Laplace transformation, the control to output small signal transfer functions are obtained:

$$\begin{aligned} G_{i1d}(s) &= \frac{\hat{i_1}}{\hat{d}} \\ &= \frac{n(r_2 + L_2 s)(8 + CRs)V_o}{2(D'^2 R * a + n^2(r_1 + L_1 s)(r_2 + L_2 s)(4 + CRs))}, \end{aligned} \tag{7.13}$$

$$\begin{aligned} G_{i2d}(s) &= \frac{\hat{i_2}}{\hat{d}} \\ &= \frac{n(r_1 + L_1 s)(8 + CRs)V_o}{2(D'^2 R * a + n^2(r_1 + L_1 s)(r_2 + L_2 s)(4 + CRs))}, \end{aligned} \tag{7.14}$$

$$\begin{aligned} G_{vig}(s) &= \frac{\hat{v_o}}{\hat{i_g}} \\ &= \frac{-8n(r_1 + L_1 s)(r_2 + L_2 s) + 2D'^2 R * a/n}{D'(8 + CRs) * a}. \end{aligned} \tag{7.15}$$

Where

$$\begin{cases} a = r_1 + r_2 + (L_1 + L_2)s, \\ \hat{i_g} = \hat{i_1} + \hat{i_2}. \end{cases} \tag{7.16}$$

$G_{i1d}(s)$ and $G_{i2d}(s)$ are small signal transfer functions from duty ratio to individual inductor current, while $G_{vig}(s)$ is the small signal transfer function from input current to output voltage.

7.3 Controller design

For direct control of the input current, current controller is necessary to regulate the source current at desired value. Moreover, in order to effectively reduce the input current ripple, equal current sharing between the two input inductors is necessary. On the other hand, output voltage should be well regulated during the load variations. Therefore a closed loop voltage controller with current sharing is designed for the proposed converter. Control schematic diagram is shown in Fig. 7.5. Instead of

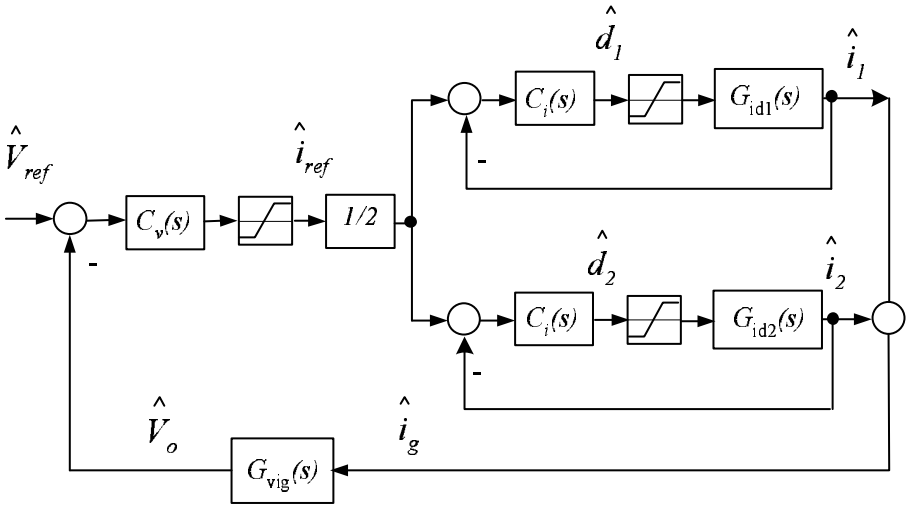

Figure 7.5: Control diagram for the interleaved current-fed full bridge converter

controlling the output voltage of each module, the total output voltage is sensed and compared with the reference voltage. The voltage controller generates the total input current reference. The reference current for each inductor is half of the total input current reference. Hence with the help of each inner current control loop, equal current sharing is realized between the two input inductors. Overall closed loop function is

obtained as:

$$\frac{\hat{V}_{out}}{\hat{V}_{ref}} = \frac{\frac{1}{2}T_i(s)C_v(s)C_{vig}(s)}{1+\frac{1}{2}T_i(s)C_v(s)C_{vig}(s)}, \tag{7.17}$$

where

$$T_i(s) = \frac{C_i(s)G_{i1d}(s)}{1+C_i(s)G_{i1d}(s)} + \frac{C_i(s)G_{i2d}(s)}{1+C_i(s)G_{i2d}(s)}. \tag{7.18}$$

The controllers are designed for the following circuit specifications: $V_g = 33V$, $P_o = 600W$, $f_s = 10kHz$, $D = 0.67$, $L_1 = L_2 = 178\mu H$, $r_1 = r_2 = 64m\Omega$, $C_1 \sim C_4 = 100\mu F$, $n = 2$. Bode plot of the control system is shown in Fig. 7.6 and Fig. 7.7. Crossover frequency ω_c of the open loop transfer function for current is one tenth

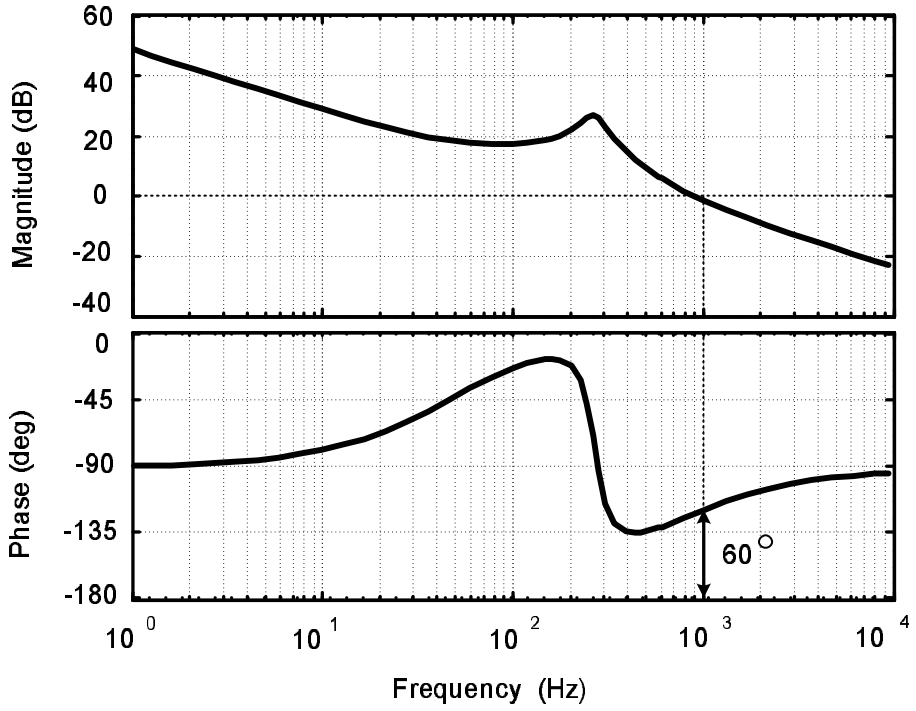

Figure 7.6: Bode plot of $C_i(s) * G_{i1d}$(s) Bode plot of $C_v(s) * T_i(s) * G_{vig}(s)$

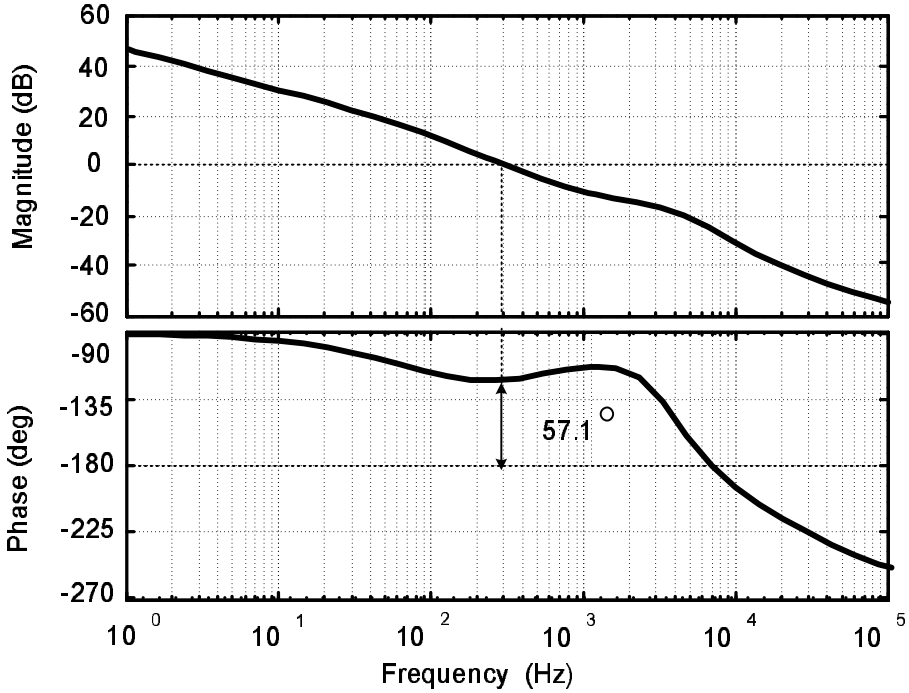

Figure 7.7: Bode plot of $C_v(s) * T_i(s) * G_{vig}(s)$

of the switching frequency and equal to $1kHz$. A phase margin of 60^o is selected (Fig. 7.6). Similarly, one tenth of the inner current loop crossover frequency (100Hz) is chosen as the outer voltage loop crossover frequency, see Fig. 7.7). Therefore, compensators $C_i(s)$ and $C_v(s)$ are obtained as:

$$C_i(s) = 0.0087 + \frac{34.67}{s}, \tag{7.19}$$

$$C_v(s) = 0.1269 + \frac{108.68}{s}. \tag{7.20}$$

Though the controller is designed based on two identical modules, it is applicable to the practical circuit when the two modules are not exactly the same. This can be seen from SIMPLORER circuit simulation result in Fig. 7.8. The inductor values

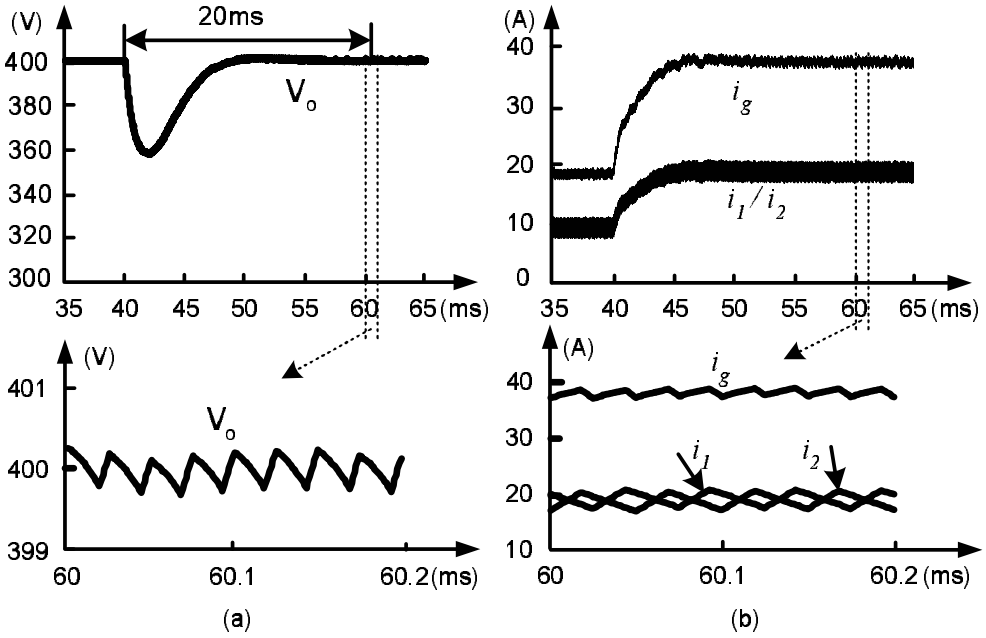

Figure 7.8: Simulation result during the load changing with closed loop control: (a) output voltage V_o; (b) input current i_g and inductor currents i_1/i_2

.

were taken as L_1 ($L = 178.8\mu H$, $r_1 = 64m\Omega$) and L_2 ($L = 177\mu H$, $r_2 = 68.6m\Omega$) for this simulation. When output power changes from $600W$ to $1200W$, it can be seen that output voltage is regulated back to $400V$ in about 20 ms, and the input current is equally distributed between the two inductors.

7.4 Controller implementation

Texas Instrument (TI) TMS320F243 DSP microcontroller is used to implement PWM functions and closed loop control. Four PWM gate signals with phase shift of 90^o are necessary for the proposed converter. However, there are only two indepen-

dent General Purpose (GP) timers in this type of DSP. Hence it can only generate two synchronized phase-shifted gate signals. Though the third gate signal can be obtained by manipulating the compare register of one of the six PWM output channels, it is not possible to obtain the fourth signal. Although this problem can be solved by using two DSP microcontrollers, it will increase the cost and introduce synchronization problem between the two DSP microcontrollers. One could also use a FPGA externally but that increases the component cost. Hence a simple method is proposed here to generate four phase-shifted gate signals using only one DSP microcontroller and one XOR gate. Working principle is shown in Fig. 7.9. All the functions in the dashed block are realized via software. Fig. 7.10 shows the experimental waveform of the phase shifted gate signals to the switches.

CMP1 and CMP2 are controllable parameters which are represented as D_1T_s and D_2T_s, where D_1 or D_2 is the duty ratio for each module respectively. CMP1 and CMP2 are written to compare registers and updated during each switching period T_s. T_s is written to both timer counter T1PR and T2PR as seen in Fig. 7.9. Timer2 is synchronized with Timer1 with phase delay of 90^o. By comparing CMP1 and CMP2 with Timer1 and Timer2 respectively, symmetric PWM waveforms S1, S2 and S5, S6 are generated as shown in Fig. 7.9. S5, S6 is delayed in phase by 90^o with respect to S1, S2, which can be seen in Fig. 7.10. By comparing (Ts - CMP1) with Timer1, S3, S4 (PWM1) is generated with 180^o phase shift to S1, S2 (Fig. 7.10). Similarly, by comparing 0.5Ts + (Ts - CMP2) and 0.5Ts - (Ts - CMP2) with Timer1 (Fig. 7.9),

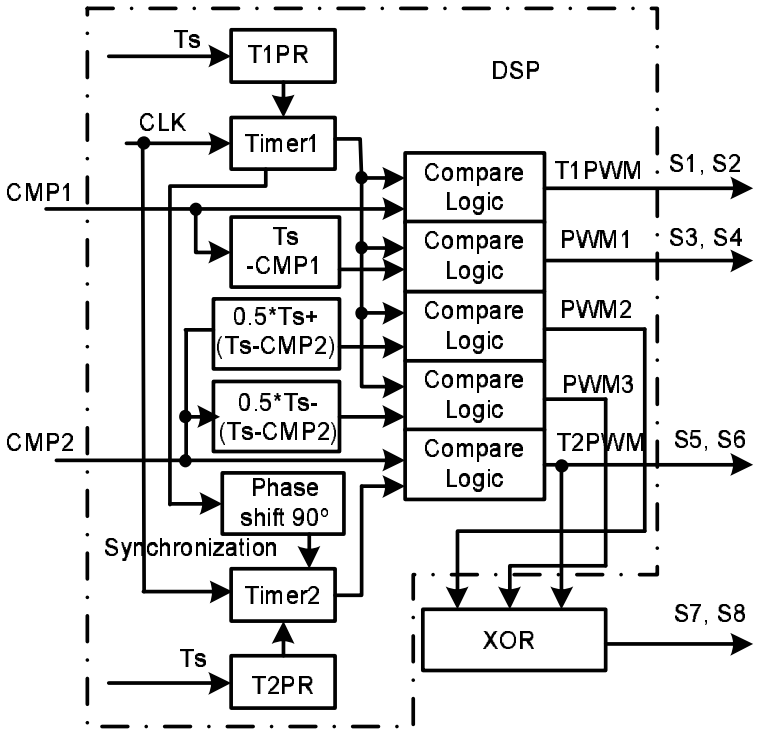

Figure 7.9: Diagram for generating four phase shifted gate signals using one DSP microcontroller

PWM2 and PWM3 can be obtained respectively. By XOR signals PWM2, PWM3 and S5, S6, signal S7, S8 is obtained, which is 180^o phase delayed respective to S5, S6 as shown in Fig. 7.10. Now all four gate signals are generated using one DSP microcontroller.

IR2110s are used as the MOSFET gate drivers. The sensed current and voltage signals are fed back to the DSP core by 10 bit ADC channels. Once this is done, the digitized feedback voltage V_{out}, is subtracted from the reference voltage. The error signal V_{err}, is an input to a digital PI compensator and output is saved as the current reference after a limiter. The current reference is divided equally to feed as

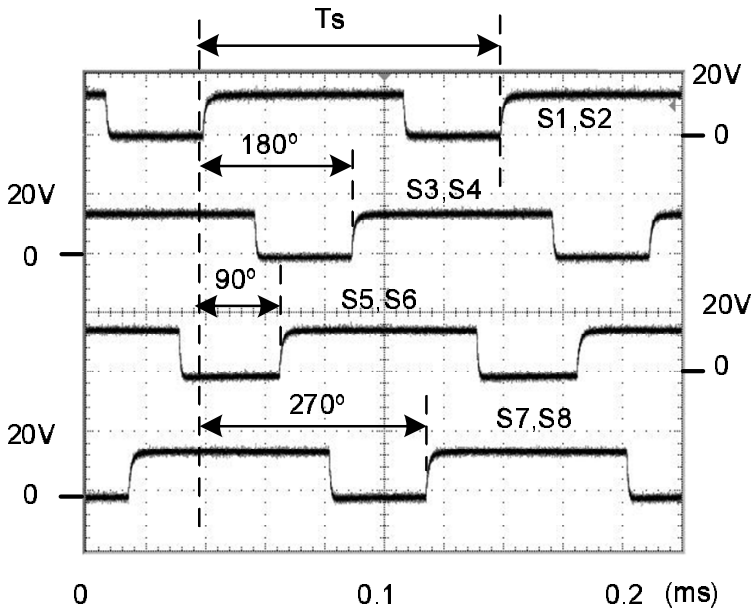

Figure 7.10: Phase shifted gate signals for ICFFB (experiment)

the inductor reference current. Again, the errors between the reference current and the measured current are compensated and written to the PWM generator as CMP1 and CMP2. Flow chart for the main program and interrupt service routine are shown in Fig. 7.20 and Fig. 7.21 (please refer to the rear part of this chapter).

7.5 Experimental Results

A $1.2kW$ interleaved current-fed full bridge converter is built and tested. Experimental circuit specifications are listed in Table 7.2.

Fig. 7.11 shows the steady-state waveforms of the ICFFB converter when operating at $1120W$. It is observed that inductor current ripple is about 20% of rated

Table 7.2: Converter specification

Switching frequency	$f_s = 10kHz$
Maximal output power	$1200W$
Switches	IXFK90N20 MOSFETs, $R_{DS(ON)} = 40m\Omega(100^oC)$
Diodes	$4\times$Ultra fast MUR860 $8A/600V$
Output capacitors	$100\mu F$,$200V$ Electrolytic + $0.027\mu F$ polyester
Snubber capacitors	$0.44\mu F$ polyester
Input inductors	$E305-26$, Iron powder core L_1: $178.8\mu H$, $r_1 = 64m\Omega$, L_2: $177\mu H$, $r_2 = 68.6m\Omega$
Transformers	$EC70$, Ferrite core$-3C90$, $n_1/n_2 = 1:2$ $L_m = 931.7\mu H$, leakage inductance $L_k = 4.9\mu H$

inductor current. While the input current ripple is reduced to 5% of the rated input current due to the phase shift between the two parallelled converters. Fig. 7.11 (c) shows the waveform of the output voltage ripple. It must be noted that due to the effect of ESR of the output capacitor and the leakage inductance of the transformer, this ripple waveform looks different from the one in Fig. 7.2, which is based on ideal analysis. The voltage ripple is about $3V$, which is only 0.75% of the rated voltage.

Fig. 7.12 shows the measured efficiency of the ICFFB converter for increasing output power from $0W$ to $1120W$. Efficiency is 90.5% at $1120W$. Fig. 7.13 (a) shows the dynamic response of the proposed converter for a load step from $90W$ to $135W$.

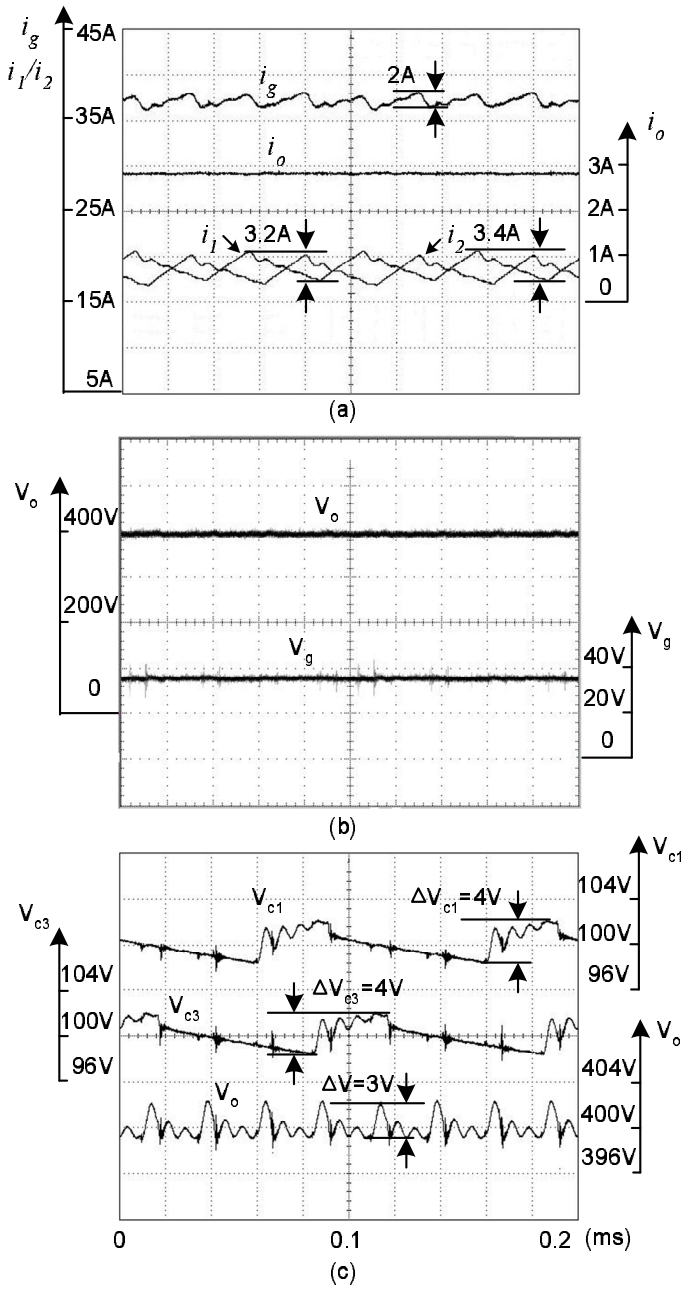

Figure 7.11: Steady state waveforms of the ICFFB converter at $1120W$ (experiment) (a) input current i_g, inductor currents i_1/i_2 and output current i_o; (b) output voltage V_o and input voltage V_g; (c) output capacitor voltage ripple ΔV_{c1}, ΔV_{c3} and output voltage ripple ΔV

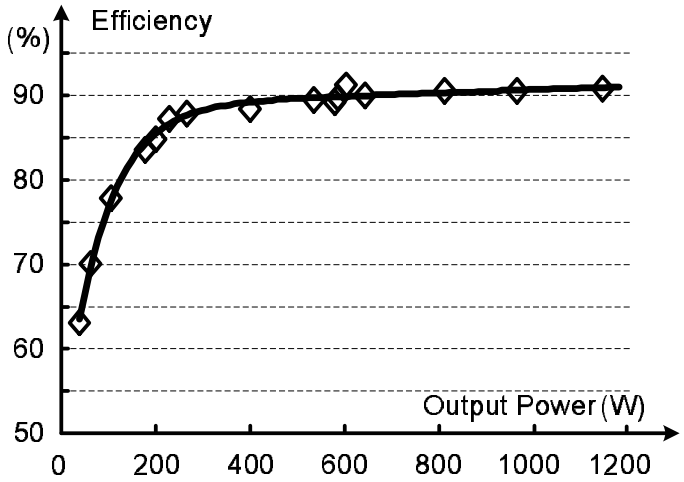

Figure 7.12: Measured converter efficiency vs. output power (experiment) ($D = 0.67$, $V_o = 400V$)

The voltage sag is about $20V$. While Fig. 7.13 (b) shows the dynamic response for a load step from $135W$ to $90W$. Voltage overshoot is about $25V$. From both Fig. 7.13 (a) and (b), it can be seen that input current can quickly reach its new steady state while output voltage can be regulated at $150V$ in about 20 ms.

Table 7.3 gives the comparison of magnetic components for the ICFFB converter and the CFFB converter. From the table, it can be seen that core volume and total weight of the magnetic components of the ICFFB converter have been reduced by about 50%. Efficiency of ICFFB converter is 1.5% greater than that of CFFB converter at full load. It is also noted from Table 7.3 that the number of switches used in ICFFB converter is twice of that in CFFB converter. However one can use lower rating components. Under faulty condition when one of the converter modules fails, it is still able to operate the system at quarter load. In this case, the output voltage has to be reduced to half of the rated voltage.

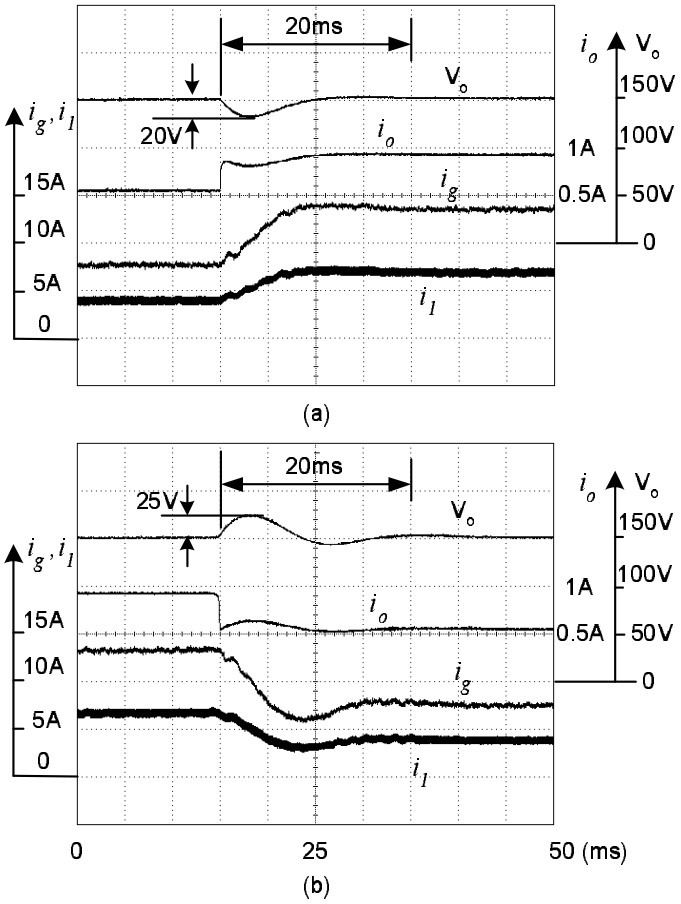

Figure 7.13: Dynamic response of output voltage V_o, output current i_o, input current i_g and inductor current i_1 (experiment) (a) Load steps from $90W$ to $135W$; (b) Load steps from $135W$ to $90W$.

7.6 Soft Start-up Scheme

For a boost-type isolated converter, output voltage reflected to the primary side of the transformer is greater than the input voltage during normal operating stage. However when the converter initially turns on, output capacitor is not charged up yet. This causes large inrush current. Control strategy designed for steady-state stage is no longer applicable during the start-up transient period. Thus external circuits

Table 7.3: Comparison between ICFFB and CFFB converters

	ICFFB	CFFB
Inductors	$2 \times 178\mu H$	$279\mu H$
Core volume	$2 \times 104cm^3$	$344cm^3$
Weight	$2 \times 728g$/set	$1940g/set$
Transformer		
Core volume	$2 \times 40.2cm^3$	$344cm^3$
Weight	$2 \times 252g$/set	$1940g/set$
Total core volume	$288.4cm^3$	$688cm^3$
Total weight	$1960g$	$3880g$
No. of switches	16×IXFK90N20	8×IXFK90N20
Efficiency at full load	$90.5\%(1.12kW)$	$89\%(1.14kW)$

are usually required for boost-type converters to suppress the high inrush current by establishing an initial output voltage before the converter operates in normal boost mode. For low power boost converter, a thermistor or a resistor is usually put on the input side to limit the inrush current [77] [78] [79]. But for high power converter, where input current is high, putting a thermistor or resistor is not an efficient solution due to the high power loss on the thermistor/resistor. Lizhi Zhu [80] proposed a new topology to suppress the inrush current for current-fed full bridge converters by using an additional flyback winding coupled with the input inductor choke. But this

obviously increases the size of the input inductor and the complexity of the controller.

To understand the generation of large inrush current during the start-up stage, it is better to look at what happens to the input inductors in this process. Since the control sequence of the second module is the same as the first one except a 90^o phase shift, it is possible to investigate the equivalent circuit of one converter only. Voltage across the input inductor V_L is V_g (Fig. 7.14 (a)) when all switches are on. While V_L is $V_g - \frac{V_{os}}{2n}$ (Fig. 7.14 (b)) when any two diagonal switches are off. In normal boost operation where $\frac{V_{os}}{2n}$ is always greater than V_g, V_L in this state is negative. That is how the volt-seconds balance of the inductor can be maintained in steady-state. However during start-up stage, initially output voltage is zero and it takes some time to build up the output voltage V_o. Before $V_{os} \geq 2nV_g$, inductor voltage V_L is positive for all switching states. Thus volt-seconds balance is lost and the inductor current keeps increasing. A prolonged increase in inductor current causes the inrush current on the input side during start-up process.

One of the promising advantages of the proposed ICFFB converter is its soft start-

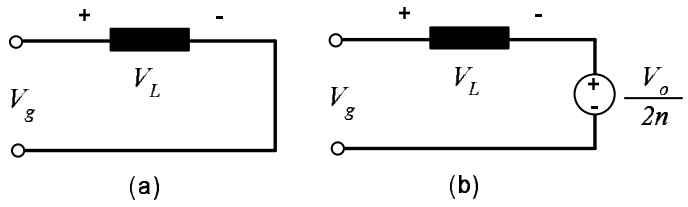

Figure 7.14: Equivalent circuit of one module of the ICFFB converter

up capability without adding any external circuit except a switch of small current

rating. Strategy to start up the circuit is simple and can be implemented on a digital signal processor. Since an overlap of all switches is necessary to charge the input inductor, duty ratio D is greater than 0.5 at normal operating stage. Hence how to change D smoothly from initial zero to a value greater than 0.5 is important to suppress inrush current during start-up. But it is also known that control scheme designed for the ICFFB converter is only valid for normal boost operation where $D > 0.5$. Hence different control scheme has to be used for start-up stage where $D < 0.5$.

As shown in Fig. 7.15 (a), an auxiliary switch S_s is put on the load side to aid the soft start-up. Initially during the start-up stage, S_s is kept open and D increases from zero to $D = 0.5$ at a slow rate of about $0.1V/s$. When output voltage is greater than $264V$ $(2 * 2nV_g = 2 * 2 * 2 * 33V)$, S_s is turned on and normal operation is enabled. As shown in Fig. 7.15 (b), during the start-up process, 90^o phase shift still remains among all the four switching gate signals. Since the load is disconnected during the start-up stage, the circuit analysis can be simplified by looking at only one converter. The same circuit analysis can be applied to the other converter by shifting all signals with 90^o phase angle. Equivalent circuits and circuit analysis for one converter is shown in Fig. 7.16. In the following detailed description, an ideal transformer is considered and $C_1 = C_2 = C_3 = C_4 = C$, $C_{s1} = C_{s2} = C_s$.

1. **State** $t_0 - t_1$ [Fig. 7.16 (a)]:

   At t_0, switches S_1 and S_2 turn on, L_1 is charged up. C_2 is charged up by means

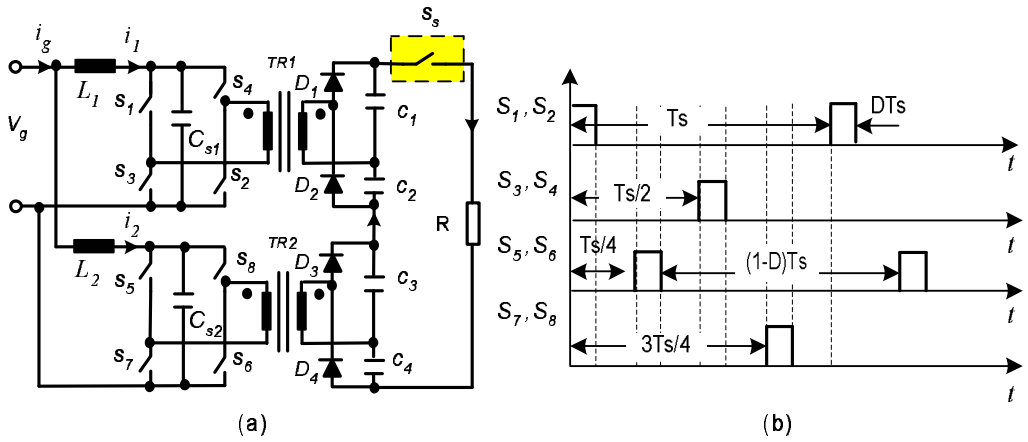

Figure 7.15: Control signals during the start-up stage

.

of D_2. Voltage across the snubber capacitor V_{Cs1} is reset to $\frac{V_{C2}(t)}{n}$, as shown in Fig. 7.16 (g). By converting circuit parameters on the secondary side of the transformer to equivalent parameters on the primary side, equivalent circuit during this state is obtained in Fig. 7.16 (a). Inductor current i_{L1} and snubber capacitor voltage $V_{Cs1}(t)$ are derived as following:

$$\begin{cases} i_{L1}(t) = I_{P1} \sin \omega(t - t_0), \\ V_{C2}(t) = V_{C2}(t_0) + V_{P1} \sin \omega(t - t_0) - V_{P2} \cos \omega(t - t_0), \\ V_{Cs1}(t) = V_{C2}(t)/n. \end{cases} \tag{7.21}$$

Where

$$\begin{cases} \omega = \sqrt{\dfrac{1}{(C_s + Cn^2)L}}, \quad I_{P1} = \omega((C_s + Cn^2)V_g - CnV_{C2}(t_0)), \\ V_{P1} = \omega(nV_g - V_{C2}(t_0)), \quad V_{P2} = \omega^2 C_s L V_{C2}(t_0). \end{cases} \tag{7.22}$$

At $t = t_1$, inductor current is $i_{L1}(t_1)$ and snubber capacitor voltage is $V_{Cs1}(t_1)$.

2. **State** $t_1 - t_2$ [Fig. 7.16 (b)]:

   At t_1, switches $S_1 \sim S_4$ turn off, the equivalent circuit (as shown in Fig. 7.16 (b) becomes a series resonant circuit. L_1 is charged up until V_{Cs1} becomes greater than V_g. After that, i_{L1} decreases with the angular resonant frequency ω_1 until at t_2, i_{L1} becomes zero and V_{Cs1} reaches its maximum value (as shown in Fig. 7.16 (g)). Expressions of i_{L1} and $V_{Cs1}(t)$ during this state are:

$$\begin{cases} i_{L1}(t) = i_{L1}(t_1)\cos\omega_1(t-t_1) + \dfrac{V_g - V_{cs1}(t_1)}{Z_r}\sin\omega_1(t-t_1), \\ V_{Cs1}(t) = V_g - (V_g - V_{Cs1}(t_1))\cos\omega_1(t-t_1) + i_{L1}(t_1)Z_r\sin\omega_1(t-t_1). \end{cases} \tag{7.23}$$

   Where

$$\omega_1 = \sqrt{\frac{1}{LC_s}}, \quad Z_r = \sqrt{\frac{L}{C_s}}. \tag{7.24}$$

   At $t = t_2$, i_{L1} reaches zero. Duration of this state can be obtained as

$$\Delta t = t_2 - t_1 = \frac{1}{\omega_1}\arctan\frac{i_{L1}(t_1)Z_r}{V_g - V_{Cs1}(t_1)}. \tag{7.25}$$

3. **State** $t_2 - t_3$ [Fig. 7.16 (c)]:

   Since inductor current i_{L1} is zero during this state, V_{Cs1} remains at its maximum value of $V_{Cs1}(t_2)$ (as shown in Fig. 7.16 (g)).

4. **State** $t_3 - t_4$ [Fig. 7.16 (d)]:

   At $t = t_3$, switches S_3 and S_4 turn on. C_1 is now charged up by means of D_1. Voltage across the snubber capacitor is immediately reset to $\frac{V_{C1}(t)}{n}$, as shown in Fig. 7.16 (g). After converting the circuit parameters on the secondary side

of the transformer to equivalent parameters on the primary side, an equivalent circuit is obtained in Fig. 7.16 (d), which is similar as Fig. 7.16 (a) expect that it is capacitor C_1 conducting now. Expressions of i_{L1} and $V_{Cs1}(t)$ during this state are:

$$\begin{cases} i_{L1}(t) = I_{P1} \sin \omega(t - t_3), \\ V_{C1}(t) = V_{C1}(t_3) + V_{P1} \sin \omega(t - t_3) - V_{P2} \cos \omega(t - t_3), \\ V_{Cs1}(t) = V_{C1}(t)/n. \end{cases} \tag{7.26}$$

Where

$$\begin{cases} \omega = \sqrt{\dfrac{1}{(C_s + Cn^2)L}}, \quad I_{P1} = \omega((C_s + Cn^2)V_g - CnV_{C1}(t_3)), \\ V_{P1} = \omega(nV_g - V_{C1}(t_3)), \quad V_{P2} = \omega^2 C_s L V_{C1}(t_3). \end{cases} \tag{7.27}$$

5. **State** $t_4 - t_5$ [Fig. 7.16 (e)]:

   Same as what happens in **State** $t_1 - t_2$, the open of switches $S_1 \sim S_4$ again results a series resonant circuit, as shown in Fig. 7.16 (e). Waveforms are the same as that in **State** $t_1 - t_2$. i_{L1} and $V_{Cs1}(t)$ during this state are:

$$\begin{cases} i_{L1}(t) = i_{L1}(t_4) \cos \omega_1(t - t_4) + \dfrac{V_g - V_{cs1}(t_4)}{Z_r} \sin \omega_1(t - t_4), \\ V_{Cs1}(t) = V_g - (V_g - V_{Cs1}(t_4)) \cos \omega_1(t - t_4) + i_{L1}(t_4) Z_r \sin \omega_1(t - t_4). \end{cases} \tag{7.28}$$

   Where ω_1 and Z_r are the same as in Eq. 7.24. At $t = t_5$, $i_{L1}(t_5) = 0$.

6. **State** $t_5 - t_6$ [Fig. 7.16 (f)]:

   Inductor current i_{L1} is zero and V_{Cs1} remains at its maximum value of $V_{Cs1}(t_5)$.

Waveforms of i_{L2} and V_{Cs2} are also plotted on Fig. 7.16 (g). They are the same as waveforms of i_{L1} and V_{Cs1} but shifted 90^o respectively.

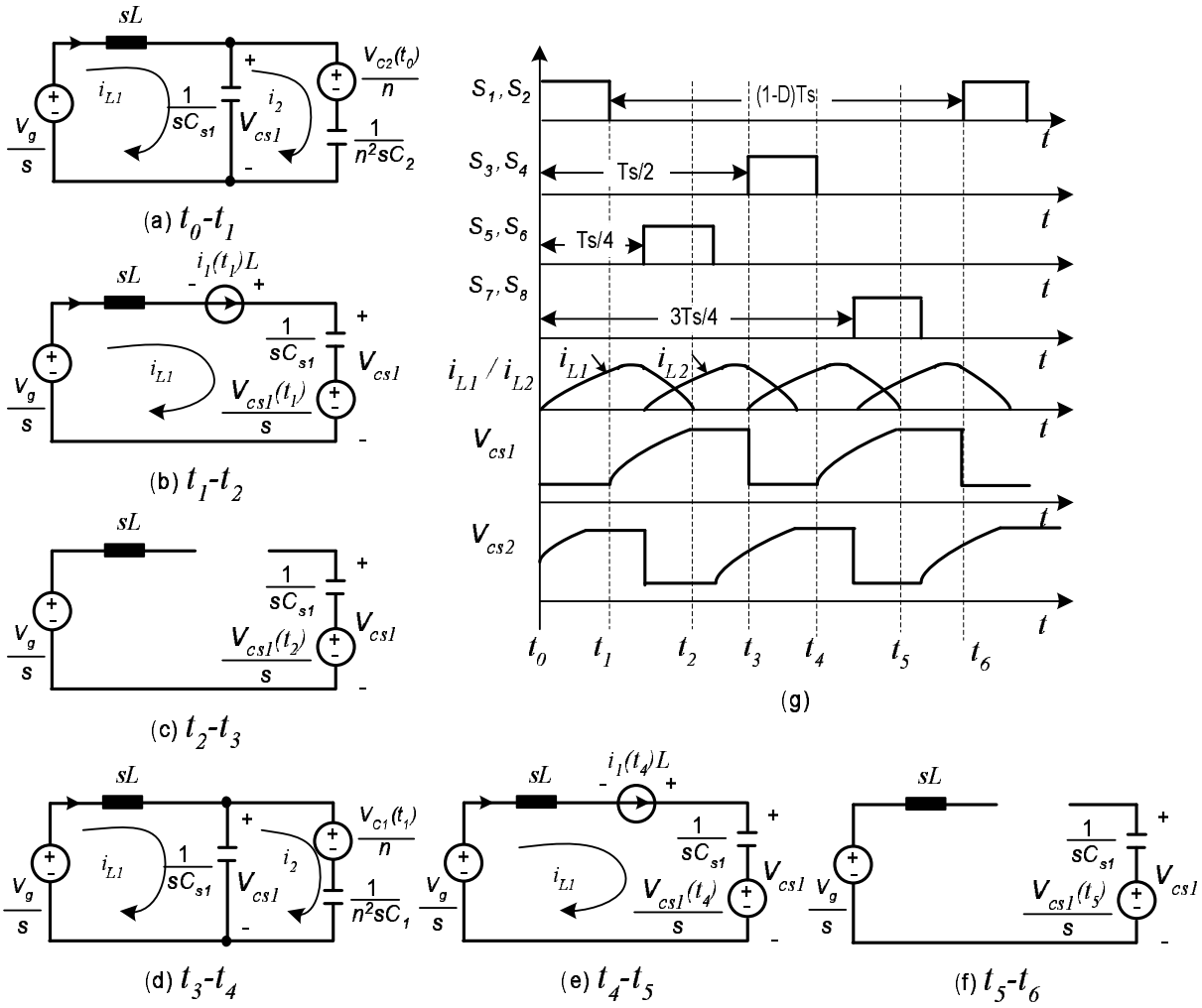

Figure 7.16: (a)∼(f) Equivalent circuits of the ICFFB converter (one converter module) during start-up stage; (c) Gate signals and main waveforms during start-up stage

.

To verify the analysis of the soft start-up scheme, circuit simulation is performed via SIMPLORER $V6.0$ software tools [87] using parameters defined as following:

Inductors: $L_1 = L_2 = 177\mu H$, Transformers: $n_1/n_2 = 1:2$;

Output capacitors: $C_1 \sim C_4 = 100\mu F$, Snubber capacitors: $C_{s1} = C_{s2} = 0.44\mu F$;
Input voltage $V_g = 33V$, Load $R = 266.67\Omega$;
Switching frequency $f_s = 10kHz$.

Simulated waveforms during soft start-up from zero to $600W$ are shown in Fig. 7.17. In the start-up stage, duty ratio D increases slowly from zero to 0.5 using the control sequence designed in Fig. 7.15 (b). Output voltage rises quickly to around $264V$ at $t = 34ms$ and the magnitude of the inductor current is less than $5A$ during the start-up stage, as shown in Fig. 7.17 (a). Also, it is noticed that although both of the inductor currents i_1/i_2 are discontinuous in the start-up process, input current i_g, which is the summation of these two is continuous and the current ripple has been greatly reduced due to the interleaving between i_1 and i_2 (Fig. 7.17 (c) (d)). At $t = 34ms$, S_s turns on when output voltage is greater than $264V$. Control sequence is changed to normal operation and a transient input current of $37A$ is observed. Output voltage V_o quickly reaches $400V$ with the closed-loop controller proposed in section 7.3.

Fig. 7.17 shows the fastest start-up process by turning on S_s when output voltage is greater than $264V$. The reason to choose $264V$ is because it is the minimum equivalent output voltage when the converter starts to work as a boost converter. But the inrush input current in Fig. 7.17 can be further reduced by charging the output capacitor closer to $400V$ with a longer start-up process. This can be realized by controlling when to turn on switch S_s. As the simulation result shown in Fig. 7.18,

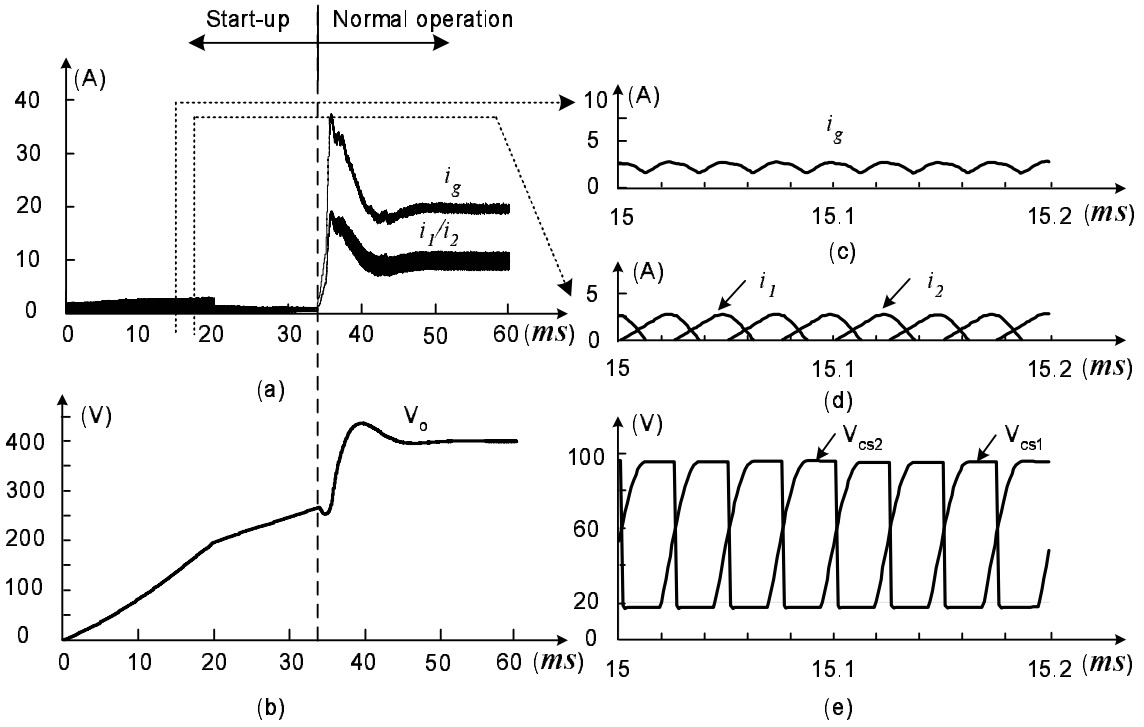

Figure 7.17: Characteristic waveforms during start-up (simulated) (a) Waveforms of input current i_g, inductor current i_1/i_2; (b) Waveforms of output voltage V_o, (c) Magnified waveforms of input current i_g; (d) Magnified waveforms of inductor current i_1/i_2; (e) Magnified waveforms of snubber capacitor voltage V_{Cs1}/V_{Cs2}.

D increases with the rate of $0.0125/ms$ until it reaches 0.5 at $40ms$. After that, D is saturated at 0.5 and the output voltage V_o keeps on increasing. Until at $60ms$ when output voltage reaches $360V$, S_s is turned on. Then start-up process ends and the converter enters the normal operation state. It is noticed that the inrush current can be reduced to about $34A$. But the start-up period is almost twice of what showed in Fig. 7.17.

This soft start-up scheme is implemented on DSP TMS320F243. Realization of the transition from start-up stage to normal operation is indicated within the dashed

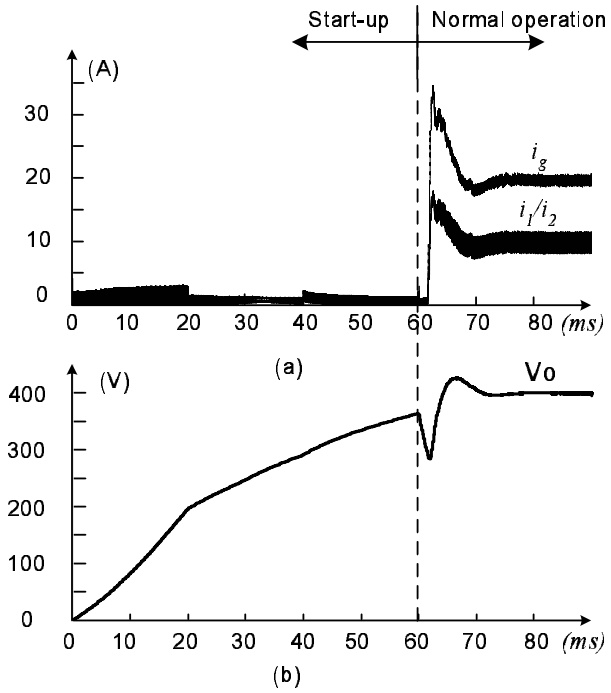

Figure 7.18: Waveforms during start-up with smaller inrush current(input current i_g, inductor current i_1/i_2 and output voltage V_o)

box in the flow chart shown in Fig. 7.21. Fig. 7.19 shows the experimental results when the proposed ICFFB converter starts from zero to $600W$. It can be seen that inrush current is absent during the start-up and output voltage can slowly reach $400V$.

7.7 Summary

An interleaved current-fed full bridge converter (ICFFB) is proposed in this chapter with a parallel input/series output scheme to solve the problems in conventional CFFB converters. By paralleling input of the converter system, input current and

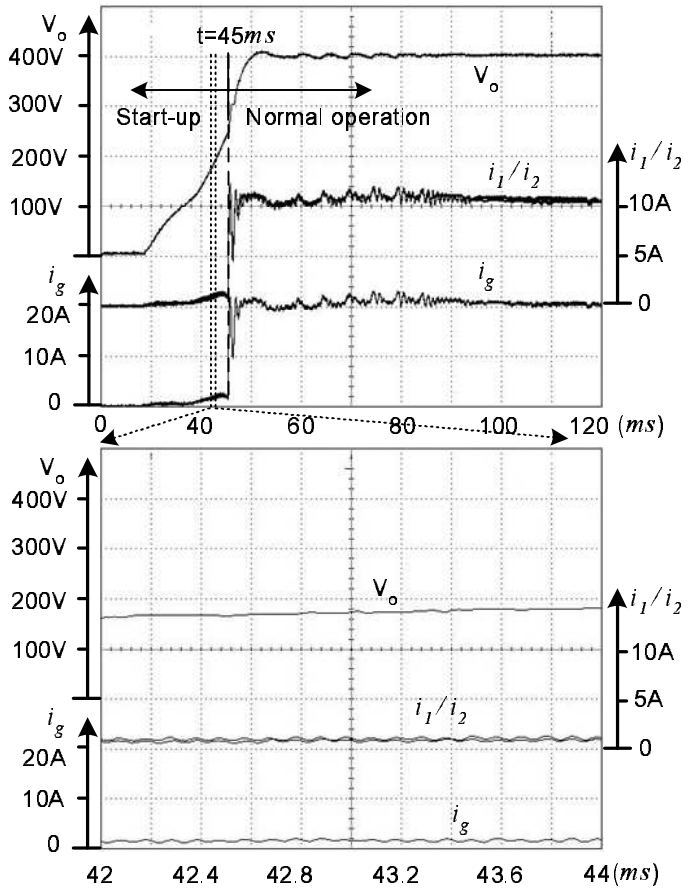

Figure 7.19: Waveforms of output voltage V_o, input current i_g and inductor currents i_1/i_2 during start-up from $0W$ to $600W$ (experiment)

power are equally shared between the modules of the converter system. Current stress on the semiconductor devices on the input side is reduced. On the other hand, the series connection on the output side results in lower voltage ratings for output capacitors and diodes. Moreover the input current ripple frequency and the output voltage ripple frequency becomes four times of the switching frequency due to the interleaving of the converter modules. Hence for the same input current and output voltage ripple requirement, smaller input inductors and output capacitors can be used. An-

other advantage of the ICFFB converter is its soft start-up capability without adding additional start-up circuit except a switch of small current rating. With the aid of the snubber capacitor and this switch, large inrush current during start-up stage is eliminated.

A $1.2kW$ ICFFB converter is built and tested. All PWM signals, closed loop controller and soft start-up is implemented on one DSP board. Input current ripple is about 5% of the rated input current. Total core volume and weight of magnetic components are reduced by 50%. Furthermore, about 90.5% efficiency is obtained at full power. Based on high efficiency, small magnetic components, small input current ripple and soft start-up capability, this ICFFB converter seems to be more suitable for a high power fuel cell system.

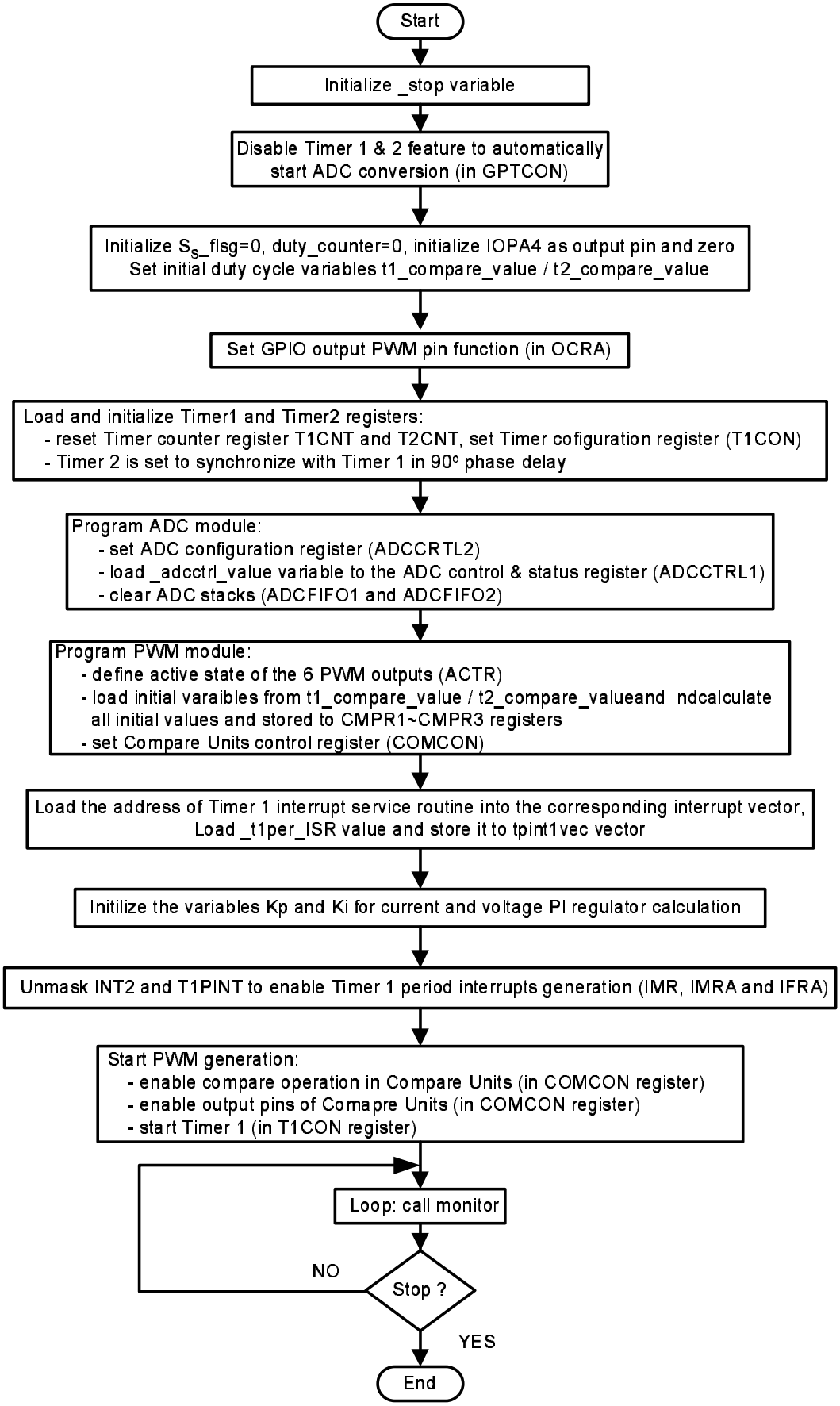
Start
Initialize _stop variable
Disable Timer 1 & 2 feature to automatically start ADC conversion (in GPTCON)
Initialize S_S_flsg=0, duty_counter=0, initialize IOPA4 as output pin and zero
Set initial duty cycle variables t1_compare_value / t2_compare_value
Set GPIO output PWM pin function (in OCRA)
Load and initialize Timer1 and Timer2 registers:
- reset Timer counter register T1CNT and T2CNT, set Timer cofiguration register (T1CON)
- Timer 2 is set to synchronize with Timer 1 in 90° phase delay
Program ADC module:
- set ADC configuration register (ADCCRTL2)
- load _adcctrl_value variable to the ADC control & status register (ADCCTRL1)
- clear ADC stacks (ADCFIFO1 and ADCFIFO2)
Program PWM module:
- define active state of the 6 PWM outputs (ACTR)
- load initial varaibles from t1_compare_value / t2_compare_valueand ndcalculate all initial values and stored to CMPR1~CMPR3 registers
- set Compare Units control register (COMCON)
Load the address of Timer 1 interrupt service routine into the corresponding interrupt vector, Load _t1per_ISR value and store it to tpint1vec vector
Initilize the variables Kp and Ki for current and voltage PI regulator calculation
Unmask INT2 and T1PINT to enable Timer 1 period interrupts generation (IMR, IMRA and IFRA)
Start PWM generation:
- enable compare operation in Compare Units (in COMCON register)
- enable output pins of Comapre Units (in COMCON register)
- start Timer 1 (in T1CON register)
Loop: call monitor
NO
Stop ?
YES
End

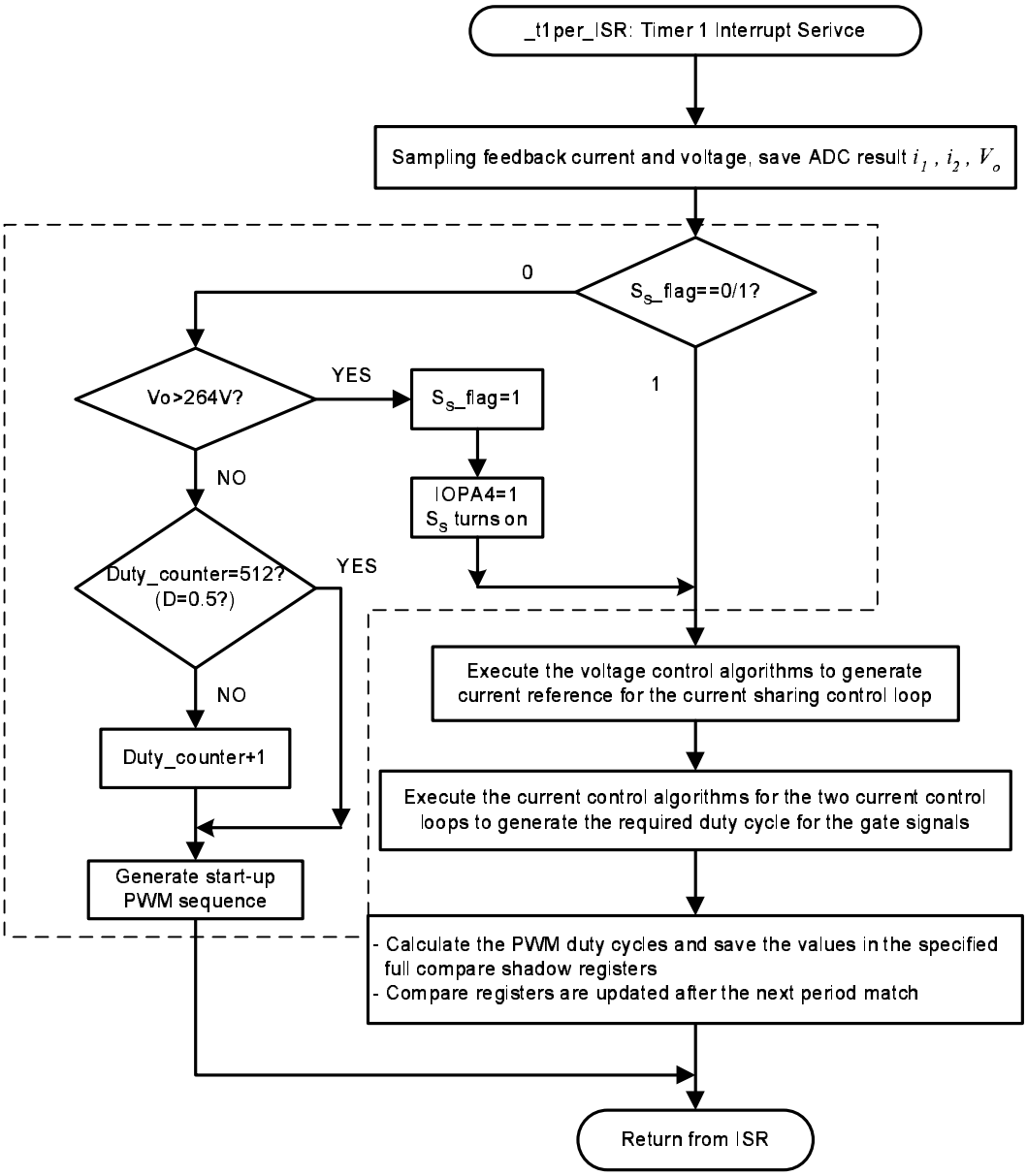

Figure 7.21: Flow chart for interrupt service routine

Chapter 8

Combined Feed-forward/Feedback Controller for ICFFB Converter

In Chapter 6, an ICFFB converter is proposed with a parallel input/series output construction to solve the problems in conventional CFFB converters. It has small input current/output ripples and soft start-up capability. In order to control the input current and output voltage of the ICFFB converter, a cascaded PI controller was designed and implemented. Since the ICFFB converter is an inherent boost type converter, the small signal control-to-output voltage transfer function presents a RHP zero. The presence of RHP zero prevents achievement of good closed-loop bandwidth resulting in slow dynamic response [88]. To minimize the effect of RHP zero, following methods have been suggested in literature: reducing inductor value, reducing switching frequency, operating in discontinuous-conduction mode (DCM) [89]

and changing the converter structure [90]. Reducing inductor value and operating in DCM results large input current ripple, which is undesirable for fuel cell applications. While reducing switching frequency increases the size of passive components in the converter. Changing converter structure can effectively eliminate RHP zero, but it is at the cost of lower efficiency. In this chapter, a combined feed-forward/feedback controller is proposed to minimize the RHP zero effect by "shaping" the trajectory of the minimum phase variable–input current, therefore reduces the undershoot and settling time during the transient response.

8.1 Combined Feed-forward/Feedback Controller Design

To understand the idea of this combined feed-forward/feedback controller, a conventional PI controller is first shown in Fig. 8.1, which was designed in Chapter 6. Since the ICFFB converter has two identical CFFB modules paralleled at the input side and connected in series at the output side, it would be easier to study the whole circuit performance by investigating only one module. Closed loop transfer functions of the inner current loop and outer voltage loop are shown as follows:

$$\begin{cases} \dfrac{\hat{i}_g(s)}{\hat{i}_{ref}(s)} = \dfrac{C_i(s)}{1 + C_i(s)G_{id}(s)} \\ \dfrac{\hat{V}_o(s)}{\hat{V}_{ref}(s)} = \dfrac{C_v(s)T_i(s)G_{vi}(s)}{1 + C_v(s)T_i(s)G_{vi}(s)} \end{cases} \tag{8.1}$$

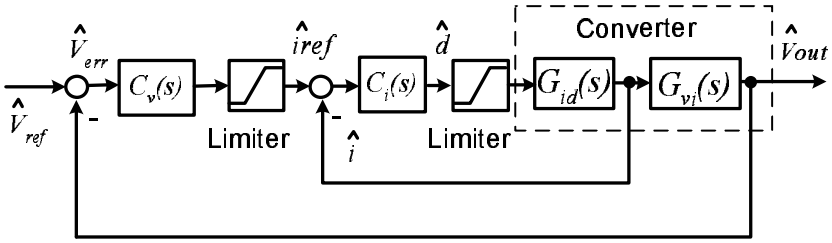

Figure 8.1: Schematic diagram of the cascaded controller

Where

$$\begin{cases} T_i(s) = \dfrac{C_i(s)G_{id}(s)}{1 + C_i(s)G_{id}(s)} \\ G_{id} = \dfrac{\hat{i}(s)}{\hat{d}(s)} = \dfrac{\dfrac{CV_o}{n}s + \dfrac{4V_o}{nR}}{LCs^2 + (\dfrac{2L}{R} + r_L C)s + \dfrac{2r_L}{R} + 2(\dfrac{D'}{n})^2} \\ G_{vi} = \dfrac{\hat{v}_o(s)}{\hat{i}(s)} = \dfrac{\dfrac{-2LV_o}{RD'}s + 2V_o(\dfrac{D'}{n^2} - \dfrac{r_L}{RD'})}{\dfrac{CV_o}{n}s + \dfrac{4V_o}{nR}} \end{cases} \tag{8.2}$$

$C_i(s)$ and $C_v(s)$ in Eq.8.1 are PI compensators. To help understand it clearly, following converter parameters in Tab. 8.1 are substituted into Eq. 8.2 to obtain Eq. 8.3.

Table 8.1: Converter parameter definition

L	$180\mu H$	C	$100\mu F$	r_L	0	n	2
R	266.7Ω	D'	0.33	V_o	$200V$	V_g	$33V$

$$\begin{cases} \dfrac{\hat{i}(s)}{\hat{d}(s)} = \dfrac{5.556e5(s + 150)}{s^2 + 75s + 3.025e6} \\ \dfrac{\hat{v}_o(s)}{\hat{d}(s)} = \dfrac{-4.5454e4(s - 40330)}{s^2 + 75s + 3.025e6} \end{cases} \tag{8.3}$$

Eq. 8.3 clearly shows that the control-to-output current loop is a minimum system while the control-to-output voltage loop is a non-minimum system with a RHP zero

at $s = 40330$. Since the current reference $\hat{i}_{ref}$ is obtained from the integration of voltage error $\hat{V}_{err}$, it takes time for the current to reach its new state and the voltage undershoot is usually large. Moreover, due to the presence of the RHP zero, there is a voltage dip in the response at the beginning of a unit step, which aggravates the undershoot. To overcome this problem, the state variable i_g can be controlled by shaping waveform of the current reference. This is realized through a combined feed-forward/feedback controller shown in Fig. 8.2. Two controllers are switched based

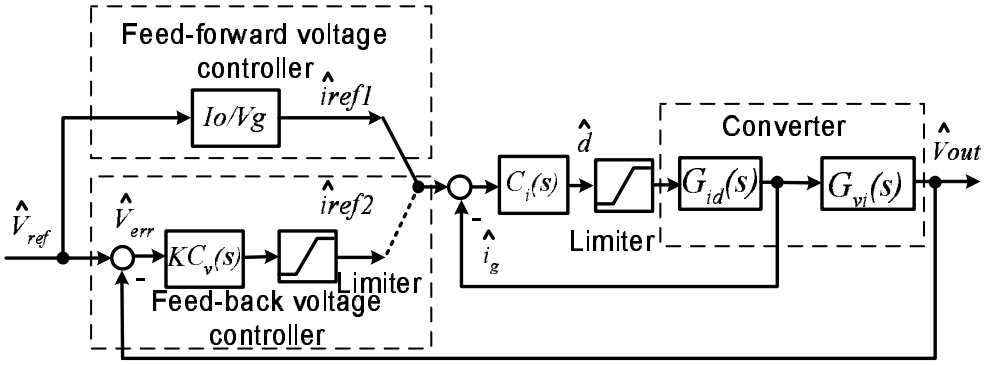

Figure 8.2: Schematic diagram of combined feed-forward/feedback controller

on certain condition to generate different current reference. Feed-forward voltage controller is used to generate i_{ref1}, while feedback voltage controller is used to generate i_{ref2}. Current reference is changed over between i_{ref1} and i_{ref2} under certain criteria. Since there is no voltage feedback in the feed-forward voltage controller, input current i_g can be steered quickly to its new state, hence a fast transient response can be achieved. However precise regulation of voltage V_o is hardly possible due to the parasitic resistance in the system and lack of voltage error compensation. On the

other hand, as explained earlier, the feedback voltage controller using PI controller, shows slower transient response and larger undershoot, but precise regulation of the control variables can be guaranteed.

8.2 Stability of Combined Feed-forward/Feedback Controller

8.2.1 Analysis of Feed-forward voltage Controller

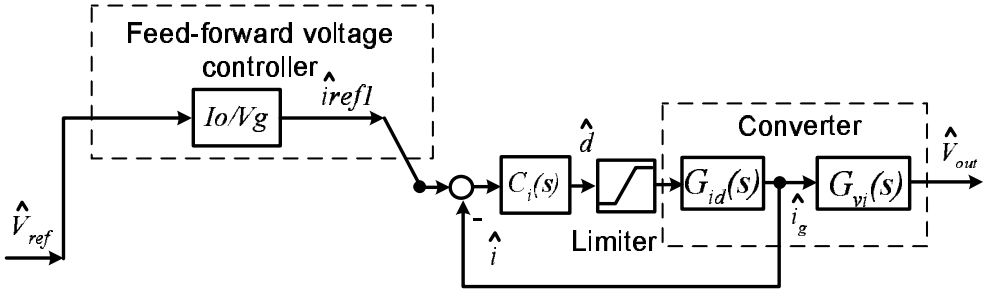

Figure 8.3: Schematic diagram of feed-forward voltage controller

Closed loop transfer functions of the converter can be obtained from Fig. 8.3, which shows the schematic diagram of the feed-forward voltage controller only.

$$\begin{cases} G_{ffv}(s) = \dfrac{V_o}{V_{ref}} = \dfrac{I_o}{V_g} * \dfrac{C_i(s)G_{id}(s)G_{vi}(s)}{1 + C_i(s)G_{id}(s)}, \\ G_{ffi}(s) = \dfrac{i_g}{V_{ref}} = \dfrac{I_o}{V_g} * \dfrac{C_i(s)G_{id}(s)}{1 + C_i(s)G_{id}(s)}. \end{cases} \tag{8.4}$$

Substituting the parameters in Tab. 8.1 into the above equations,

$$G_{ffv}(s) = \frac{-18.7596(s - 4.033e4)(s + 3539)}{(s + 127.6)(s^2 + 4998s + 2.102e7)}. \tag{8.5}$$

$$G_{ffi}(s) = \frac{229.2871(s+150)(s+3539)}{(s+127.6)(s^2+4998s+2.102e7)}. \tag{8.6}$$

As it is known, if the roots of the denominator of a transfer function $F(s)$ is λ_1, λ_2, $\cdots\cdots$, λ_n,

$$F(s) = \frac{b_m s^m + b_{m-1}s^{m-1} + \cdots + b_1 s + b_0}{a_n s^n + a_{n-1}s^{n-1} + \cdots + a_1 s + a_0}, \quad n > m. \tag{8.7}$$

Then the inverse Laplace transformation of $F(s)$ can be obtained as:

$$f(t) = k_1 e^{\lambda_1 t} + k_2 e^{\lambda_2 t} + \cdots + k_n e^{\lambda_n t}. \tag{8.8}$$

Where

$$k_l = [(s-\lambda_l)F(s)]|_{s-\lambda_l}, \quad l = 1, 2, \cdots, n. \tag{8.9}$$

Similarly,

$$f'(t) = k_1\lambda_1 e^{\lambda_1 t} + k_2\lambda_2 e^{\lambda_2 t} + \cdots + k_n\lambda_n e^{\lambda_n t}. \tag{8.10}$$

Using the above method, inverse Laplace transformation of $G_{ffv}(s)$ and $G_{ffi}(s)$ can be obtained as:

$$G_{ffv}(t) = k_1 e^{\lambda_1 t} + k_2 e^{\lambda_2 t} + k_3 e^{\lambda_3 t}. \tag{8.11}$$

Where

$$\begin{cases} \lambda_1 = -127.6 & k_1 = 127.464, \\ \lambda_2 = -2499 + 3843.9j & k_2 = -72.8420 - 57.0344j, \\ \lambda_3 = -2499 - 3843.9j & k_3 = -72.8420 + 57.0344j. \end{cases} \tag{8.12}$$

Similarly,

$$G_{ffi}(t) = k_1 e^{\lambda_1 t} + k_2 e^{\lambda_2 t} + k_3 e^{\lambda_3 t}. \tag{8.13}$$

Where

$$\begin{cases} \lambda_1 = -127.6 & k_1 = 0.8590, \\ \lambda_2 = -2499 + 3843.9j & k_2 = -114.33 - 31.452j, \\ \lambda_3 = -2499 - 3843.9j & k_3 = -114.33 + 31.452j. \end{cases} \tag{8.14}$$

8.2.2 Analysis of Feedback voltage Controller

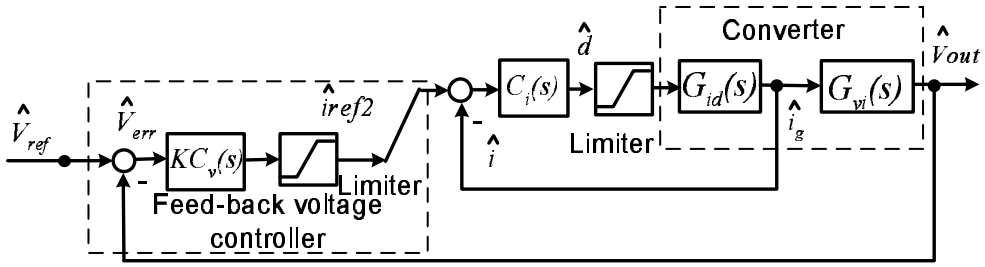

Figure 8.4: Schematic diagram of feedback voltage controller

Closed loop transfer functions of the converter with feedback voltage controller can be obtained from Fig. 8.4.

$$\begin{cases} G_{fbv}(s) = \dfrac{V_o}{V_{ref}} = \dfrac{KC_v(s)T_i(s)G_{vi}(s)}{1 + KC_v(s)T_i(s)G_{vi}(s)} \\ G_{fbi}(s) = \dfrac{i_g}{V_{ref}} = \dfrac{KC_v(s)T_i(s)}{1 + KC_v(s)T_i(s)G_{vi}(s)} \end{cases} \tag{8.15}$$

Where

$$T_i(s) = \frac{C_i(s)G_{id}(s)}{1 + C_i(s)G_{id}(s)}. \tag{8.16}$$

K is an adjustable coefficient, here it is chosen as $K = 2$. Substituting the parameters in Tab. 8.1 into the above equations:

$$G_{fbv}(s) = \frac{-136.992(s - 4.033e4)(s + 3539)(s + 565.9)}{(s^2 + 1051s + 5.035e5)(s^2 + 3937s + 2.198e7)}. \tag{8.17}$$

$$G_{fbi}(s) = \frac{1674.4(s+150)(s+3539)(s+565.9)}{(s^2+1051s+5.035e5)(s^2+3937s+2.198e7)}. \tag{8.18}$$

Applying the same method in Eq. 8.7 $\sim$ Eq. 8.9, the inverse Laplace transformation of $G_{fbv}(s)$ and $G_{fbi}(s)$ can be obtained:

$$G_{fbv}(t) = k_1 e^{\lambda_1 t} + k_2 e^{\lambda_2 t} + k_3 e^{\lambda_3 t} + k_4 e^{\lambda_4 t}. \tag{8.19}$$

Where

$$\begin{cases} \lambda_1 = -525.50 + 476.29j & k_1 = 428.27 - 3.5453j, \\ \lambda_2 = -525.50 - 476.29j & k_2 = 428.27 + 3.5453j, \\ \lambda_3 = -1968.5 + 4255j & k_3 = -496.78 - 486.11j, \\ \lambda_4 = -1968.5 - 4255j & k_4 = -496.78 + 486.11j. \end{cases} \tag{8.20}$$

Similarly,

$$G_{fbi}(t) = k_1 e^{\lambda_1 t} + k_2 e^{\lambda_2 t} + k_3 e^{\lambda_3 t} + k_4 e^{\lambda_4 t}. \tag{8.21}$$

Where

$$\begin{cases} \lambda_1 = -525.50 + 476.29j & k_1 = -48.3151 + 60.8595j, \\ \lambda_2 = -525.50 - 476.29j & k_2 = -48.3151 - 60.8595j, \\ \lambda_3 = -1968.5 + 4255j & k_3 = 885.53 - 266.29j, \\ \lambda_4 = -1968.5 - 4255j & k_4 = 885.53 + 266.29j. \end{cases} \tag{8.22}$$

8.2.3 Stability Analysis

Phase plane analysis is a graphical method for studying nonlinear system. It allows us to visualize what goes on in a nonlinear system without solving the nonlinear

equations analytically [91]. Fig. 8.5 shows the phase plane portraits of the closed loop voltage transfer function for both feed-forward voltage and feedback voltage controllers. While Fig. 8.6 shows the phase portraits of the closed loop current transfer function for both feed-forward voltage and feedback voltage controllers.

From these figures, it can be seen that both $f(t)$ and $\dot{f}(t)$ converge to zero

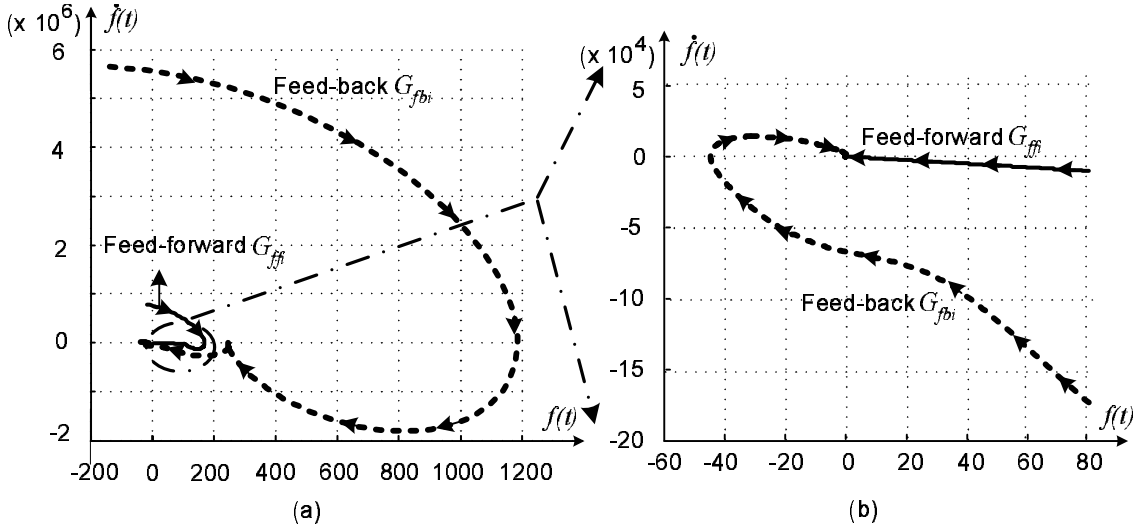

Figure 8.5: Phase portrait of feed-forward structure $G_{ffv}(t)$ and feedback structure $G_{fbv}(t)$

asymptotically, which means the system with either feed-forward voltage or feedback voltage controller is asymptotically stable. Moreover, it is noticed that the feed-forward structure follows a much shorter trajectory to reach stability than that of a feedback structure, which implies that the feed-forward structure has a much faster transient response. Hence if the system trajectory first follows the feed-forward locus till it reaches a small domain of zero, then changes over to the feedback locus, a better transient performance can be achieved .

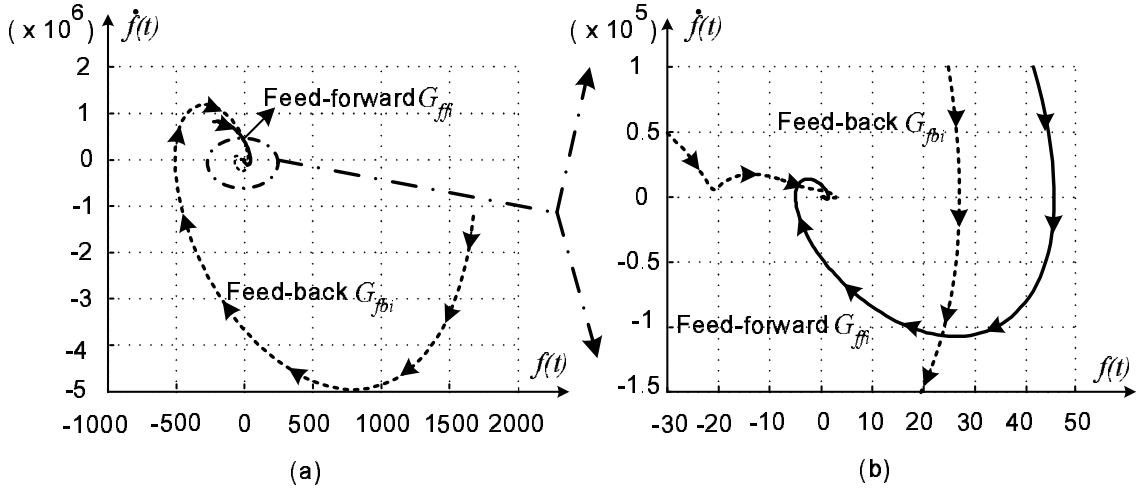

Figure 8.6: Phase portrait of feed-forward structure $G_{ffi}(t)$ and feedback structure $G_{fbi}(t)$

To further verify the stability of the combined feed-forward/feedback controller, Fig. 8.7 and Fig. 8.8 show the trajectories of state variable i_g and V_o under different operating conditions. Fig. 8.7 shows the state variable i_g when V_o is kept as $400V$ while the operating power varies from $600W$ to $1200W$. Fig. 8.8 shows the state variable i_g and V_o when V_o is regulated at different operating point from $200V$ to $400V$. To see it clearly, the waveform is normalized at maximum operating point at $V_o = 400V$ and $i_g = 50A$. From Fig. 8.7 and Fig. 8.8, it is noticed that both the feedback voltage controller and feed-forward controller are stable under different operating conditions. i_g and V_o of feed-forward structure follows much shorter trajectories and has reduced current overshoot compared to that of feedback voltage controller. But errors are observed after feed-forward voltage controller steers i_g and V_o to its final state. This error comes from the parameter deviation between the real system and the derived ideal transfer function. Since the loss of the real system cannot be anticipated

exactly, the error would be even larger in practical implementation. Fig. 8.9 gives an example of how i_g and V_o follow the trajectories of the combined feedback and feed-forward controller. The converter steps from $0W$ to $1200W$. Output voltage is regulated at $400V$ with input voltage $24V$ and duty ratio 0.76. The input current i_g first follows the feed-forward trajectory with fast transient dynamic response. It switches to feedback structure when $i_{ref1} = i_{ref2}$, where $i_g = 0.9829$ under this operating condition. After the change over, the input current i_g then follows the feedback trajectory. i_g and V_o then can be regulated both at 1, which are $50A$ and $400V$.

The trajectory difference between the ideal converter and the converter with

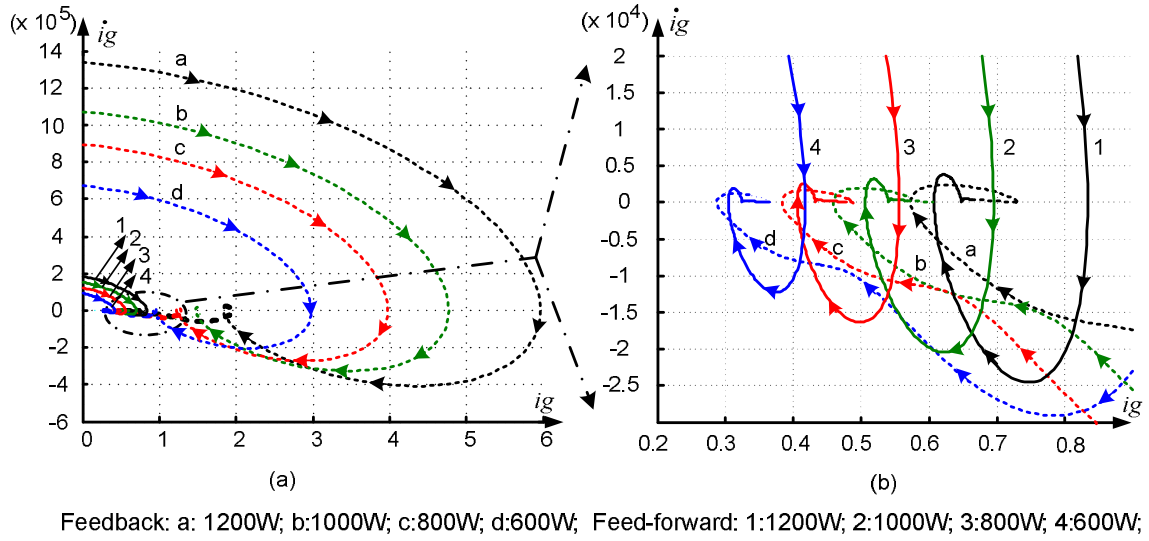

Figure 8.7: Phase portrait of state variable i_g for feed-forward and feedback structures at different power and Vo is maintained at $400V$.

parasitic resistance is shown in Fig. 8.10. It is noticed that feedback structure with parasitic resistance follows a slightly shorter locus compared to the ideal feedback

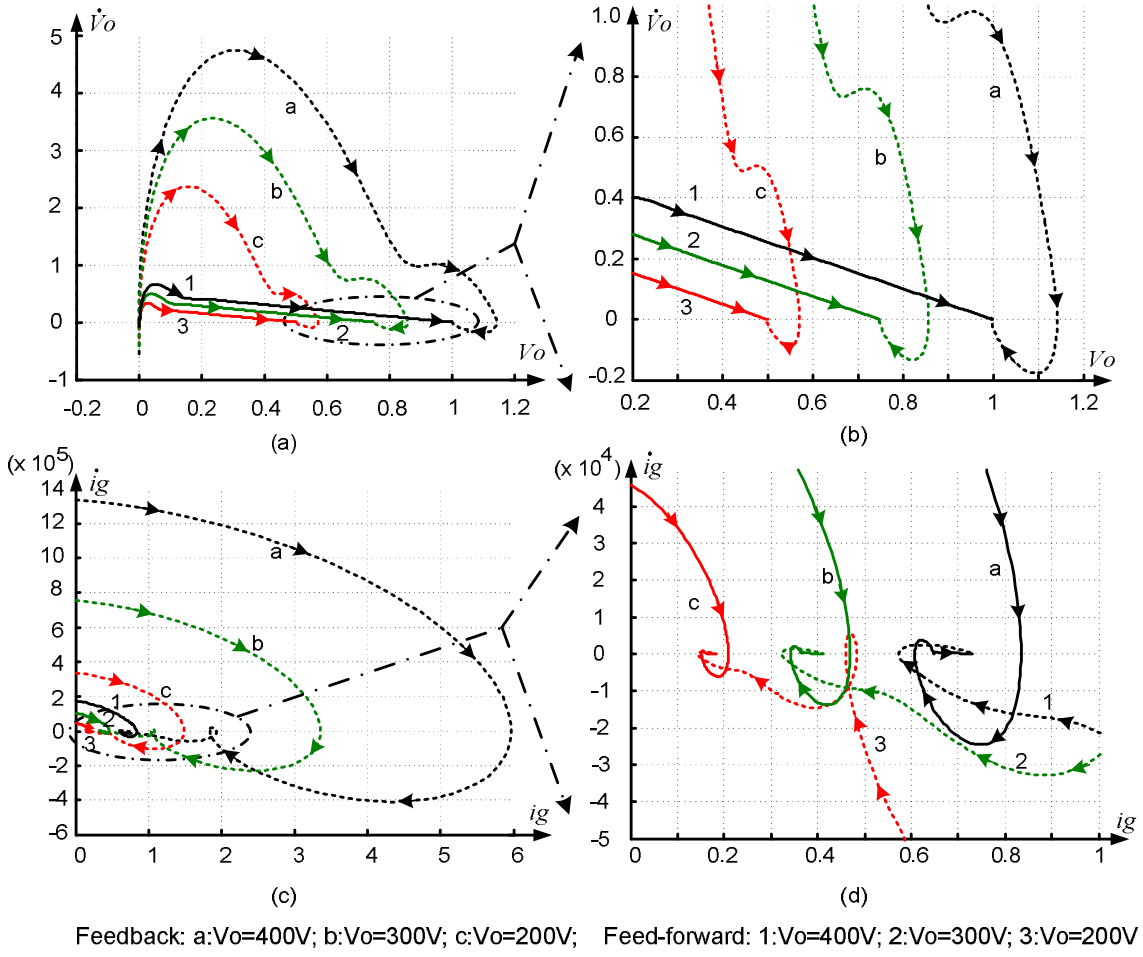

Figure 8.8: Phase portrait of state variable i_g and V_o for feed-forward and feedback structures at different output voltage. (a)(b) Phase portrait of state variable V_o; (c)(d) Phase portrait of state variable i_g.

structure, but the voltage difference diminishes as the trajectories settle to stable operating point. However for feed-forward structure, there is no evident difference between the ideal one and the non-ideal one. But the voltage error becomes evident for the trajectory with parasitic inductance when it reaches stable operating point. This is a proof to show that feed-forward structure lacks accurate self-regulation under different operating conditions.

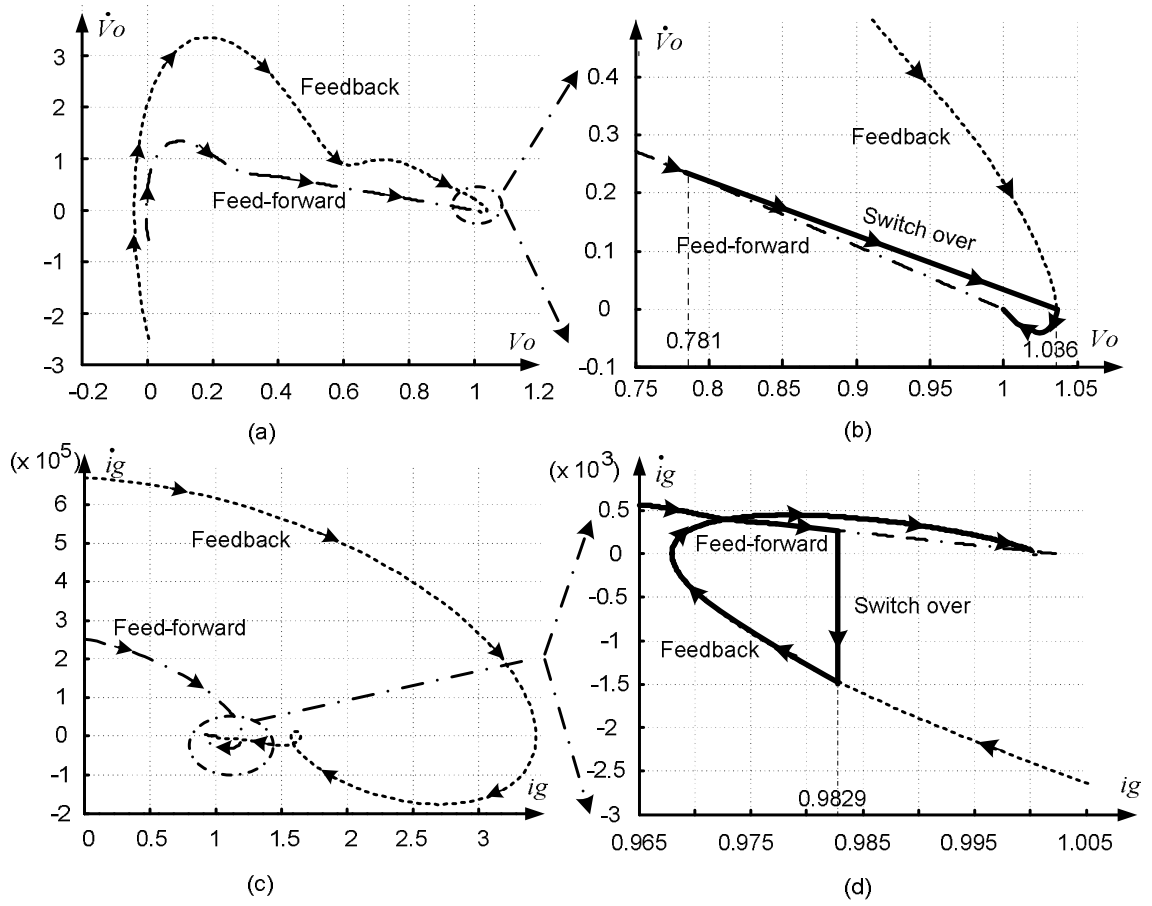

Figure 8.9: Actual trajectory of state variable i_g and V_o when power steps from $0W$ to $1200W$ using the combined feedback and feed-forward controller ($V_o = 400V$, $V_g = 24V$, $D = 0.76$). (a)(b) Phase portrait of state variable V_o; (c)(d) Phase portrait of state variable i_g.

8.3 Changeover of the Combined Feed-forward/Feedback Controller

In earlier sections, the asymptotical stability of individual structure is shown and the advantages and disadvantages of individual structure is studied in the controller. To make fully use of the advantages of these two structures, a proper strategy should

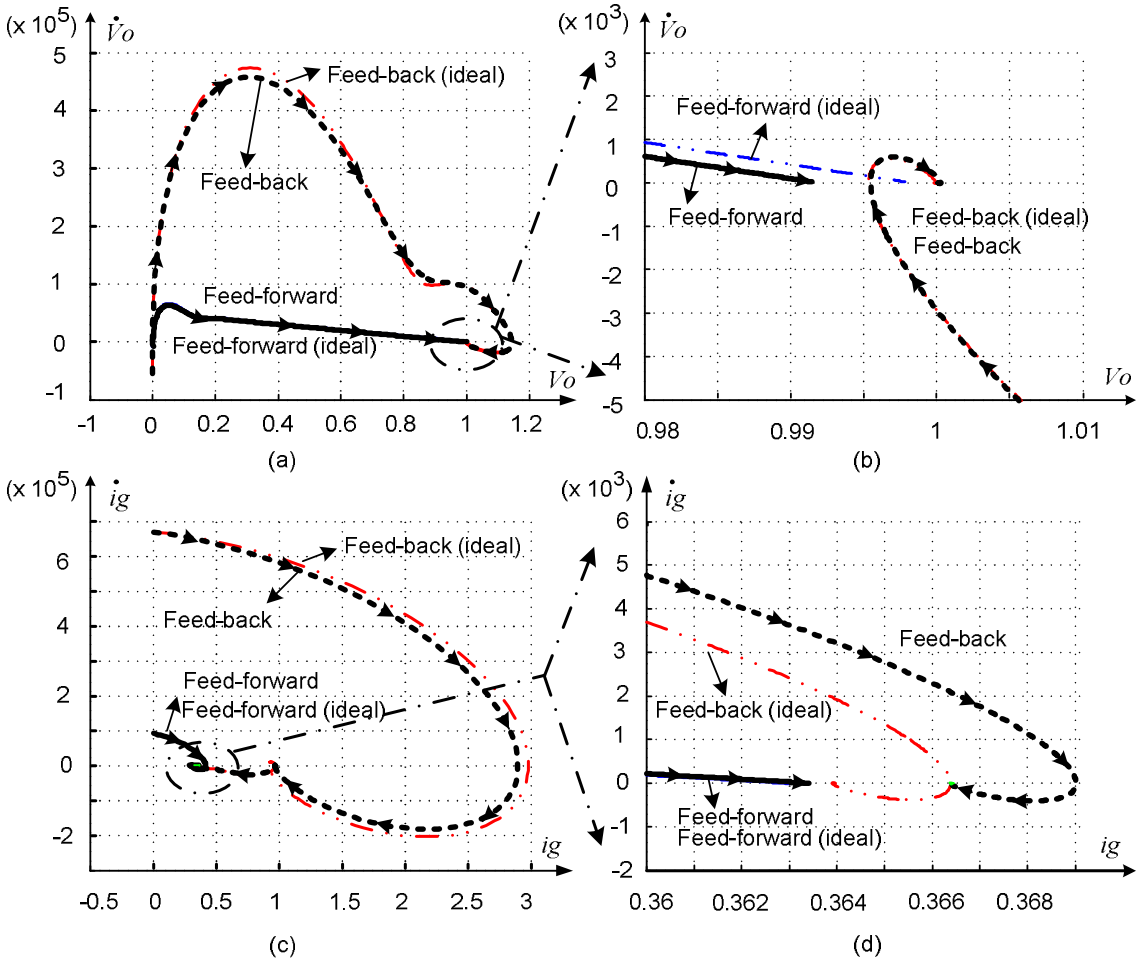

Figure 8.10: Phase portrait of state variable i_g and V_o for feed-forward and feedback structures with parasitic resistance. (a)(b) Phase portrait of state variable V_o; (c)(d) Phase portrait of state variable i_g.

be considered to change over between the two structures. Fig. 8.11 gives the general description of the change over condition between theses two structures. It depends on the direction of load changes. Detailed explanation of the strategy is to be presented in the following sections. Flowchart of the switching strategy is shown in Fig. 8.19 (please refer to the rear part of this chapter).

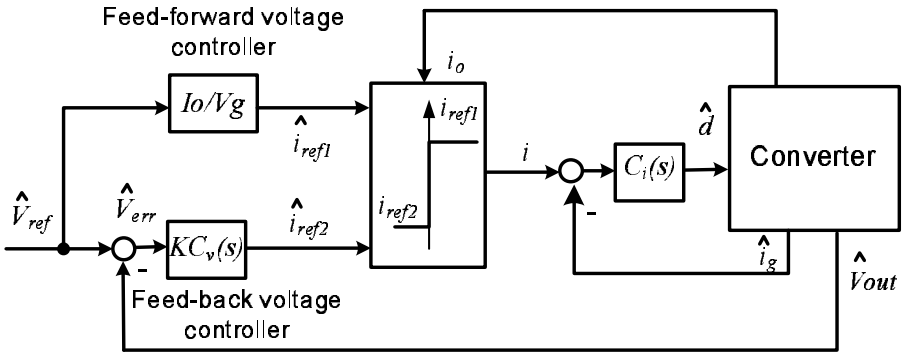

$$i = \begin{cases} \hat{i}_{ref1} & (\hat{i}_{ref1} > \hat{i}_{ref2}) \,\&\, (\dfrac{\mathrm{di_o}}{dt} > 0) \\ \hat{i}_{ref2} & (\hat{i}_{ref1} \le \hat{i}_{ref2}) \,\&\, (\dfrac{\mathrm{di_o}}{dt} > 0) \\ \hat{i}_{ref1} & (\hat{V}_{err} > \delta) \,\&\, (\dfrac{\mathrm{di_o}}{dt} < 0) \\ \hat{i}_{ref2} & (\hat{V}_{err} \le \delta) \,\&\, (\dfrac{\mathrm{di_o}}{dt} < 0) \end{cases}$$

Figure 8.11: Change over condition between feed-forward and feedback structures

8.3.1 Load Step Up

Fig. 8.12 (a)∼(i) explains the strategy to change over between feed-forward and feedback structures during load step up. Fig. 8.12 (a)∼(b) shows the waveforms of input current i_{ff} and output voltage V_{ff} when only feed-forward voltage controller is activated. Due to its fast response, i_{ff} is quickly steered to its steady-state I_{ref1} and the undershoot of V_{ff} is small. It should be noticed that I_{ref1} is calculated based on an ideal condition when converter efficiency is 100%. However in practice, power loss always exists and the required current reference I_{ref2} should always be greater than I_{ref1}. That is why output voltage V_{ff} cannot be steered to its operating point

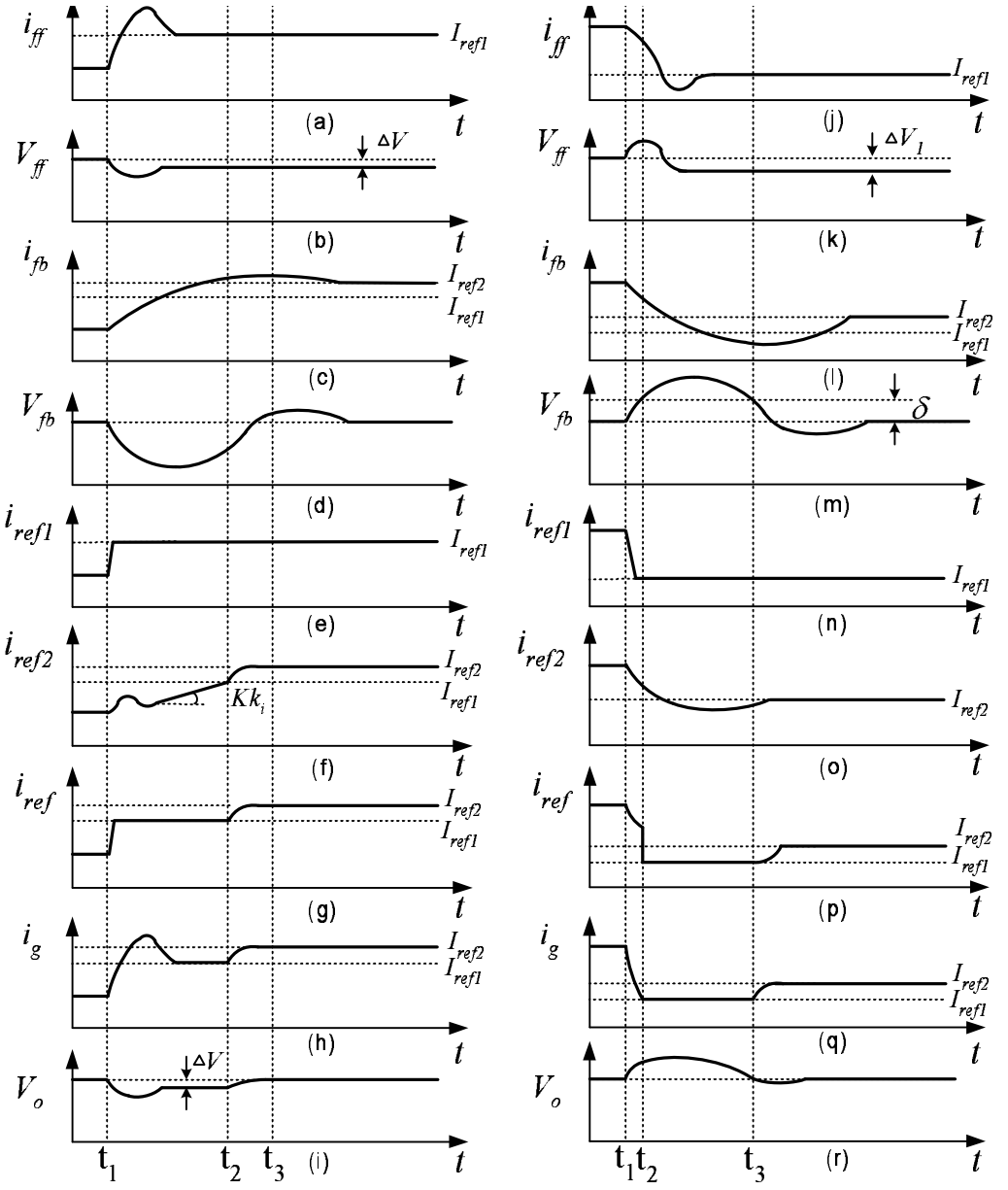

Figure 8.12: Main waveforms of the strategy to change over the structures in the combined feed-forward/feedback controller (a)∼(i) strategy during load step up; (j)∼(r) strategy during load step down

and there exists an error ΔV, as shown in Fig. 8.12 (b). Fig. 8.12 (c)∼(d) shows the waveforms of input current i_{fb} and V_{fb} when only feedback voltage controller is activated. Due to the compensation of voltage error, i_{fb} can be regulated at I_{ref2} and

V_{fb} is regulated back to its operating point without error. Since it takes some time for i_{fb} to settle down, large undershoot of V_{fb} is observed, as shown in Fig. 8.12 (d).

In order to switch between these two structures, current references i_{ref1} and i_{ref2} generated from the two structures are shown in Fig. 8.12 (e)$\sim$(f) and the combined current reference i_{ref} is shown in Fig. 8.12 (g). Also, the waveforms of input current i_g and output voltage V_o with combined feed-forward/feedback controller are shown in Fig. 8.12 (h)$\sim$(i). Strategy to switch the structures is:

1. At $\mathbf{t_1}$, load is stepped up. Immediately the feed-forward structure is activated and it generates current reference at i_{ref1}. Hence i_{ref} is the same as i_{ref1} after t_1. i_g follows i_{ref1} until it settles at I_{ref1}, as shown in Fig. 8.12 (h). Similarly, V_o settles down with a small undershoot after t_1 due to the fast response of i_g, and voltage error becomes almost a constant ΔV, see Fig. 8.12 (i). Since the current reference from feedback structure i_{ref2} can be estimated as an integration of the output voltage error, i_{ref2} begins to increase almost linearly with a slope of Kk_i, as shown in Fig. 8.12 (f). Where k_i is the integration part of $C_v(s)$ (Fig. 8.2) and K is the adjustable parameter as mentioned in Eq. 8.15.

2. At $\mathbf{t_2}$, when i_{ref2} reaches I_{ref1}, i_{ref} is changed from the output of feed-forward structure i_{ref1} to the output of feedback structure i_{ref2}. Due to the PI compensation in the feedback structure and the small voltage error, i_g is quickly regulated at I_{ref2} and the output voltage V_o is regulated back to its operating point without any error.

3. At $\mathbf{t_3}$, the converter settles down to the new steady-state at $i_g = I_{ref2}$.

8.3.2 Load Step down

Fig. 8.12 (j)∼(r) describes the strategy to change over between feed-forward and feedback structures during load step down. Fig. 8.12 (j)∼(k) shows the waveforms of input current i_{ff} and output voltage V_{ff} when only feed-forward voltage controller is activated. i_{ff} is quickly steered to its steady-state I_{ref1} and the overshoot of V_{ff} is small. Similar to load step up, there exists voltage error ΔV_1, as shown in Fig. 8.12 (k) due to the model mismatch. Fig. 8.12 (l)∼(m) shows the waveforms of input current i_{fb} and output voltage V_{fb} when only feedback voltage controller is activated. Both i_{fb} and V_{fb} can be exactly regulated at its operating point due to the PI compensators. But large overshoot is observed and the response time is slow.

As it is noticed in Fig. 8.12 (j)∼(m), i_{ref1} decreases much faster than i_{ref2}, and its new steady-state I_{ref1} is smaller than the new stead-state I_{ref2} of i_{ref2}. If the same changeover strategy is used as for load step up, i_{ref2} becomes almost instantaneously greater than I_{ref1} after the load step down occurs. Thus the combined feed-forward/feedback controller changes from feed-forward structure to feedback structure almost immediately after the load changes. Hence the effect of the feed-forward structure is hardly effective. Therefore a different strategy should be derived for the load step down. Let us define $\Delta V = V_o - V_{ref}$. Where V_{ref} is the voltage reference and V_o is the output voltage. Feed-forward structure will be activated when $\Delta V > \delta$ and

switch to feedback structure only when $\Delta V \leq \delta$. Where $\delta > 0$.

1. At $\mathbf{t_1}$, load steps down. Since $\Delta V \leq \delta$, feedback structure is first activated. Output voltage V_o begins to overshoot until it reaches $(V_{ref} + \delta)$ at t_2, where the structure is switched to feed-forward voltage controller, as shown in Fig. 8.12 (m).

2. During $\mathbf{t_2} \sim \mathbf{t_3}$, where $\Delta V > \delta$, feed-forward structure is activated. Since the current reference during this period is i_{ref1}, which is fast and already reaches I_{ref1}, the input current i_g can quickly follow i_{ref1}. Due to the fast response of i_g, overshoot of V_o is limited, see Fig. 8.12 (r).

3. At $\mathbf{t_3}$, when again $\Delta V \leq \delta$, feedback structure is switched back again. Due to the PI compensation and the small voltage error, i_g is quickly regulated at I_{ref2} and the output voltage V_o is regulated back to its operating point without any error.

Fig. 8.13 shows the simulation result of the input current i_g and output voltage V_o with combined feed-forward/feedback controller when load steps up from $600W$ to $1200W$ and steps down from $1200W$ to $600W$. This is performed on an ICFFB converter. As a comparison, the same converter with cascaded PI controller only is also simulated and plotted as the dotted line. It is noticed that the transient response of the converter with combined feed-forward/feedback controller shows better performance than that with PI controller. During load step up, voltage undershoot

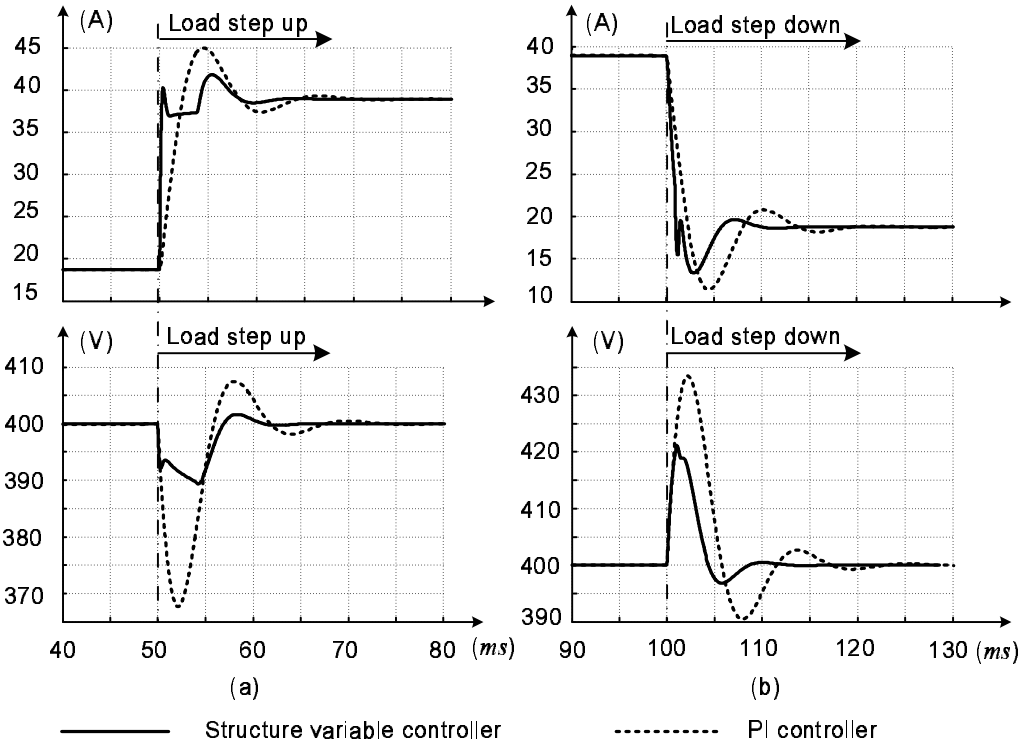

Figure 8.13: Simulation result of input current i_g, and output voltage V_o with combined feed-forward/feedback controller and PI controller (a) load steps up from $600W$ to $1200W$; (b) load steps down from $1200W$ to $600W$.

decreases from 12.5% (PI controller) to 0.25% (combined feed-forward/feedback controller) and the settling time is reduced from $20ms$ to $10ms$ (see Fig. 8.13 (a)). Moreover, voltage overshoot decreased from 19% to 15% during load step down as shown in Fig. 8.13 (b).

Fig. 8.14 compares the step response of the converter with PI controller and the proposed combined feed-forward/feedback controller using Matlab Simulink. It is noticed that there is around $10V$ initial voltage dip with the PI controller, while the initial voltage dip disappears when a combined feed-forward/feedback controller is used. However it must be noticed that the RHP zero is not physically removed

but only transparent to the designers due to the change over strategy used in the combined feed-forward/feedback controller, where a feed-forward voltage controller is first activated.

To verify the applicability of this changeover strategy, the case when the output of

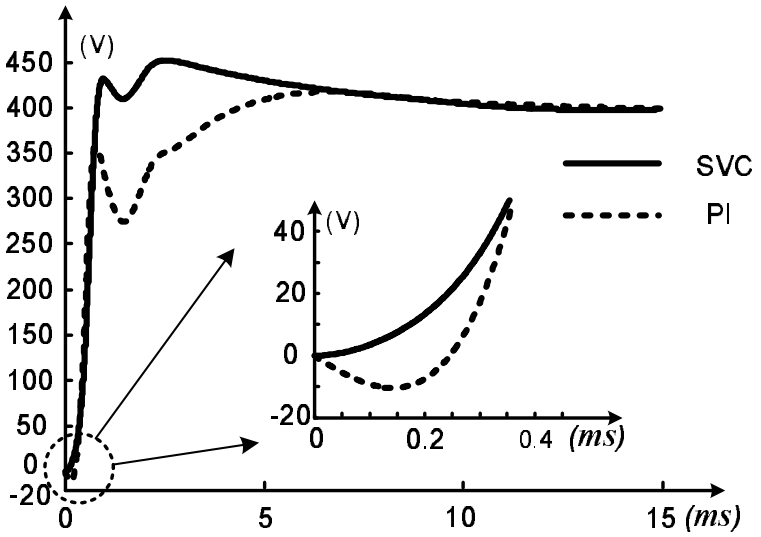

Figure 8.14: Comparison of step response of the converter with combined feed-forward/feedback controller and PI controller (Simulation)

PI oscillates in highly under-damped condition is studied. Although in proper control design, the highly under-damped controller should be avoided, it is still discussed here to study the effect of damping on the stability of the combined feed-forward/feedback controller under severe conditions. The oscillation caused by the highly under-damped controller will not affect the final stability of the system, as long as the PI controller itself is stable. But this may affect the number of switchings between the two structures. Fig. 8.15 shows the simulation result with a highly under-damped PI controller (damping ratio $\zeta = 0.2$). From this figure, it can be seen that due to the high os-

cillation, the switching occurs twice between feed-forward and feedback structures. But the peak oscillation amplitude of the combined feed-forward/feedback controller is reduced to half of that in a normal PI controller. More simulation results are performed with different damping ratios in Fig. 8.16. To ensure a good dynamic performance and allow only one switchover between the two structures, the damping ratio ζ is recommended to be $\boxed{\zeta > 0.4}$.

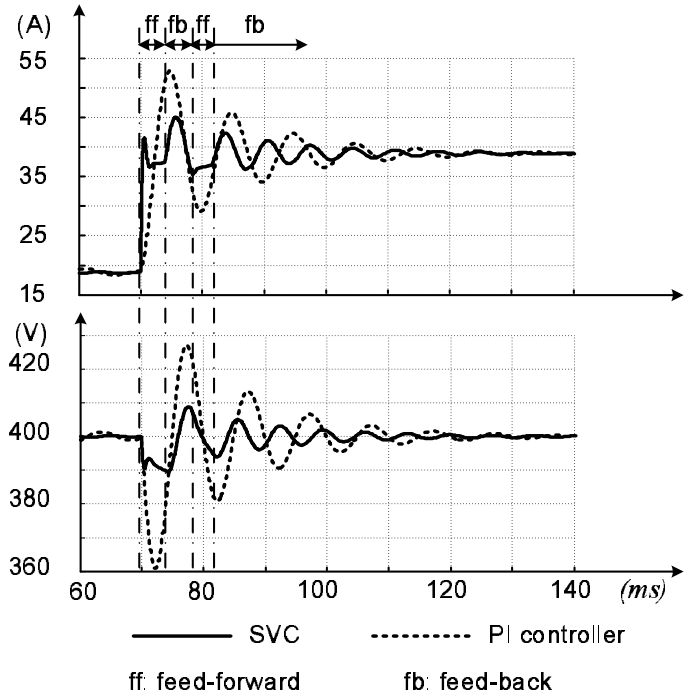

Figure 8.15: Simulation result of the combined feed-forward/feedback controller during highly under-damped condition when power steps up from $600W$ to $1200W$

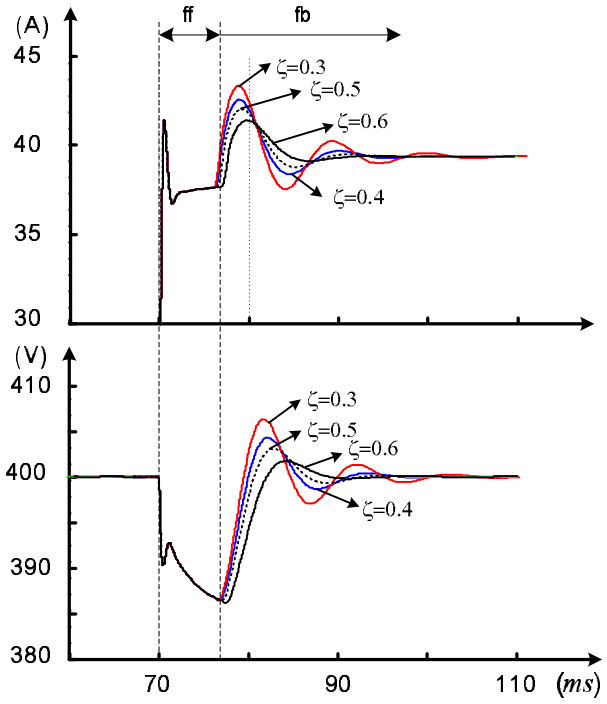

Figure 8.16: Comparison of the combined feed-forward/feedback controller with different damping ratio $\zeta = 0.3 \sim 0.6$ when power steps up from $600W$ to $1200W$ (simulation)

8.4 Experimental Results

A $1.2kW$ ICFFB converter is built with the circuit specifications listed in Table 8.2.

The dSPACE 1104 controller system is used to implement PWM functions and closed loop control. The system consists of a floating point DSP TMS320C31, a DSP-microcontroller TMS320P14 based digital I/O subsystem, A/D and D/A converters. Since this controller system is specifically designed for the development of multivariable digital controllers and real-time simulations in various fields, it would be much helpful to control the whole system when all subsystems (fuel cell, DC/DC convert-

Table 8.2: Converter specification

Switching frequency	$f_s = 10kHz$
Maximal output power	$1200W$
Switches	IXFK90N20 MOSFETs, $R_{DS(ON)} = 40m\Omega(100^oC)$
Diodes	$4\times$Ultra fast MUR860 $8A/600V$
Output capacitors	$100\mu F$,$200V$ Electrolytic + $0.027\mu F$ polyester
Snubber capacitors	$0.44\mu F$ polyester
Input inductors	$E305-26$, Iron powder core L_1: $180.0\mu H$, $r_1 = 55.2m\Omega$, L_2: $179.6\mu H$, $r_2 = 54.6m\Omega$
Transformers	$EC70$, Ferrite core$-3C90$, $n_1/n_2 = 1:2$ $L_m = 1.19mH$, leakage inductance $L_k = 3.16\mu H$

ers, inverters, energy control) are built up into one in future. As it is known, four gate signals with 90^o phase shift are necessary to control the converter. However in a standard dSPACE firmware, there is no such functions to define a specific phase shift among the PWM generators. To modify the standard firmware is one option, but it requires specific knowledge and experience in this particular field. Hence, to simplify the problem, a Field Programmable Gate Array (FPGA) board Spartan III is used to shift the gate signals. Block diagram for the realization of the controller is shown in Fig. 8.17. D_1 or D_2 is the duty ratio for each module of the interleaved converter. $PWM1$ and $PWM2$ are gate signals produced from PWM generator and there is

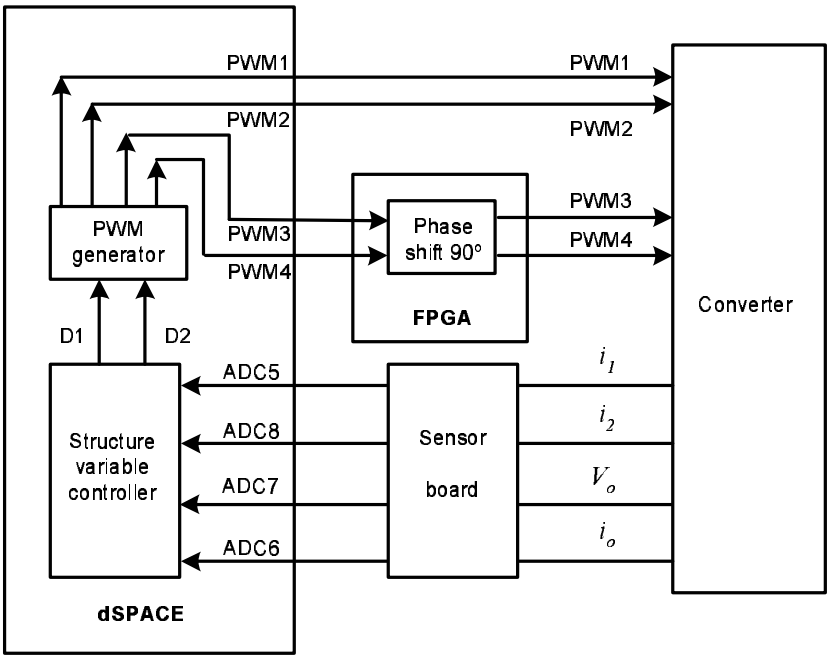

Figure 8.17: Block diagram for controller implementation with dSPACE and FPGA board

180^o phase shift between $PWM1$ and $PWM2$. $PWM3$ and $PWM4$ are delayed in phase by 90^o with respect to $PWM1$ and $PWM2$ via the FPGA board. Inductor currents i_1 and i_2, output voltage V_o and load current i_o are sensed and converted to digital signals.

Since the ICFFB converter consists of two identical CFFB converters, it is easy to verify the analysis by testing one CFFB converter only. Combined feed-forward/feedback controller is programmed in real-time simulink. The dSPACE's realtime interface (RTI) is used to link between the dSPACE' realtime hardware and the MATLAB/Simulink development software. It extends the C code generator realtime workshop so that the simulink models can be implemented very easily on dSPACE realtime hard-

ware. Fig. 8.18 shows the experimental result by implementing the combined feed-forward/feedback controller and the cascaded PI controller on one CFFB converter. Fig. 8.18 (a) (b) shows the transient response when the CFFB converter steps

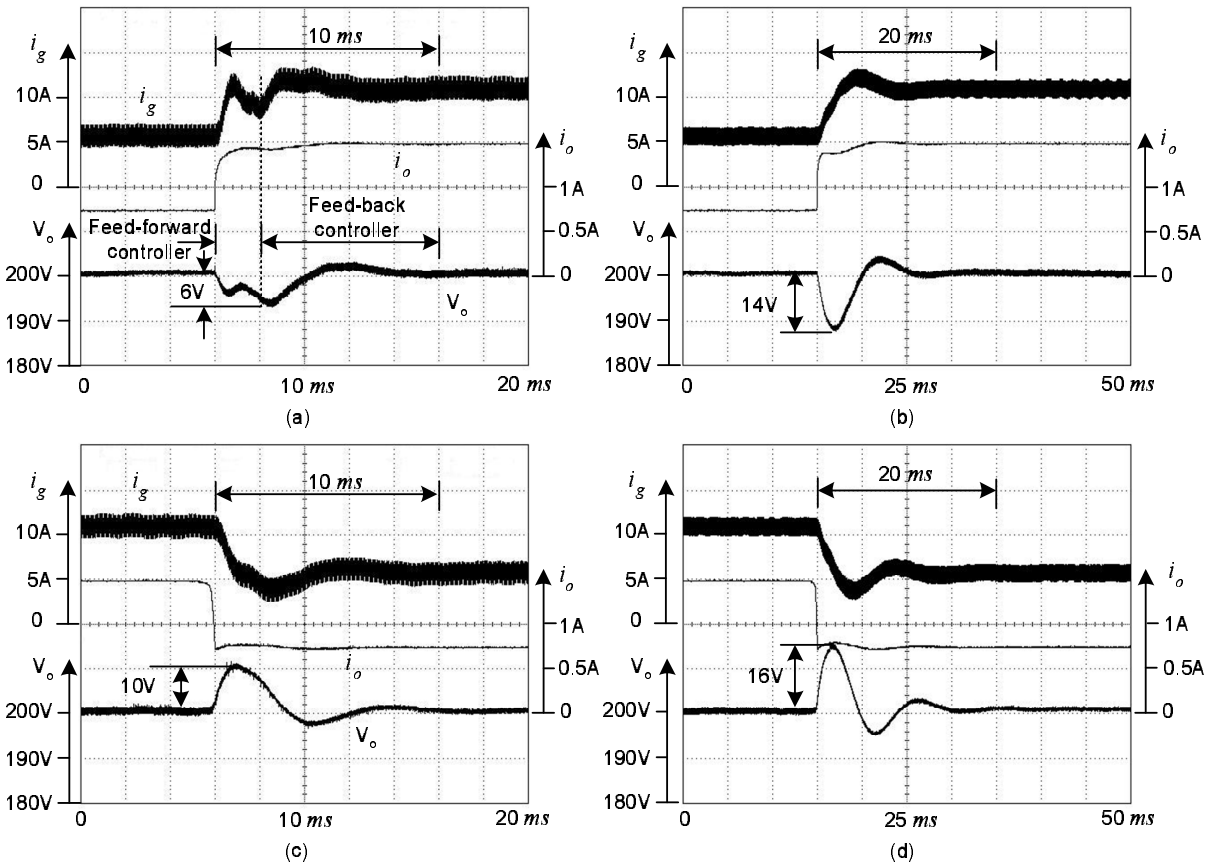

Figure 8.18: Comparison of experimental result of input current i_g , output current i_o and output voltage V_o with combined feed-forward/feedback controller and PI controller (a) load step up with combined feed-forward/feedback controller from $150W$ to $300W$; (b) load step up with PI controller from $150W$ to $300W$; (c) load step down with combined feed-forward/feedback controller from $300W$ to $150W$; (d) load step down with PI controller from $300W$ to $150W$

up from $150W$ to $300W$. It can be seen that voltage undershoot with combined feed-forward/feedback controller (Fig. 8.18 (a)) is only 3% compared to 7% of that with the PI controller (Fig. 8.18 (b)). Moreover, settling time with combined feed-

forward/feedback controller is only $10ms$, which is much faster than that with PI controller. Similarly, Fig. 8.18 (c) (d) shows the transient response when the converter steps down from $300W$ to $150W$. Voltage overshoot is reduced to 5% for combined feed-forward/feedback controller (Fig. 8.18 (c)) compared to 8% with PI controller (Fig. 8.18 (d)). The experimental results clearly verified the improvement of the response performance by using the combined feed-forward/feedback controller. It is not only faster, but also effectively reduces the undershoot/overshoot of the output voltage.

8.5 Summary

A combined feed-forward/feedback controller is proposed in this Chapter to minimize the RHP zero effect by "shaping" the trajectory of the minimum phase variable–input current. To "shape" the trajectory of the input current, current references generated from two different controller structures are changed over under certain criteria. Feed-forward structure has a faster response and smaller voltage undershoot/overshoot, but lacks accurate regulation of the control variables. While feedback structure can achieve precise regulation of control variables, but it is slow and has large voltage undershoot/overshoot. The combined feed-forward/feedback controller proposed in this Chapter is to take advantages of these two structures. By changing over between the feed-forward structure and feedback structures, a faster transient response can be achieved. Moreover, the voltage undershoot/overshoot is

greatly reduced.

Since there is a switching between two different control structures, the stability of the combined feed-forward/feedback controller is proved through the phase plane analysis. Moreover, the criteria of when and how to change over the structures is also derived and described. To verify the validity of the combined feed-forward/feedback controller, a $1.2kW$ ICFFB converter is built. All PWM signals, closed loop controller are implemented via a dSPACE 1104 system. Experimental result shows that the voltage undershoot is reduced to 3% with the combined feed-forward/feedback controller compared to 7% with a conventional PI controller. Furthermore, settling time of the combined feed-forward/feedback controller ($10ms$) is faster compared to $20ms$ of the PI controller.

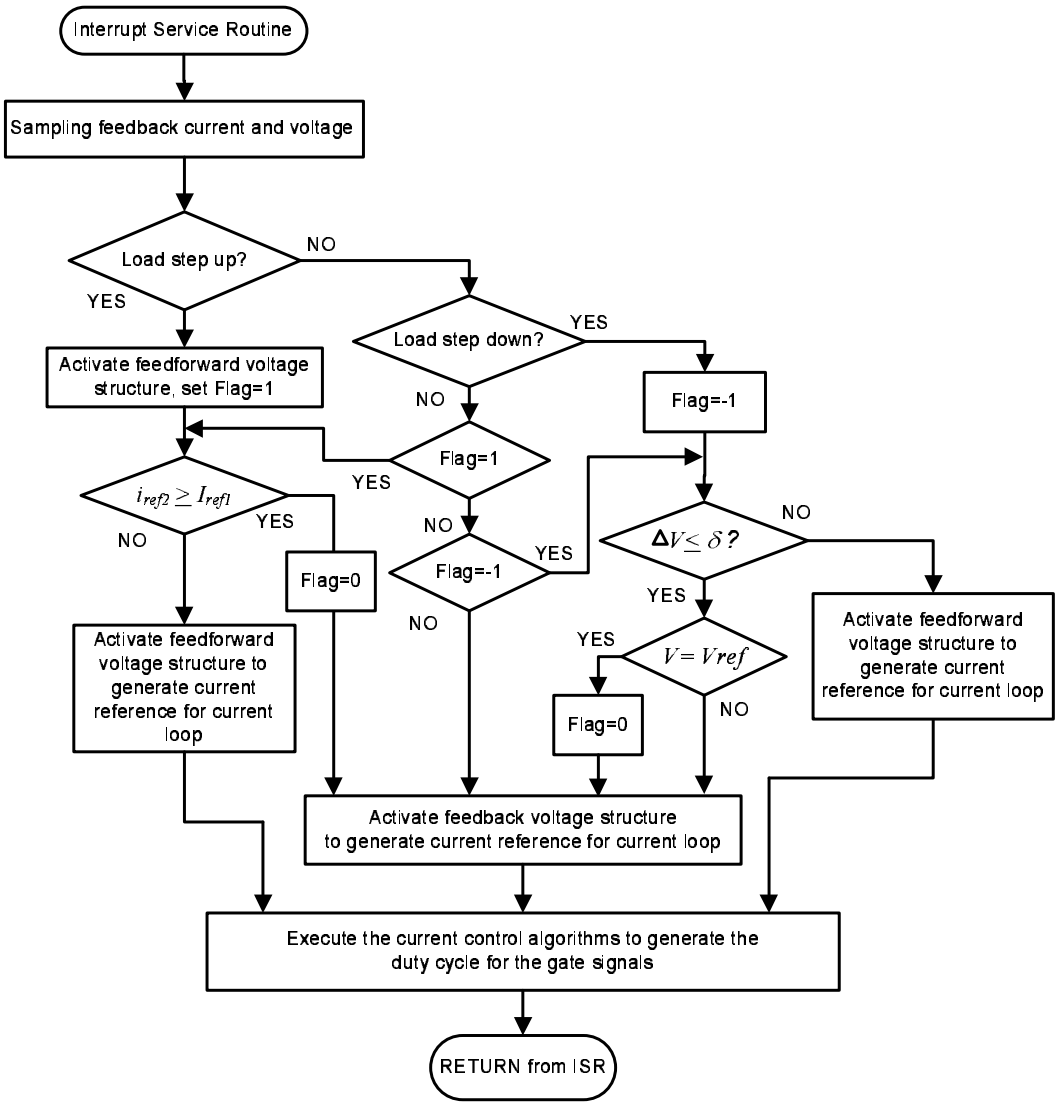

Figure 8.19: Flow chart for changeover strategy of combined feed-forward/feedback controller

Chapter 9

Conclusions and Future Work

Two issues are studied in this thesis: fuel cell stack modelling, design and control of DC/DC converters. They are presented as two parts in the thesis. In this chapter, results of the research work are first summarized, and then future works are suggested.

9.1 Summary of Results

Part I Fuel Cell Stack Modelling

- Chapter 3 of the thesis describes a simple and accurate fuel cell stack model suitable for electrical engineers. With the combination of an empirical stack model, an electrical circuit stack model and temperature effect, this hybrid fuel cell stack model is capable of characterizing fuel cell stack's steady state performance as well as transient behavior. Compared to those analytical fuel

cell models [7] [8] [9], the proposed hybrid model has no comprehensive mathematics. Unlike the normal empirical models [15] [16] [17], the proposed hybrid model includes charge double layer dynamics and regulates its "RC" parameters according to various operating point. At the same time, temperature effect on the fuel cell is simulated as the modification of fuel cell internal resistance according to temperature variation. Identification of model parameters is derived and obtained from experimental results. To verify the model validity, a $1.2kW$ PEMFC stack from Ballard $Nexa^{TM}$ is used as the test-bench. The correlation between the hybrid model and the experimental data during steady-state are shown in Fig. 3.13. More than 97% accuracy is achieved during all load range, which is a good proof of the model accuracy in evaluating the steady-state performance of the fuel cell stack. Similarly, Fig. 3.11 shows a very good correlation between the hybrid model and the experimental data to a short period of load insertion or extraction. It is also verified from Fig. 3.11 that charge double layer dynamics is dominant due to the negligible temperature effect during the short period of load insertion/rejection. However when temperature effect becomes dominant during large period of load insertion and extraction, about 93% accuracy can be obtained between the model and the experiment for most transient responses, as shown in Fig. 3.12. Also, it is noticed that a maximum error of $2V$ appears in Fig. 3.12 (c) and (d), which is mainly caused by the approximation of temperature dependant internal resistance. From all these

experimental results, the hybrid model is verified to be capable of evaluating both the steady-state and dynamic performance of a fuel cell stack with a good accuracy of above 93%. The accuracy can be further improved with a neural network described in Chapter 4. Although the model is designed for a specific stack, design procedure and instructions for model parameter identification can be followed and applied to other PEMFC stacks too.

- In Chapter 4, an ANN PEM fuel cell stack model is described and implemented in real-time. The aim of this ANN approach is to improve the dynamic accuracy and flexibility of the model by modelling the nonlinear behavior of the hybrid model proposed in Chapter 3. It has been explained that linear approximation of the nonlinear model parameters results in the errors during some of the large period of load insertions/extractions. Two ANN blocks are brought in the hybrid model. One is designed to obtain the nonlinear fuel cell internal resistance. The other one is to map the relationship between fuel cell current and temperature, which finally represents the temperature effect on the stack as fuel cell current effect by sensing fuel cell current via an ANN block. The real-time implementation of the ANN model is based on a $1.2kW$ PEMFC stack from Ballard $Nexa^{TM}$ and a real-time processor dSPACE-1104. The experimental results have shown that the ANN model has a higher accuracy than the hybrid model, as shown in Fig. 4.6. The maximum voltage error has been improved from $2V$ to $0.5V$ and the Mean Squared Error of the ANN model has been

reduced to about 20% of that in a hybrid model. Moreover, as shown in Fig. 4.7, Fig. 4.9 and Fig. 4.11, with load steps outside the training set, a good correlation is also observed between the ANN model and the experimental data, which proves the flexibility of the ANN model dealing with different load steps.

Part II DC/DC Converters

- In Chapter 6, an isolated current-fed full bridge converter (CFFB) is proposed with a voltage doubler on the secondary side. Compared to [32] [48] [54], this CFFB converter has inherent high boost ratio and direct control of fuel cell current. While compared to [31] [65] [71], the CFFB converter is a better candidate for high power level. Detailed circuit analysis has been performed and has shown that voltage conversion ratio of CFFB is twice of that in a conventional current-fed full bridge converter. With the design of a dual loop controller, the output voltage and input current of the CFFB converter can both be controlled. A $1.2kW$ CFFB converter is set up and controlled via a digital signal processor DSP TMS320F. About 8% input current ripple and 89% efficiency have been achieved at the full power rating, as shown in Fig. 6.13 and Fig. 6.14. Regulation of output voltage can be realized in about 35 ms during the load insertion/extraction, as indicated in Fig. 6.15. Although the CFFB converter is a good candidate for high power fuel cell based supplies, its inherent problems of the current-fed full bridge converters have not been solved. The

high current inductor and large inrush current during start-up have hindered further application of this kind of converter topology.

- To solve the remaining problems of the CFFB converter in Chapter 6, an interleaved current-fed full bridge converter (ICFFB) is proposed in Chapter 7. Due to its parallel input/series output scheme, input current and power are equally shared between the modules of the converter system, hence small current-stress semiconductor devices on the input side can be used. Moreover, the series connection on the output side results in lower voltage ratings for output capacitors and diodes. On the other hand, the effective frequency of the ICFFB converter is four times of the switching frequency due to the interleaving of the converter modules, which again helps reduce the size of magnetic components in the circuit. Experimental results on a $1.2kW$ ICFFB converter with the DSP controller have shown that input current ripple is reduced to 5% and the total core volume and weight of magnetic components are reduced by 50%, see Fig. 7.11 and Table 7.3. Moreover, about 90.5% efficiency is obtained at full power and the dynamic response of the ICFFB converter is about 20 ms, as shown in Fig. 7.12 and Fig. 7.13.

- Another contribution of Chapter 7 is the proposed soft start-up method. Compared to [77] [78], where a thermistor or a resistor is used to limit the inrush current, the proposed method is more efficient. On the other hand, there is no

complex additional circuits added as compared to [80]. Strategy to start up the circuit is to suppress the high inrush current by establishing an initial output voltage before the converter operates in normal boost mode. All the process is realized through the proper control of the switches via the software. As the experimental waveforms shown in Fig. 7.19, the proposed ICFFB converter starts without high inrush current and the output voltage slowly reaches $400V$. Based on high efficiency, smaller magnetic components, reduced input current ripple and soft start-up capability, this ICFFB converter seems to be quite suitable for a high power fuel cell system.

- In Chapter 8, a combined feed-forward/feedback controller is proposed to improve the dynamic performance of the boost-type converters by "shaping" the trajectory of the minimum phase variable–input current. To fully use the advantages of feed-forward and feedback voltage controllers, the trajectory of the input current reference is generated from two different controller structures and changed over under certain criteria. In doing so, a fast transient response and small voltage undershoot/overshoot can be achieved. The stability of this structure variable controller is proved through phase plane analysis. Criteria of when and how to change over the structures are derived and analyzed. Compared to the normal current controller designed in the previous chapters, the structure variable controller is faster and has reduced voltage sag/overshoot. This is verified from both simulation and experimental results. Fig. 8.18 clearly

indicates that the voltage undershoot is reduced to 3% with the combined feed-forward/feedback controller compared to 7% with a conventional PI controller. Furthermore, settling time with the combined feed-forward/feedback controller ($10ms$) is faster compared to $20ms$ of the PI controller.

9.2 Future Works

There are several directions for future work in the area of the research presented in the thesis.

- Fuel cell simulator

  Fuel cell modelling is an effective way to understand fuel cell characteristics. To extend its application from simulation to connection with power electronic circuit, a real fuel cell stack should be used. However the cost of a real fuel cell stack is usually expensive for research and development activities. Auxiliary equipment like hydrogen storage and safety standards also have to be taken into considerations. To avoid this problem, a flexible fuel cell simulator can play an important role in assisting and developing a fuel cell power electronic circuit.

  Several approaches to fuel cell simulators were published. A method was proposed by Drolia to emulate steady-state and dynamic characteristics of a fuel cell using DSP controlled buck converter [92]. A real-time fuel cell model is

run on a DSP, which provides the control signal to a switched mode power converter. The converter amplifies the control signal to the required voltage and thus emulates the steady-state and dynamic characteristics of the fuel cell model running in the DSP. Although the approach was novel, the experimental results with the fuel cell simulator was only verified by simulation. Another fuel cell simulator was proposed later in [93]. The highly nonlinear V-I curve of the fuel cell is achieved using buck converter. By sensing the output current of the simulator, different voltage reference is generated according to different load region (activation region, ohmic region and concentration region). The simulator was built as a part of a fuel cell generation system and the experimental results were verified by the simulation results. However, the so called nonlinear polarization curve is actually linear in each region. The activation region and the concentration region were actually simplified as constants. This may not be able to reproduce the behavior of the fuel cell properly. Authors in [94] developed a PSpice model which incorporated steady-state thermal effect. Although the model was only simulated in computer, it would be very easy to be implemented in real-circuit as a fuel cell simulator. A novel fuel cell simulator was proposed by controlling a near time optimal Switching Mode Power Supply (SMPS) [95] . Reference signal for the SMPS is generated using a single fuel cell and the behavior of the single fuel cell is amplified by the SMPS to emulate the fuel cell stack. This emulator allows a complete scale evaluation of

the stack and prevents possible inaccuracies due to modelling.

Emulating a low mathematic fuel cell model is left for future investigations. The method to emulate the nonlinear V-I characteristics and the dynamic behavior of the fuel cell with a DSP controller is also an interesting field in the future work.

- Fuel cell energy management

  Fuel cells cannot store energy. In other words, fuel cell is a unidirectional power source. Hence for fuel cell powered distributed generation system or electrical vehicles, energy storage is always required as the secondary energy source. In hybrid electric vehicles, batteries and ultracapacitors can be employed to reduce the cost and improve the performance of the hybrid fuel cell system. Thus energy management becomes important to either capture the regenerative brake energy or prevent excessive power drawn from the fuel cell. The voltage level and dynamic characteristic of the energy storage are normally different from the fuel cell. Hence a bidirectional power converter is usually used to provide bidirectional power flow between the fuel cell and energy storage, which is the essential part of the energy management system.

  Some publications have been found recently in this area [96] [97] [98] [99] [100]. In [99], Jason Lai presented the significance of the bidirectional power converters in energy control and explained how to select the circuit topology for efficiency, size and cost considerations. He also pointed out that the major difficulties of

developing a high power bidirectional dc-dc converter are lack of high power passive components and lack of multiphase dc-dc controllers. A three-port bidirectional converter was proposed in [98] for a hybrid fuel cell system. Three H-bridge modules are coupled by means of a three-winding transformer, with the addition of external inductors. The power flow was controlled by shifting the switching patterns with respect to the fuel cell module. While in [97], a novel energy management method was proposed to control a three-level bidirectional converter. The converter is controlled to operate under different modes according to the battery and fuel cell conditions. Totally nine modes were considered. Fig. 9.1 shows the energy management topology for future work. Ultracapacitor is selected as the energy storage. The ICFFB converter is used to boost fuel cell output voltage. While a bidirectional DC/DC converter is used to control the power flow between fuel cell stack and ultracapacitors. The challenges here are the appropriate sizing of ultracapacitors, design of the bidirectional circuit and power control method between the two sources.

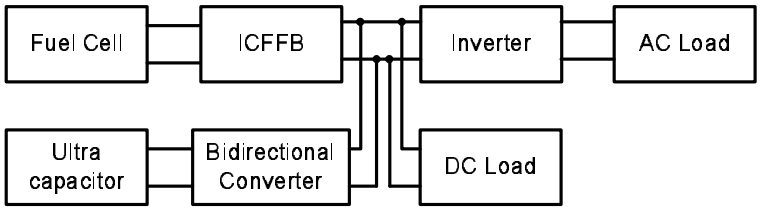

Figure 9.1: Block diagram of fuel cell and energy storage system

Bibliography

[1] M.A. Laughton, "Fuel cells," *Power Engineering Journal*, pp. 7–16, February 2002.

[2] Michael W. Ellis, Michael R. Von Spakovsky, and Douglas J. Nelson, "Fuel cell systems: Efficient, flexible energy conversion for the 21st century," *Proceedings of the IEEE*, vol. 89, pp. 1808–1818, December 2001.

[3] J.E. Larminie and Dicks, *Fuel Cell Systems Explained*, John Wiley and Sons Chichester England, 2002.

[4] Internation Energy Agency, *Hydrogen and Fuel Cells–Review of National R & D Programs*, OECD, 2004.

[5] J.C. Amphlett, R.M. Baumert, R.F. Mann, B.A. Peppley, P.R. Roberge, and J.P. Salvador, "A model predicting transient responses of proton exchange membrane fuel cells," *Journal of Power Sources*, vol. 142, pp. 9–15, 1995.

[6] Andrew Richard Balkin, "Modeling a 500W polymer electrolyte fuel cell,"

Project Report Capstone Project A02-080, University of Technology, Sydney, Jun 28 2002.

[7] T.E. Springer, T.A. Zawodzinski, and S. Gottesfeld, "Polymer electrolyte fuel cell model," *Journal of the Electrochemical Society*, vol. 138, pp. 2334–2342, 1991.

[8] T.E. Springer, M.S. Wilson, and S. Gottesfeld, "Modeling and experimental diagnostics in polymer electrolyte fuel cells," *Journal of the Electrochemical Society*, vol. 140, pp. 3513–3526, 1993.

[9] J.C. Amphlett, R.M. Baumert, R.F. Mann, B.A. Peppley, P.R. Roberge, and A. Rodrigues, "Parametric modeling of the performance of a 5kW proton exchange membrane fuel cell stack," *Journal of Power Sources*, vol. 49, pp. 349–356, 1994.

[10] J.C. Amphlett, R.M. Bumert, R.F. Mann, B.A. Peppley, and P.R. Roberge, "Performance modeling of the ballard mark IV solid polymer electrolyte fuel cell I: Mechanistic model development," *Journal of the Electrochemical Society*, vol. 142, pp. 1–8, 1995.

[11] J.C. Amphlett, R.M. Bumert, R.F. Mann, B.A. Peppley, and P.R. Roberge, "Performance modeling of the ballard mark IV solid polymer electrolyte fuel cell II: Empirical model development," *Journal of the Electrochemical Society*, vol. 142, pp. 9–15, 1995.

[12] Sukee Um, C.Y. Wang, and K.S. Chen, "Computational fluid dynamic modeling of proton exchange membrane fuel cells," *Journal of the Electrochemical Society*, vol. 147, pp. 4485–4493, 2000.

[13] J.H. Lee and T.R. Lalk, "Modeling fuel cell stack systems," *Journal of Power Sources*, vol. 73, pp. 229–241, 1998.

[14] Sampath Yerramat, Asad Davari, and Feliachi, "Dynamic modeling and analysis of polymer electrolyte fuel cell," *Power Engineering Society Summer Meeting IEEE*, vol. 1, pp. 21–25, 2002.

[15] Junbom Kim, Seong Min Lee, Supramaniam Srinivasan, and Charles E.Chamberlin, "Modeling of proton exchange membrane fuel cell performance with an empirical equation," *Journal of the Electrochemical Society*, vol. 142, pp. 2670–2674, 1995.

[16] S. Busquet, C.E. HUbert, J. Labbé, D. Mayer, and R. Metkemeijer, "A new approach to empirical electrical modelling of a fuel cell, an electrolyser or a regenerative fuel cell," *Journal of Power Sources*, vol. 134, pp. 41 – 48, July 2004.

[17] Deryn Chu and Rongzhong Jiang, "Performance of polymer electrolyte membrane fuel cell (PEMFC) stacks part I: Evaluation and simulation of an air-breathing PEMFC stack," *Journal of Power Sources*, vol. 83, pp. 128–133, 1999.

[18] S. Jemeï, D. Hissel, M.C. Péra, and J.M. Kauffmann, "Black-box modeling of proton exchange membrane fuel cell generators," in *The 28th Annual Conference of the IEEE Industial Electronic Society, IECON 2002*, 5-8 November 2002, pp. 1474 – 1478.

[19] Christof Nitsche, Stefan Schroedl, and Wolfgang Weiss, "Onboard diagnostics concept for fuel cell vehicles using adaptive modelling," in *2004 IEEE Intelligent Vehicles Symposium*, 14-17 June 2004, pp. 127 – 132.

[20] Jay T. Pukrushpan, Anna G. Stefanopoulou, and Huei Peng, *Control of Fuel Cell Power Systems-principles, modeling, analysis and feedback design*, Springer, 2004.

[21] Elmar Achenbach, "Response of a solid oxide fuel cell to load change," *Journal of Power Sources*, vol. 57, pp. 105–109, 1995.

[22] J.C. Amphlet, Erick H. de Oliverira, Ronald F. Mann, and Pierre R. Roberge, "Dynamic interaction of a proton exchange membrane fuel cell and a lead-acid battery," *Journal of Power Source*, vol. 65, pp. 173–178, 1997.

[23] Jammes Garnier, M.C. Pera, D. Hissel, F. Harel, D. Candusso, N. Glandut, J.P. Diard, A. De Bernardinis, J.M. Kauffmann, and G. Coquery, "Dynamic pem fuel cell modeling for automotive applications," in *Vehicular Technology Conference, 2003, VTC 2003-Fall, 2003 IEEE 58th*, 6-9 Oct. 2003, pp. 3284 – 3288.

[24] Sandip Pasricha and Steven R. Shaw, "A dynamic pem fuel cell model," *IEEE Transactions on Energy Conversion*, vol. 21, pp. 484 – 490, June 2006.

[25] C. Wang, M.H. Nehrir, and H. Gao, "Control of pem fuel cell distributed generation systems," *IEEE Transactions on Energy Conversion*, vol. 21, pp. 586 – 595, June 2006.

[26] J.M. Corrêa, F.A. Farret, and L.N. Canha, "An analysis of the dynamic performance of proton exchange membrane fuel cells using an electrochemical model," in *Industrial Electronics Society, 2001. IECON '01. The 27th Annual Conference of the IEEE*, Nov 29 - Dec 2 2001, vol. 1, pp. 1147–1150.

[27] J.M. Corrêa, F.A. Farret, L.N. Canha, and M.G. Sim oes, "An electrochemical-based fuel-cell model suitable for electrical engineering automation approach," *IEEE Transactions on Industrial Electronics*, vol. 51, pp. 1103 – 1112, October 2004.

[28] M. Ceraolo, C. Miulli, and A. Pozio, "Modelling static and dynamic behavior of proton exchange membrane fuel cells on the basis of electro-chemical description," *Journal of Power Sources*, vol. 113, pp. 131–144, February 2003.

[29] Kourosh Sedghisigarchi and Ali Feliachi, "Dynamic and transient analysis of power distribution systems with fuel cells-part I: Fuel cell dynamic model," *IEEE Transactions on Energy Conversion*, vol. 19, pp. 423–428, June 2004.

[30] P.R. Pathapati, X. Xue, and J. Tang, "A new dynamic model for predicting transient phenomena in a PEM fuel cell system," *Renewable Energy*, vol. 30, pp. 1–22, January 2005.

[31] G.K. Andersen, C. Klumpner, S.B. Kjær, and F Blaabjerg, "A new green power inverter for fuel cells," in *Power Electronics Specialists Conference, 2002. PESC'02, IEEE 33rd Annual*, 23-27 June 2002, vol. 2, pp. 727 – 733.

[32] Jason Lai, "A high-efficiency low-cost DC-DC converter for SOFC performance and control of V6 converter," Tech. Rep., Virginia Polytechnic Institute and State University Future Energy Electronics Center, 2004.

[33] *Nexa Power Module User's Manual*, Ballard Systems Inc., 2003.

[34] T.E. Springer, T.A. Zawodzinski, M.S. Wilson, and S. Gottesfeld, "Characterization of polymer electrolyte fuel cell using AC impedance spectroscope," *Journal of the Electrochemical Society*, vol. 143, pp. 587–599, 1996.

[35] Jens T. Mueller and Peter M. Urban, "Characterization of direct methanol fuel cell by ac impedance spectroscopy," *Journal of Power Sources*, vol. 75, pp. 139–143, 1998.

[36] N. Buchi Felix, Alois Marek, and Gunther G. Scherer, "In situ membrane resistance measurements in polymer electrolyte fuel cells by fast auxiliary current pulses," *Journal of the Electrochemical Society*, vol. 142, pp. 1895–1901, 1995.

[37] C.G. Lee, H. Nakano, T. Nishina, I. Uchida, and S. Kuroe, "Characterization of a $100cm^2$ class molten carbonate fuel cell with current interruption," *Journal of the Electrochemical Society*, vol. 145, pp. 2747–2751, 1998.

[38] P.J.H. Wingelaar, J.L. Duarte, and M.A.M. Hendrix, "Dynamic characteristics of PEM fuel cells," in *Power Electronics Specialists Conference, 2005. PESC'05, IEEE 36th Annual*, June 12 2005, pp. 1635 – 1641.

[39] Shaoduan Ou and Luke E.K. Achenie, "A hybrid neural network model for PEM fuel cells," *Journal of Power Sources*, vol. 140, pp. 319 – 330, February 2005.

[40] S.O.T. Ogaji, P. Pilidis R. Singh, and M. Diacakis, "Modelling fuel cell performance using artificial intelligence," *Journal of Power Sources*, vol. 154, pp. 192 – 197, March 2006.

[41] Amir Abtahi Anucha Saengrung and Ali Zilouchian, "Neural network model for a commercial PEM fuel cell system," *Journal of Power Sources*, doi:10.1016/j.jpowsour.2007.05.039 2007.

[42] Simon Haykin, *Neural Networks-A comprehensive Foundation*, Prentice-Hall Inc., 1999.

[43] Xin Kong, A.M. Khambadkone, and Soy kee Thum, "A hybrid model with combined steady state and dynamic characteristics of PEMFC fuel cell stack,"

in *Industry Applications Conference, Fortieth IAS Annual Meeting, Conference Record of the 2005*, 2-6 October 2005, pp. 1618 – 1625.

[44] Ned Mohan, Tore M Undeland, and William P Robbins, *Power Electronics: Converters, Applications and Design, Second Edition*, John Wiley and Sons Inc, 1995.

[45] Marian K. kazimierczuk, *Pulse-width Modulated DC-DC Power Converters*, John Wiley, 2008.

[46] Kaushik Rajashekara, "Propulsion system strategies for fuel cell vehicles," Tech. Rep., Energenix Center Delphi Automotive systems, March 2000.

[47] "http://www.fuelcellcontrol.com/dcconverter.html," .

[48] G.J. Su and F.Z. Peng, "A low cost, triple-voltage bus dc-dc converter for automotive applications," in *Applied Power Electronics Conference and Exposition, APEC'05. 20th Annual IEEE, 2005*, 6-10 March 2005, vol. 2, pp. 1015 – 1021.

[49] R. Oruganti, "Notes for EE5711 power electronics and system," Tech. Rep., Department of Electrical and Computer Engineering, National University of Singapore, 2003-04.

[50] Q. Zhao and F.C. Lee, "High-efficiency, high step-up dc-dc converters," *IEEE Transactions on Power Electronics*, vol. 18, pp. 65 – 73, January 2003.

[51] Su-Jin Jang, Tae-Won Lee, Ku-Sam Kang, Soo-Seok Kim, and Chung-Yuen Won, "A new active clamp sepic-flyback converter for a fuel cell generation system," in *Industrial Electronics Society, 2005. IECON'05. The 31th Annual Conference of the IEEE*, 6-10 Nov. 2005, pp. 2538 – 2542.

[52] P.G. Vernados, M.G. Ioannides, and S.N. Manias, "Application of power electronics to fuel cell technology," in *3rd Mediterranean Conference and Exhibition On Power Generation, Transmission, Distribution and Energy Conversion, MED POWER 2002*, 4-6 Nov. 2002.

[53] R. Gopinath, Sangsun Kim, and Jae-Hong Hahn, "Development of a low cost fuel cell inverter system with DSP control," in *Power Electronics Specialists Conference, 2002. PESC'02, IEEE 33rd Annual*, 23-27 June 2002, vol. 1, pp. 309 – 314.

[54] J.Mazumdar, I.Batarseh, N.Kutkut, and O.Demirci, "High frequency low cost DC-AC inverter design with fuel cell source for home applications," in *Industry Applications Conference, 2002, 37th IAS Annual Meeting Conference Record*, 13-18 Oct. 2002, vol. 2, pp. 789–794.

[55] Robert W. Erickson and Dragan Maksimovic, *Fundamentals of Power Electronics*, Kluwer Academic publishers, 2000.

[56] M.H. Todorovic, L. Palma, W. Choi, C. Dowling, D. Humphrey, D. Tarbell, P. Enjeti, and J. Howze, "Development of a low cost fuel cell inverter system

with dsp control for residential use," in *2003 Fuel Cell Seminar Special Session on Fuel Cell Power Conditioning and International Future Energy Challenge*, Nov. 3 2003, pp. 21 – 26.

[57] C. Smith, M. Gilliom, D. Urciuoli, A. McLandrich, E. Pepa, and Jih-Sheng Lai, "Low-cost solid oxide fuel cell power conditioning with bidirectional charging," in *2003 Fuel Cell Seminar Special Session on Fuel Cell Power Conditioning and International Future Energy Challenge*, Nov. 3 2003, pp. 8 – 15.

[58] D.S. Oliveira, Jr., and I. Barbi, "A three-phase ZVS PWM DC/DC converter with asymmetrical duty cycle for high power applications," *IEEE Transactions on Power Electronics*, vol. 20, pp. 370 – 377, March 2005.

[59] E. Santi, D. Franzoni, A. Monti, D. Patterson, F. Ponci, and N. Barry, "A fuel cell based domestic uninterruptible power supply," in *Applied Power Electronics Conference and Exposition 2002, APEC 2002*, 10-14 March 2002 2002, vol. 1, pp. 605–613.

[60] A.M. Tuckey and J.N. Krase, "A low-cost inverter for domestic fuel cell applications," in *Power Electronics Specialist Conference PESC'02 IEEE 33rd Annual*, 23-27 June 2002, vol. 1, pp. 339–346.

[61] Troy Nergaard, Jeremy Ferrell, and Leonard Leslie, "Design of a 10kW inverter for a fuel cell," Tech. Rep., Virginia Tech, 2001.

[62] Troy A. Nergaard, Jeremy F. Ferrell, Leonard G. Leslie, and Jih-Sheng Lai, "Design considerations for a 48V fuel cell split single phase inverter system with ultracapacitor energy storage," in *Power Electronics Specialist Conference PESC'02 IEEE 33rd Annual*, 23-27 June 2002, vol. 4, pp. 2007–2012.

[63] J. Wang, F.Z. Peng, J. Anderson, A. Joseph, and R. Buffenbarger, "Low cost fuel cell converter system for residential power generation," *IEEE Transactions on Power Electronics*, vol. 19, pp. 1315 – 1322, September 2004.

[64] H.J. Cha and P.N. Enjeti, "A new soft switching direct converter for residential fuel cell power system," in *Industry Applications Conference, 39th IAS Annual Meeting, Conference Record of the 2004 IEEE*, 3-7 October 2004, pp. 1172 – 1177.

[65] S. Meo, A. Perfetto, L. Piegari, and F. Esposito, "A ZVS current fed DC/DC converter oriented for applications fuel-cell-based," in *Industrial Electronics Society, 2004. IECON'04. The 30th Annual Conference of the IEEE*, 2-6 Nov. 2004, pp. 932 – 937.

[66] Robert Balog, "Non-linear boundary techniques for a boost converter," Project report, August 2001.

[67] P.T. Krein and R. Balog, "Low cost inverter suitable for medium-power fuel cell sources," in *Power Electronics Specialist Conference PESC'02 IEEE 33rd Annual*, 23-27 June 2002, vol. 1, pp. 321–326.

[68] C. Liu, T.Nergaard, L. Leslie, J. Ferrell, and J.Bates, "Power balance control and voltage conditioning for fuel cell converter with multiple sources," in *Power Electronics Specialists Conference, 2002. PESC'02, IEEE 33rd Annual*, 23-27 June 2002, vol. 4, pp. 2001–2006.

[69] X. Huang, T. Nergaard, and Jih-Sheng lai, "A DSP based controller for high-power interleaved boost converters," in *Applied Power Electronics Conference and Exposition, APEC'03. 18th Annual IEEE, 2003*, Feb. 9-13 2003, vol. 1, pp. 327 – 333.

[70] Haiping Xu, Xuhui Wen, and Li Kong, "Dual-phase DC-DC converter in fuel cell electric vehicle," in *Power Electronics Congress, 2004. CIEP 2004. 9th IEEE International*, Oct. 17-22 2004, pp. 92 – 97.

[71] W. Choi, P. Enjeti, and J.W. Howze, "Fuel cell powered UPS systems: design considerations," in *Power Electronics Specialists Conference, 2003. PESC'03, IEEE 34th Annual*, June 15-19 2003, vol. 1, pp. 385 – 390.

[72] M.H. Todorovic, L. Palma, and P. Enjeti, "Design of a wide input range dc-dc converter with a robust power control scheme suitable for fuel cell power conversion," in *Applied Power Electronics Conference and Exposition, APEC'04. 19th Annual IEEE, 2004*, 2004, vol. 3, pp. 374 – 379.

[73] Kunrong Wang, Fred C Lee, and Jason Lai, "Operation principles of bi-directional full-bridge DC/DC converter with unified soft-switching scheme

and soft-starting capability," in *Applied Power Electronics Conference and Exposition, 2000. APEC 2000, Fifteenth Annual IEEE*, Feb 6-10 2000, vol. 1, pp. 111–118.

[74] Kunrong Wang, Lizhi Zhu, Dayu Qu, H Odendaal, J. Lai, and F.C. Lee, "Design, implementation, and experimental results of bi-directional full-bridge DC/DC converter with unified soft-switching scheme and soft-starting capability," in *Power Electronics Specialists Conference, 2000. PESC'00, IEEE 31st Annual*, June 18-23 2000, vol. 2, pp. 1058–1063.

[75] S.J. Jang, T.W. Lee, W.C. Lee, and C.Y. Won, "Bi-directional dc-dc converter for fuel cell generation system," in *Power Electronics Specialists Conference, 2004. PESC'04, IEEE 35th Annual*, June 20-25 2004, vol. 6, pp. 4722 – 4728.

[76] L. Rongyuan, A. Pottharst, N. Fröhleke, and J. Böcker, "Analysis and design of improved isolated full-bridge bidirectional dc-dc converter," in *Power Electronics Specialists Conference, 2004. PESC'04, IEEE 35th Annual*, June 20-25 2004, vol. 1, pp. 521 – 526.

[77] V. Ramanarayanan, "Notes for switched mode power conversion," Tech. Rep., Indian Institute of Science.

[78] Ming Hian Chew, "Power-one inrush current control," Tech. Rep., Power-One.

[79] Ming Hian Chew, "Design of power factor correction circuit using greenline compact power factor controller mc33260," Tech. Rep., ON Semiconductor.

[80] Lizhi Zhu, Kunrong Wang, F.C. Lee, and Jih-Sheng Lai, "New start-up schemes for isolated full-bridge boost converters," *IEEE Transactions on Power Electronics*, vol. 18, pp. 946 – 951, July 2003.

[81] Gun-Woo Moo and Myung-Joong Youn, "Start-up inrush current elimination control of new push-pull quantum series resonant rectifier," *IEEE Transactions on Power Electronics*, vol. 13, pp. 995 – 1004, November 1998.

[82] R. Attanasio, M. Cacciato, F. Gennaro, and A. Consoli, "An innovative boost converter for fuel cells stationary generation systems," in *Industrial Electronics Society, 2004. IECON'04. The 30th Annual Conference of the IEEE*, 2-6 Nov. 2004, pp. 2831 – 2836.

[83] F.Z. Peng, "Z-source inverter," *IEEE Transactions on Industry Applications*, vol. 39, pp. 504 – 510, March/April 2003.

[84] Jin-Woo Jung, Min Dai, and Ali Keyhani, "Modeling and control of a fuel cell based z-source converter," in *Applied Power Electronics Conference and Exposition, APEC'05. 20th Annual IEEE, 2005*, March 6-10 2005, vol. 2, pp. 1112 – 1118.

[85] Yoon-Ho Kim, Hyun-Wook Moon, Soo-Hong Kim, Eun-Jin Cheong, and Chung-

Yeon Won, "A fuel cell system with z-source inverters and ultracapacitors," in *Power Electronics and Motion Control Conference, 2004. IPEMC 2004. The 4th International*, August 14-16 2004, vol. 3, pp. 1587 – 1591.

[86] F.Z. Peng, M. Shen, and Z.Qian, "Maximum boost control of the z-source inverter," *IEEE Transactions on Power Electronics*, vol. 20, pp. 833 – 838, July 2005.

[87] *Simulation software SIMPLORER 6.0 user manual*, Ansoft Corporation, 1996-2002.

[88] Katsuhiko Ogata, *Modern Control Engineering*, Prentice-Hall Inc., 1970.

[89] W. C. Wu, R. M. Bass, and J. R. Yeargan, "Eliminating the effects of right half plane zero in fixed frequency boost converters," in *Power Electronics Specialists Conference, 1998. PESC'98*, 1998, vol. 1, pp. 362–366.

[90] Kanakasabai Viswanathan, *Dynamic Performance Improvement In Boost And Buck-Boost-Derived Power Electronic Converters*, Ph.D. thesis, National University of Singapore, 2004.

[91] Jean Jacques, E. Slotine, and Weiping Li, *Applied Nonlinear Control*, Englewood Cliffs, Prentice Hall, 1991.

[92] Abhishek Drolia, Philip Jose, and Ned Mohan, "An approach to connect ultracapacitor to fuel cell powered electric vehicle and emulating fuel cell electrical

characteristics using switched mode converter," in *Industrial Electronics Society, 2003. IECON'03. The 29th Annual Conference of the IEEE*, 2-6 Nov. 2003, pp. 897 – 901.

[93] T.W. Lee, B.K. Lee, S.J. Jang, S.H. Kim, and C.Y. Won, "Development of a 3kW fuel cell generation system with an active fuel cell simulator: Topology, control, and design," in *Power Electronics Specialists Conference, 2004. PESC'04, IEEE 35st Annual*, June 20-25 2004, vol. 6, pp. 4743 – 4748.

[94] Ken Stanton and Jason Lai, "A thermally dependent fuel cell model for power electronics design," in *Power Electronics Specialists Conference, 2005. PESC'05, IEEE 36th Annual*, June 12 2005, pp. 1647 – 1651.

[95] M.Ordonez, M.T. Iqbal, and J.E. Quaicoe, "A novel fuel cell simulator," in *Power Electronics Specialists Conference, 2005. PESC'05, IEEE 36th Annual*, June 12 2005, pp. 178 – 184.

[96] J.Moreno, M. E. ortuzar, and J. W. Dixon, "Energy management system for a hybrid electric vehicle, using ultracapacitors and neural networks," *IEEE Transactions on Industrial Electronics*, vol. 52, pp. 614 – 623, April 2006.

[97] Ke Jin, Xinbo Ruan, Mengxiong Yang, and Min Xu, "A novel hybrid fuel cell power system," in *Power Electronics Specialists Conference, 2006. 37th IEEE*, 18 - 22 June 2006, pp. 1–7.

[98] M. Michon, J. L. Duarte, M. Hendrix, and M. G. Simoes, "A three-port bi-directional converter for hybrid fuel cell systems," in *Power Electronics Specialists Conference, 2004. 35th IEEE*, 20 - 25 June 2004, pp. 4736 – 4742.

[99] J. S. Lai and D. J. Nelson, "Energy management power converters in hybrid electric and fuel cell vehicles," *Proceedings of the IEEE*, vol. 95, pp. 766 – 777, April 2007.

[100] M. Tekin, D. Hissel, M. C.Pera, and J. M. Kauffmann, "Energy-management strategy for embedded fuel-cell systems using fuzzy logic," *IEEE Transactions on Industrial Electronics*, vol. 54, pp. 595 – 603, February 2007.

[101] L. Palma, M. Harfman Todorovic, and P. Enjeti, "Design considerations for a fuel cell powered DC-DC converter for portable applications," in *Applied Power Electronics Conference and Exposition, APEC'06. 21st Annual IEEE, 2006*, March 19-23 2006, pp. 1263 – 1268.

List of Publications

Published/Accepted for Publication

Journals

1. Xin Kong and Ashwin M. Kambadkone, "Analysis and Implementation of a High Efficiency, Interleaved Current-Fed Full Bridge Converter for Fuel Cell System", *Published in IEEE transactions on Power Electronics*, Vol. 22, Issue 2, March 2007, pp.543 - 550.

2. Haihua Zhou, Ashwin M. Kambadkone and Xin Kong, "Passivity Based Control for an Interleaved Current Fed Full Bridge converter With a Wide Operating Range using the Brayton Moser Form", *Accepted for publish in IEEE transactions on Power Electronics.*

Conferences

1. Xin Kong and Ashwin M. Khambadkone, "Dynamic modeling of fuel cell with power electronic circuit and performance analysis", *2003 international conference on power electronics and drive systems, PEDS 2003*, 17-20 November, 2003, pp.607 - 612.

2. Xin Kong and Lim Thian Choi and Ashwin M Khambadkone, "Analysis and Control of Isolated Current-fed Full Bridge Converter in Fuel Cell System", *The 30th Annual Conference of the IEEE Industrial Electronic Society, IECON 2004*, 2-6 November, 2004, pp.2825 - 2830.

3. Xin Kong, A. M. Khambadkone and Soy kee Thum, "A Hybrid Model With Combined Steady State and Dynamic Characteristics of PEMFC Fuel Cell Stack", *Industry Applications Conference, Fortieth IAS Annual Meeting, Conference Record of the 2005*, 2-6 October, 2005, pp.1618 - 1625.

4. Xin Kong and Ashwin M. Khambadkone, "Analysis and Implementation of a High Efficiency, Interleaved Current-Fed Full Bridge Converter for Fuel Cell System", *2005 international conference on power electronics and drive systems, PEDS 2005*,28 Nov.- 01 Dec., 2005, pp.474 - 479.

5. Xin Kong, Wenjie Yeau and A.M. Khambadkone, "ANN modelling of nonlinear subsystem of a PEMFC Stack for a Dynamic and Steady State Operation", *2003 The 32th Annual Conference of the IEEE Industrial Electronic Society,*

IECON 2006, November, 2006, pp.4322 - 4327.

6. Haihua Zhou, Ashwin M. Khambadkone and Xin Kong, "Fast Dynamic Response in a Fuel Cell Based Converter Using Augmented Energy Storage", *Power Electronics Specialists Conference, 2007. PESC 2007*, June, 2007.

7. Haihua Zhou, Ashwin M. Khambadkone and Xin Kong, "A Passivity based control with augmented integration for an Interleaved Current Fed Full Bridge converter as a front end for fuel cell source", *The 42th Annual Meeting of the IEEE Industry Applications Society, IAS 2007*, September, 2007

Appendix A

Effect of Fuel Cell Current Ripple

A.1 Effect of Fuel Cell Current Ripple

This section aims to report the effect of fuel cell current ripple from the test on a $1.2kW$ fuel cell stack. Understanding the effect of ripple current on fuel cell helps decide the performance criteria for the DC-DC converter circuit.

When a fuel cell stack is connected with power electronic circuits, the switching ripple produced by the circuit will reflect in the fuel cell current. The presence of such current ripple may affect the fuel cell stack itself and furthermore, it may affect the requirement of the selection of interfaced DC/DC converters. In order to find out the effect of such switching ripple on the fuel cell stack, a series of experiments were done in the laboratory. In this thesis, the effect of fuel cell current ripple is investigated on hydrogen consumption.

Experiments were conducted on the $1.2kW$ PEM fuel cell stack from Ballard $Nexa^{TM}$. Experimental setup is shown in Fig. A.1. Load bank is the load resistance

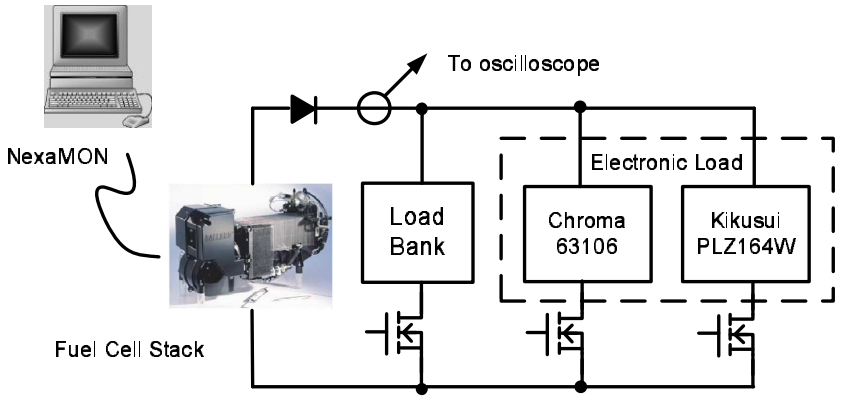

Figure A.1: Experimental setup designed for testing on the effect of fuel cell current ripple.

network that can be switched on/off according to different current requirement. NexaMon OEM software can provide accumulated hydrogen consumption in unit Liter. If the sampling rate of the data logging is $1s^{-1}$, hydrogen consumption HC during a certain period $\Delta t = T$ can be obtained as $HC(T+T_0) - HC(T_0)$. Where $HC(T+T_0)$ is hydrogen consumption at time $t = T + T_0$ and $HC(T_0)$ is hydrogen consumption at time $t = T_0$. Load bank and electronic load are parallelled to obtain a DC current with triangular current ripple. Current ripple at different frequency is generated by electronic loads. Two electronic loads are used in the test. Each electronic load can only cover certain range of frequency. Chroma 63106 DC electronic load $12A/120A$, $16V/80V$, $600W$ is used to generate triangular current from $1kHz$ to $10kHz$. While Kikusui electronic load $PLZ164W$, $1.5 - 150V$, $0 - 33A$ is used to obtain triangular current from $50Hz$ to $500Hz$. Both of these two electronic loads are operating at constant current mode. To protect the fuel cell stack, ripple amplitude generated from the electronic load is controlled to be less than $1.5A$. Experiments were done in the following steps:

- Step 1: Switch off the electronic load and adjust the load bank to obtain $7.5A$ load current (see Fig. A.2(a)).
- Step 2: Adjust the electronic load to obtain a triangular current with a 50% duty cycle, $1A$ amplitude, and $10kHz$ frequency (see Fig. A.2(b)).
- Step 3: Switch on the electronic load and the fuel cell current is now the super-

position of the load bank and the electronic load, which is a triangular current from minimum $8.5A$ to maximum $9.5A$ (see Fig. A.2(c)).

- Step 4: Record the hydrogen consumption of the stack during a period of $\Delta t = 280s$.

- Step 5: Vary the frequency of the load current from $10kHz$ to $50Hz$, repeat step 1 to step 4.

- Step 6: Calculate the RMS DC value of the triangular fuel cell current, which is $I_{rms} = \sqrt{I_{ave}^2 + \frac{(\Delta I)^2}{12}}$. Where I_{ave} is the average value of the triangular fuel cell current and ΔI is the current ripple of the triangular fuel cell current, as seen in Fig. A.2(c)). Then switch off the electronic load and adjust the load bank to obtain an equivalent DC current at $I_{rms} = 9.0A$. Record the hydrogen consumption of the stack during a period of $\Delta t = 280s$.

- Step 7: Plot out the relationship of the hydrogen consumption $vs.$ current ripple frequency.

Fig. A.3 shows a triangular wave load current with a 50% duty cycle drawn from the fuel cell stack. This waveform is recorded from the oscilloscope. Fig. A.4 shows the hydrogen consumption as a function of fuel cell current frequency. In order to make it clear, hydrogen consumption at the equivalent DC current I_{rms} is normalized to be 1.0. It can be seen that hydrogen consumed in the stack increases due to the presence of the ripple current. For frequency less than $1kHz$, fuel cell

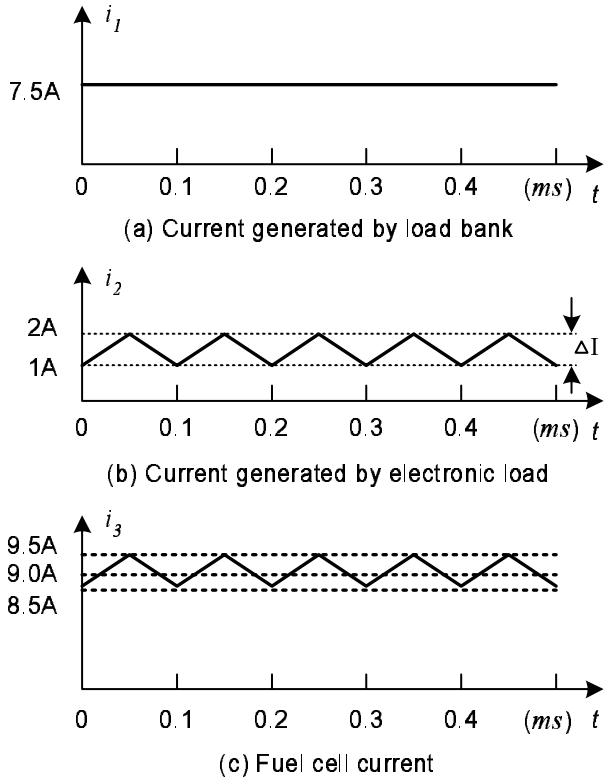

Figure A.2: Sketch of the generation of fuel cell current with triangular current ripple.

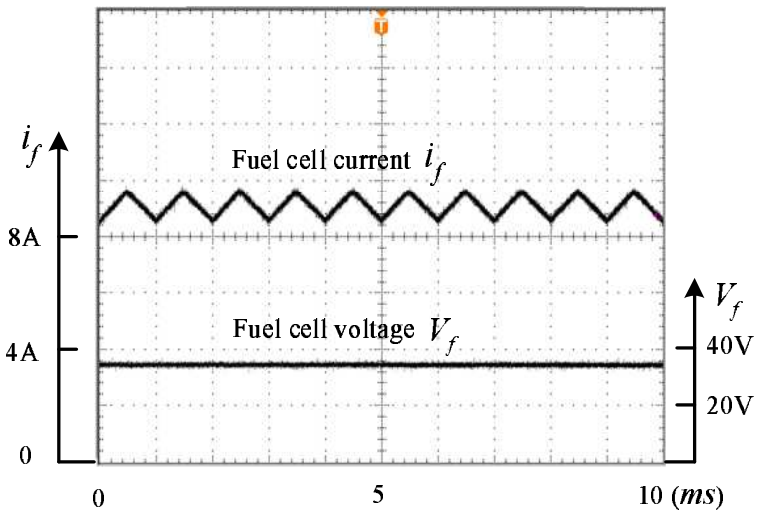

Figure A.3: Sample waveform of fuel cell current with $1kHz$ current ripple.

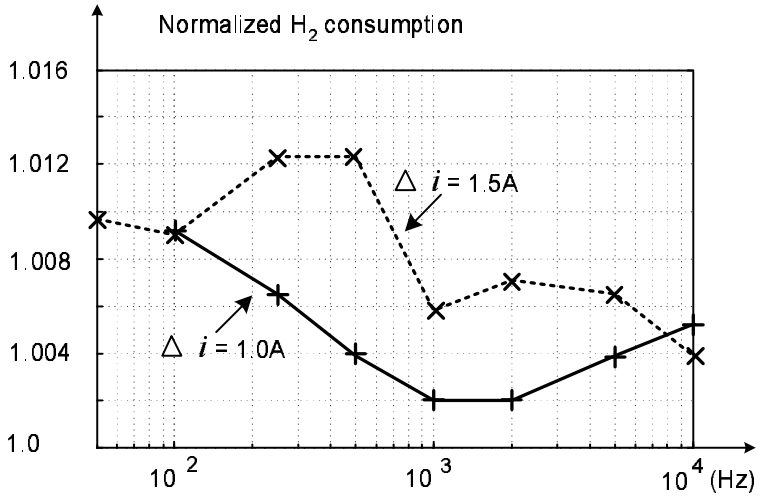

Figure A.4: Hydrogen consumption vs. switching ripple frequency

consumes about 1% additional hydrogen while for frequency higher than $5kHz$, fuel cell consumes more than 0.5% extra hydrogen. Moreover, another curve is drawn on Fig. A.4 for comparison. It is hydrogen consumption with the same I_{rms} but $1.5A$ current ripple. These two curves seem to suggest that the larger the current ripple, the more extra hydrogen is consumed. Some similar results have also been reported in [101].

The experiment done in this section seems to indicate that ripple current induced by the power electronic circuit increases the fuel consumption. Hence small current ripple might be preferred for less fuel consumption. However more experiment should be done in future to consolidate this conclusion.

Appendix B

Circuit Schematic and Layout for Fuel cell Test

B.1 Circuit Schematic for Variable Load Control in Fuel Cell Test

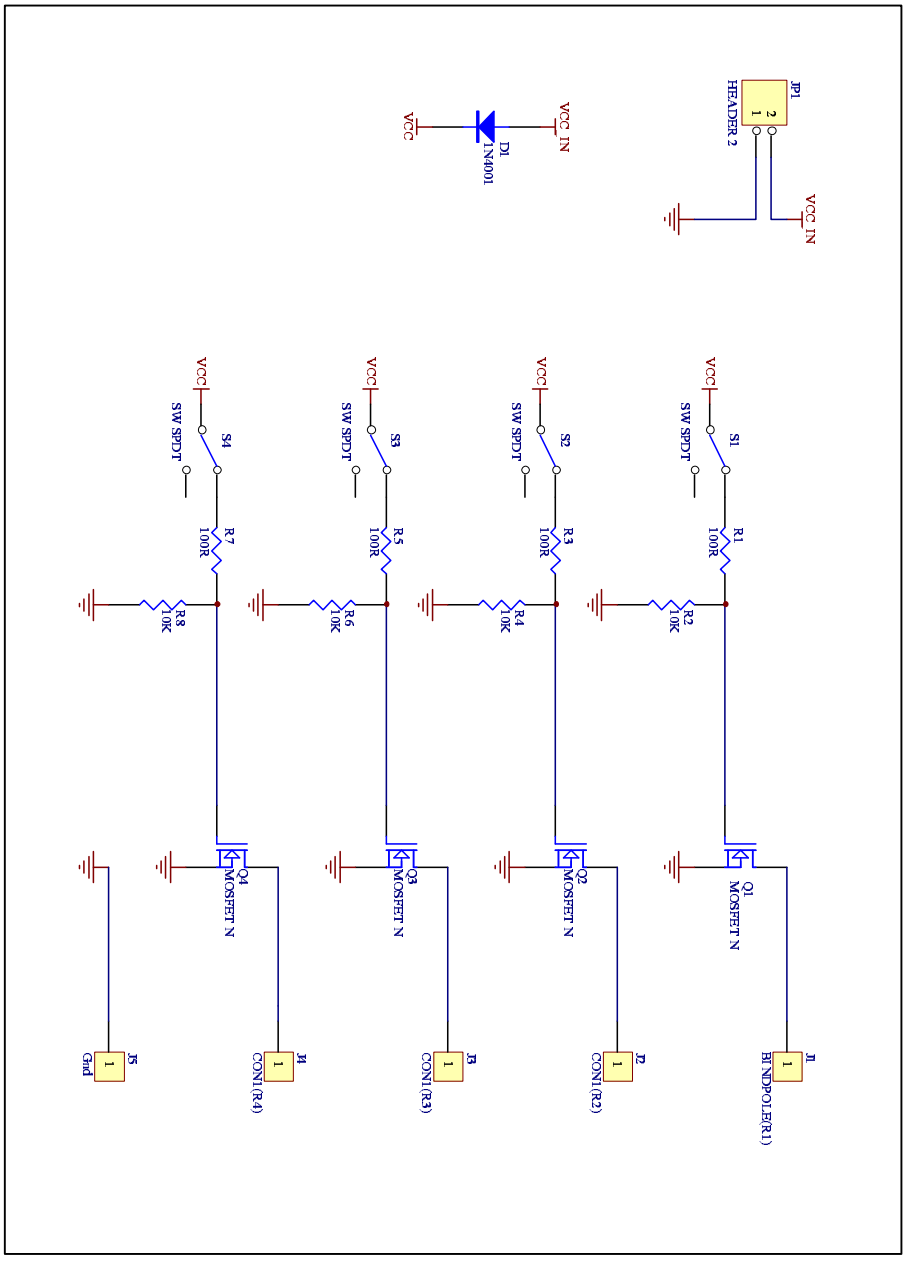

B.2 Layout for Variable Load Control in Fuel Cell Test

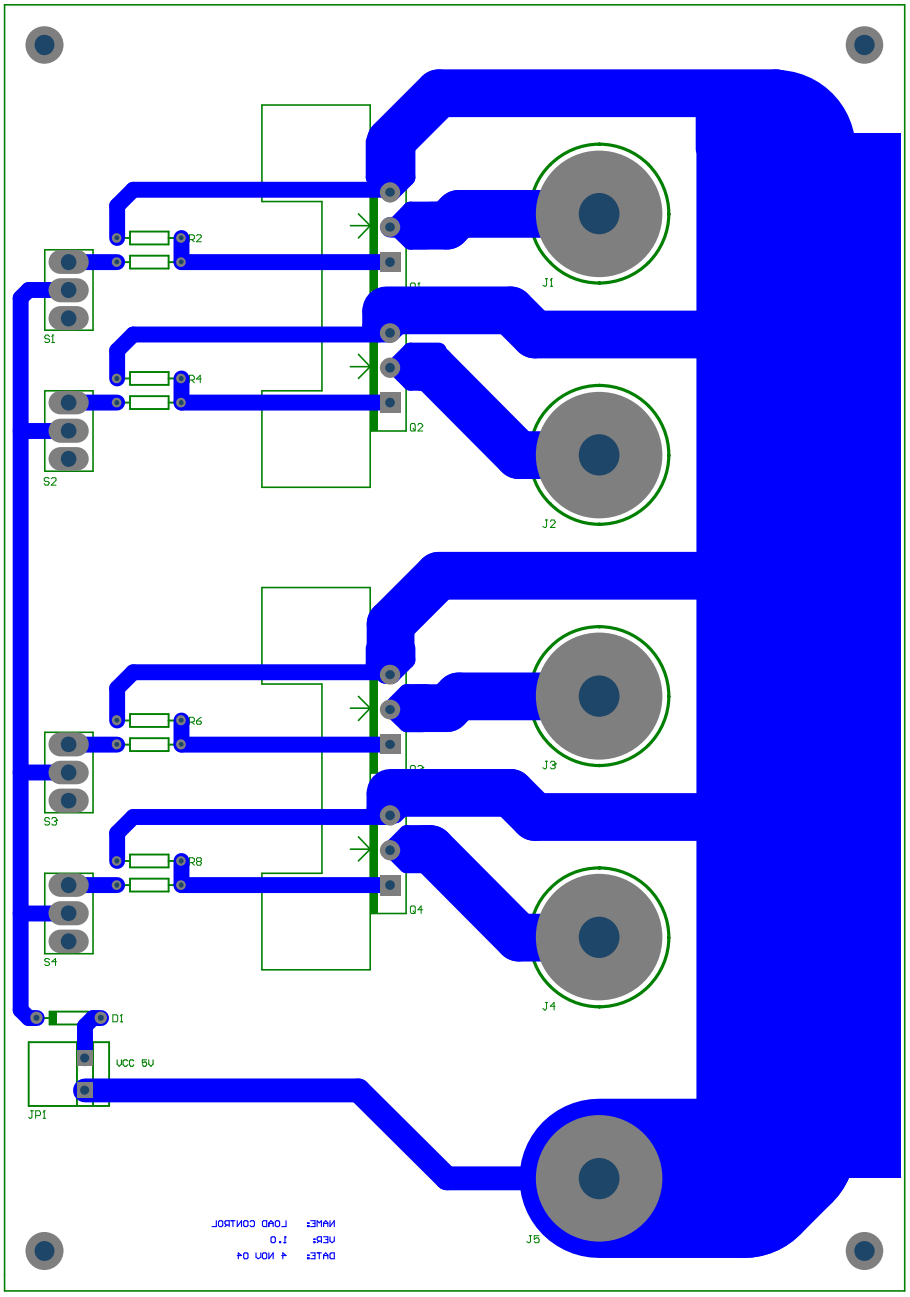

Appendix C

Circuit Schematic and Layout for CFFB Converter

C.1 Circuit Schematic for CFFB Converter

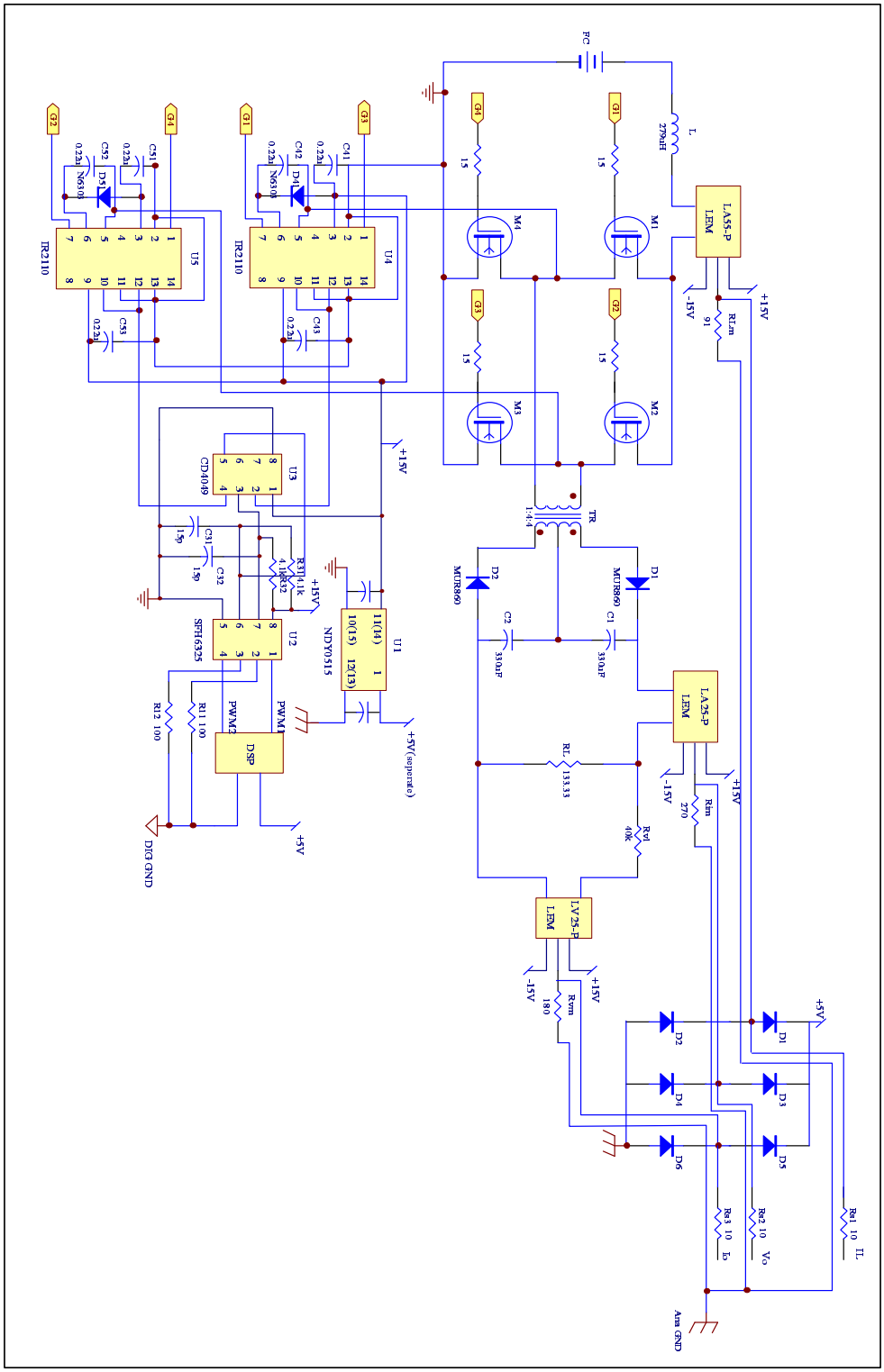

C.2 Layout of the Primary Side for CFFB Converter

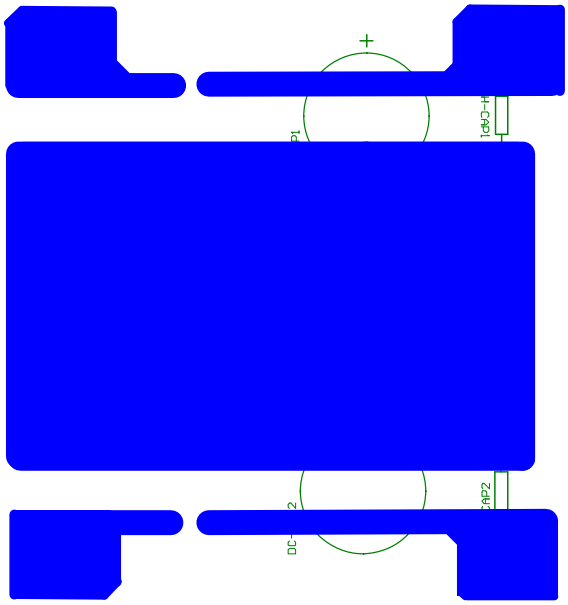

<Secondary Side>

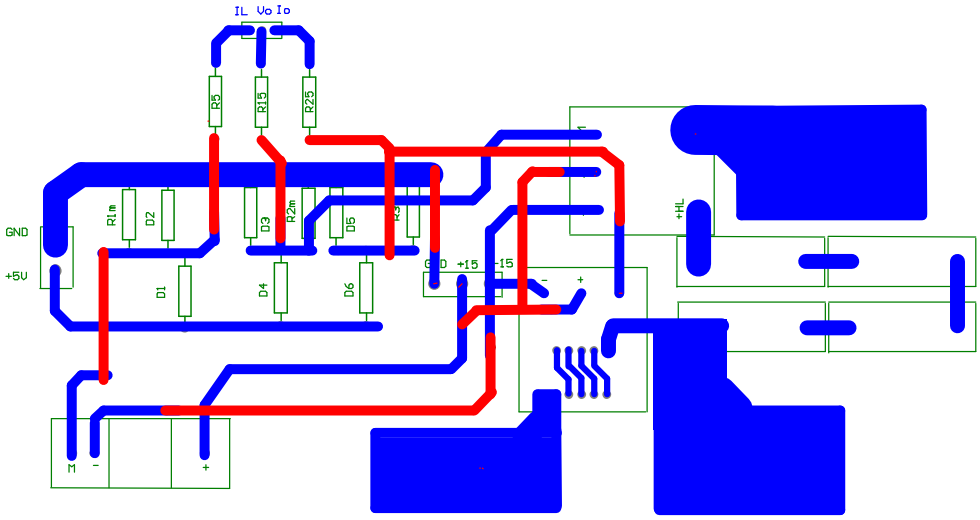

Sensor board

C.3 Layout of the Secondary Side for CFFB Converter

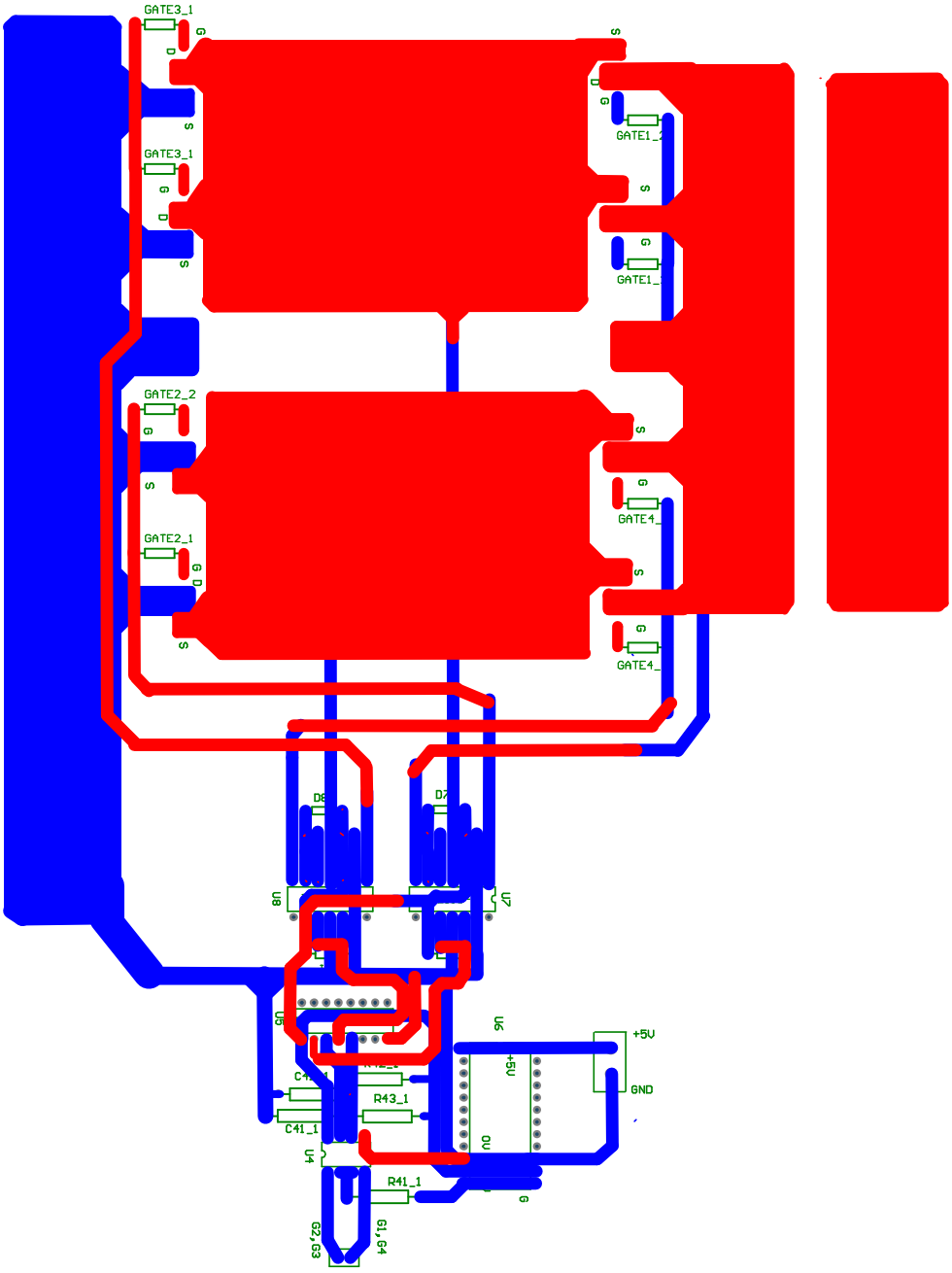

Appendix D

Circuit Schematic and Layout for ICFFB Converter

D.1 Circuit Schematic for ICFFB Converter

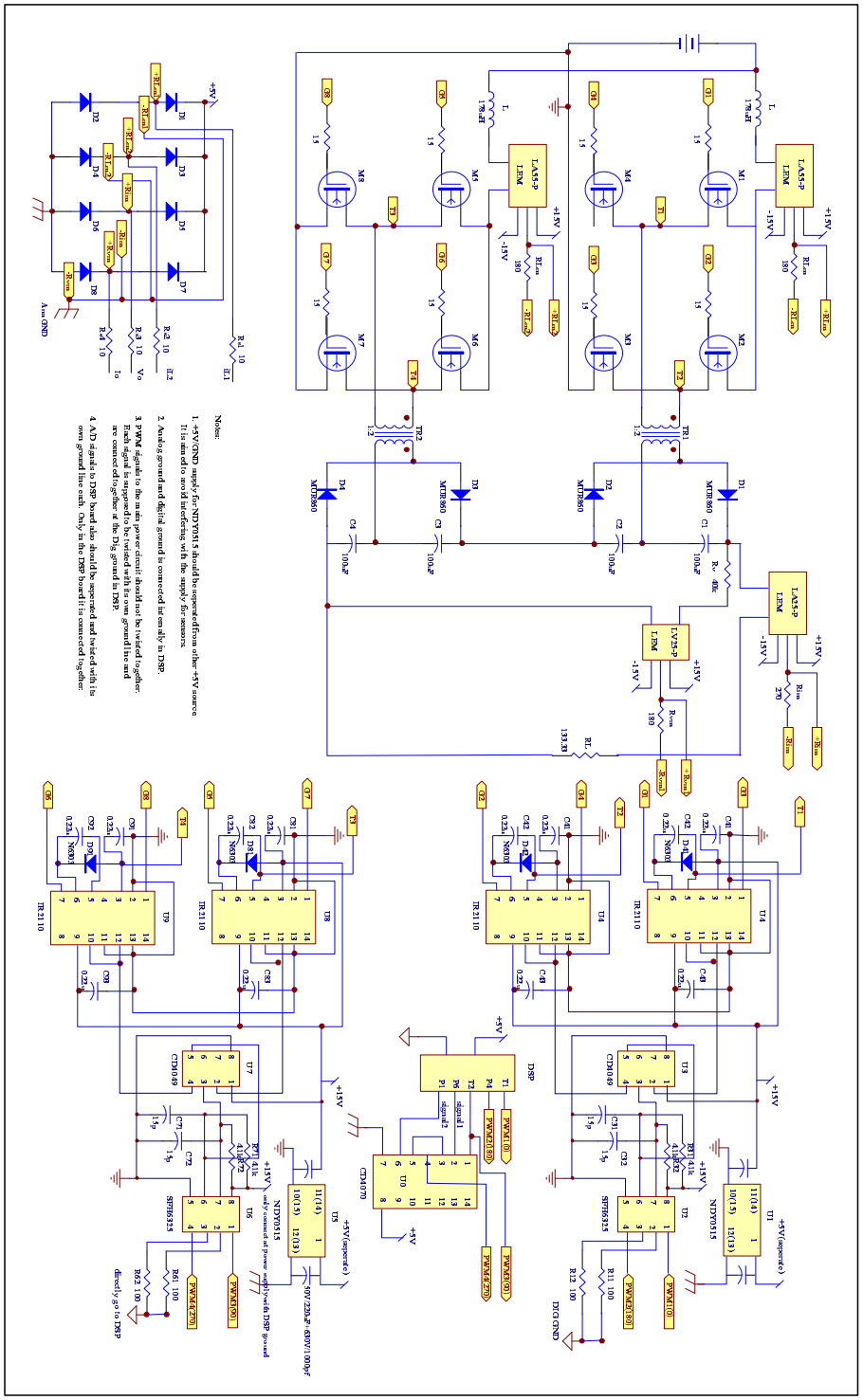

D.2 Layout of the Primary Side for ICFFB Converter

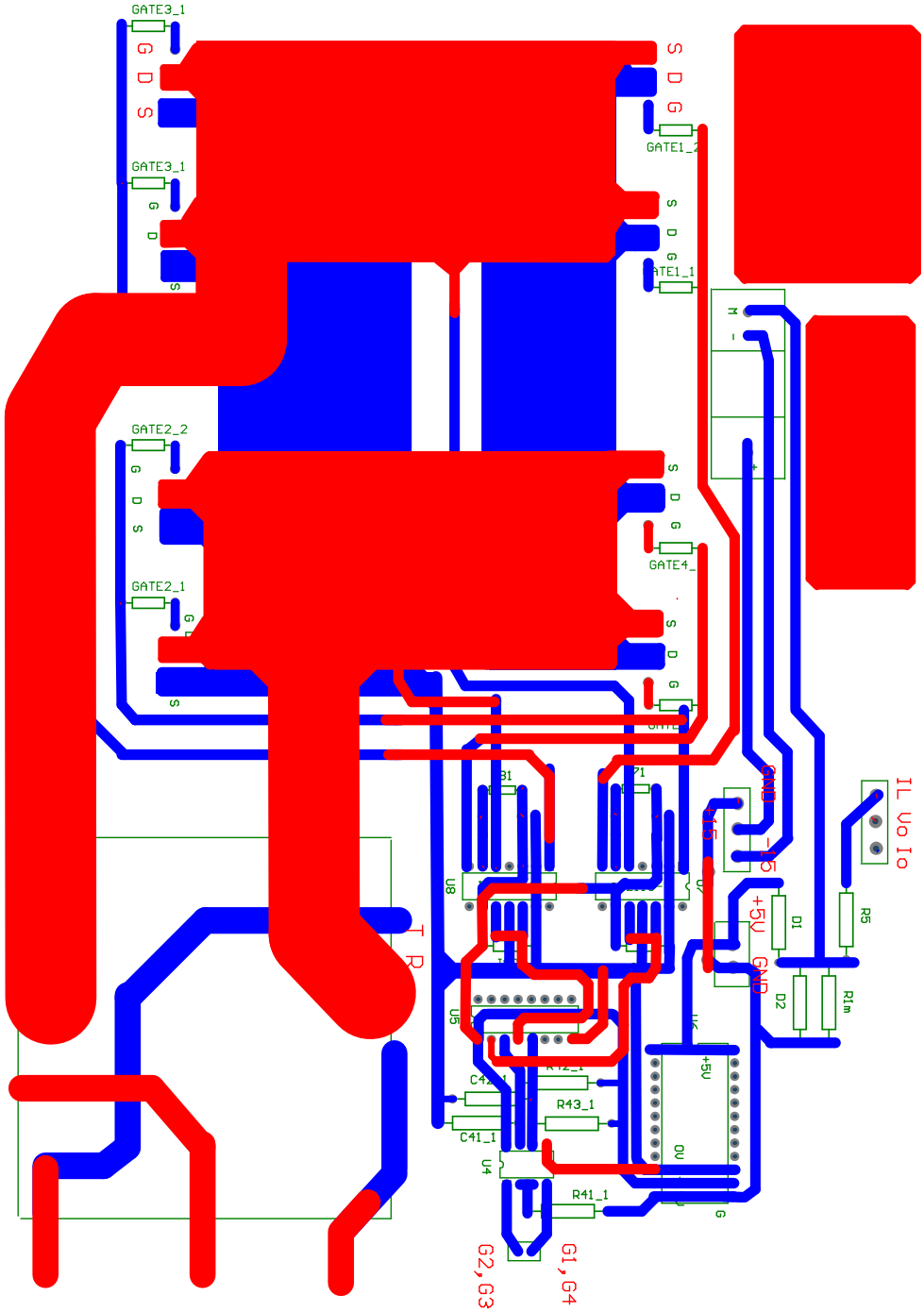

D.3 Layout of the Secondary Side for ICFFB Converter

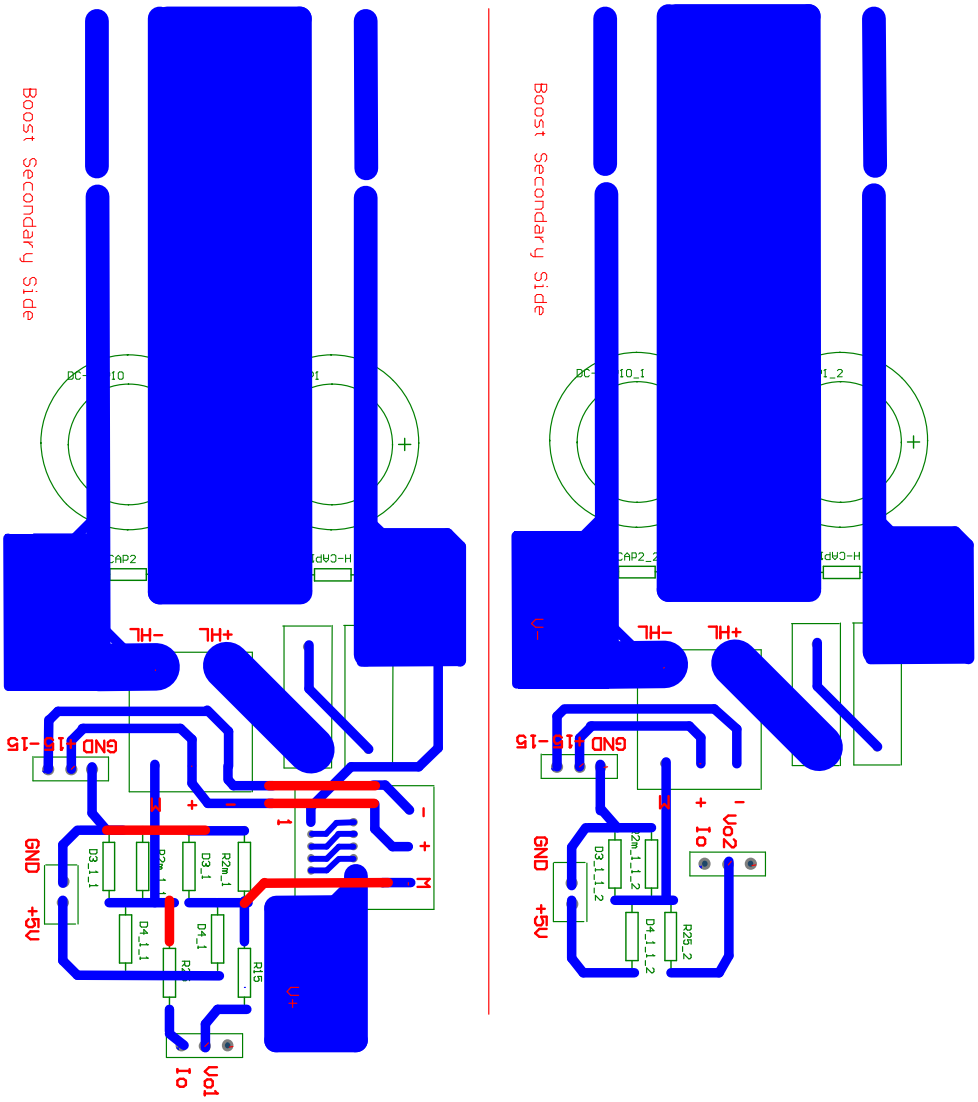

D.4 Layout of auxiliary board for ICFFB Converter

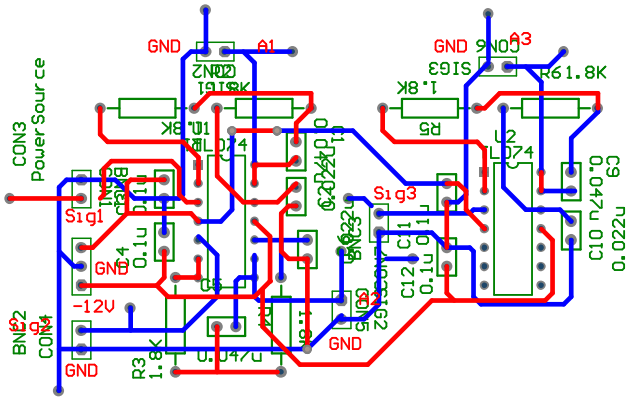

D.5 Build of ICFFB Converter